LBL-36504
UC-404

Center for Advanced Materials

CAM

Pt and Pd Contacts on ZnSe

K.J. Duxstad
(M.S. Thesis)

November 1994

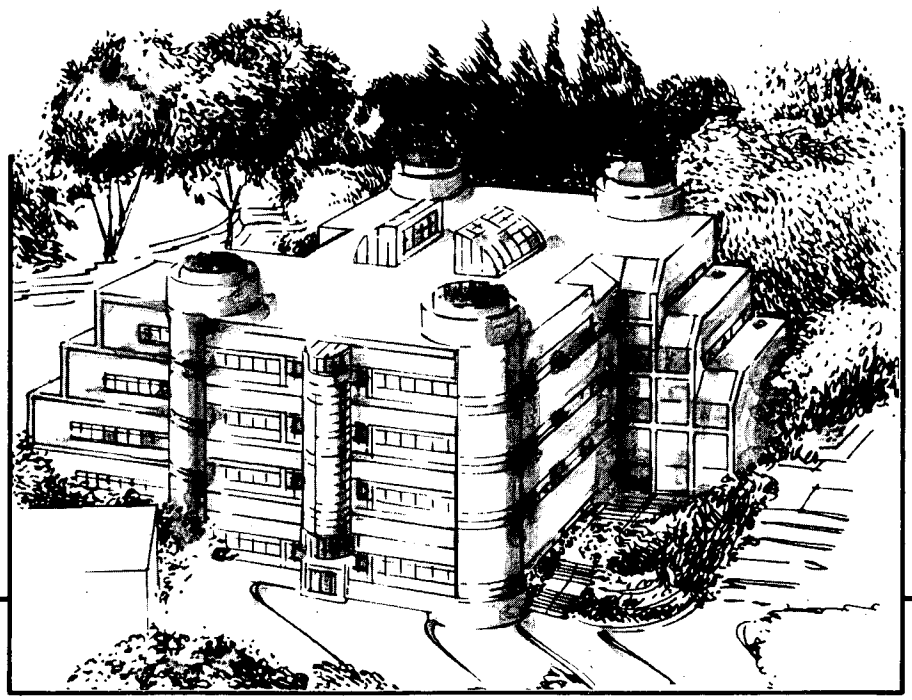

Materials and Chemical Sciences Division
Lawrence Berkeley Laboratory • University of California
ONE CYCLOTRON ROAD, BERKELEY, CA 94720 • (415) 486-4755

Prepared for the U.S. Department of Energy under Contract DE-AC03-76SF00098

REFERENCE COPY
Does Not
Circulate
Bldg. 50 Library.
LBL-36504
Copy 1

DISCLAIMER

This document was prepared as an account of work sponsored by the United States Government. While this document is believed to contain correct information, neither the United States Government nor any agency thereof, nor the Regents of the University of California, nor any of their employees, makes any warranty, express or implied, or assumes any legal responsibility for the accuracy, completeness, or usefulness of any information, apparatus, product, or process disclosed, or represents that its use would not infringe privately owned rights. Reference herein to any specific commercial product, process, or service by its trade name, trademark, manufacturer, or otherwise, does not necessarily constitute or imply its endorsement, recommendation, or favoring by the United States Government or any agency thereof, or the Regents of the University of California. The views and opinions of authors expressed herein do not necessarily state or reflect those of the United States Government or any agency thereof or the Regents of the University of California.

LBL-36504
UC-404

Pt and Pd Contacts on ZnSe

KRISTIN JOY DUXSTAD

Center for Advanced Materials, Materials Sciences Division
Lawrence Berkeley Laboratory, 1 Cyclotron Rd.
Berkeley, CA 94720

and

Materials Science and Mineral Engineering Department
University of California
Berkeley, CA 94720

M.S. Thesis

November 1994

This work was supported by the Director, Office of Energy Research, Office of Basic Energy Sciences, Materials Science Division of the U.S. Department of Energy under Contract No. DE-AC03-76SF00098. The author acknowledges support from the University of California Graduate Mentor Fellowship program and the AT&T Bell Labs Ph.D. Fellowship program.

Table of Contents

1. Introduction 1

    1.1 ZnSe 2
    1.2 Metal contacts 3
    1.3 Phase formation in thin films 8
    1.4 Issues to be resolved for Pt and Pd on ZnSe 10

2. Characterization techniques for analysis of thin film systems 12

    2.1 Rutherford Backscattering Spectroscopy (RBS) 12
    2.2 X-ray diffraction 19
    2.3 Complementary techniques 24
        2.3.1 Transmission Electron Microscopy (TEM) 25
        2.3.2 X-ray Photoelectron Spectroscopy (XPS) 25

3. Metal contacts on semiconductors 27

    3.1 Overview of Pt and Pd silicides 27
        3.1.1 Phase formation behavior 28
        3.1.2 Electrical characteristics 37

    3.2 Overview of Pt and Pd on GaAs 39
        3.2.1 Phase formation behavior 39
        3.2.2 Electrical characteristics 48

    3.3 ZnSe literature review 50
        3.3.1 Metal contact behavior 52
        3.3.2 Surface preparation methods 57

4. Experimental 58

    4.1 Sample preparation 58
        4.1.1 Surface preparation 58
        4.1.2 Deposition 60
        4.1.3 Annealing 61

    4.2 Characterization- experimental setup 61
        4.2.1 RBS 61
        4.2.2 X-ray diffraction 62
        4.2.3 X-ray photoelectron spectroscopy 62

5. Results and discussion 63
    5.1 Surface characteristics 63

5.2 Pd 71
5.3 Pt 82

6. Conclusions 90

7. References 93

Appendices:

Appendix I: ZnSe etchants 98
Appendix II: ZnSe OMVPE growth parameters 99
Appendix III: Powder diffraction data file record numbers for Pd/Zn/Se and Pt/Zn/Se phases 100
Appendix IV: Pd_5ZnSe crystal structure 101

Acknowledgments

I would like to thank Professor Eugene Haller for suggesting this project and providing the resources to pursue it. Kin Man Yu provided invaluable expertise and insight into metal contact behavior on semiconductors and many hours of patient direction on the principles and operation of the RBS and x-ray equipment. I would also like to acknowledge Xi Wei Lin for performing the TEM on my samples and Wendy Swider for preparing the TEM samples. Without the details obtained from TEM, it would have been much more difficult to ascertain the behavior of these systems. I am grateful for the support of all of my fellow graduate students and staff in our research group. In particular, I am indebted to Chris Olsen and Jeff Beeman for their help with equipment and general lab protocol and Hilary Baumann for performing XPS measurements. In addition, the ZnSe samples grown by Edith Bourret and Jim Walker provided the basis for this project. I would like to thank Dr. Tim Sands and Dr. Nathan Cheung for reviewing this thesis.

I wish to acknowledge financial support from the University of California Graduate Mentor Fellowship program and the AT&T Bell Labs Ph.D. Fellowship program.

On a more personal level, I would like to thank Dr. Frank Bates from the University of Minnesota for encouraging me in the field of Materials Science and the pursuit of graduate school. I am also grateful for the support of my family, and especially my parents. Their commitment to education has motivated me throughout my academic career. Finally, I am most thankful for the love and support of my husband, Dave. Without his encouragement and understanding this work would not have been accomplished.

1. Introduction

II-VI compound semiconductors have been studied and used for decades. They have been widely utilized in radiation detectors, CRT screens, and a myriad of other devices. However, a number of difficulties related to the growth of high quality bulk crystals and highly perfect thin films, doping limitations, and the rich spectrum of native defects have limited the uses and scientific understanding of these materials. In contrast, the ability to grow and process high quality group IV and III-V semiconductors has allowed them to become the key elements of today's electronics industry. Recently, II-VI materials have undergone a scientific and technical renaissance, due to the application of growth techniques such as molecular beam epitaxy (MBE) and organo-metallic vapor phase epitaxy (OMVPE). These methods allowed the development of thin films of high purity and excellent crystallinity and opened the door to a much deeper scientific understanding and many new uses. The wide, direct band gaps of many of these materials make them ideal candidates for blue/green lasers and light emitting diodes (LEDs). The drive for new devices has encouraged the continued development of II-VI thin films and increased understanding of the fundamental behavior of this class of semiconductors. The ability to obtain high quality crystalline films makes it possible to study the basic properties of this exciting class of materials. For example, practically no data exist on II-VI semiconductor-metal solid phase reactions.

1.1 ZnSe

ZnSe, in particular, has generated a great deal of interest due to its direct bandgap of 2.7 eV at room temperature. Light generated by this material lies in the blue region of the visible spectrum and several groups have reported the development of blue lasers from ZnSe systems (Bhargava 1992; Chung, et al. 1992; Gunshor, et al. 1993; Haase, et al. 1991; Han, et al. 1994; Neumark, et al. 1994; Xie, et al. 1993; Yu, et al. 1993). The ability to create useful devices from ZnSe requires the development and understanding of good Ohmic and Schottky contacts. One of the key needs is a knowledge of the thin film reactions that occur at the interface of these contacts. The thermal stability over the range of possible processing and operating temperatures must be considered. Also important is an insight into the effect these reactions have on Schottky barrier heights and electrical characteristics.

Current theories are unable to precisely predict the Schottky barrier that will be formed at a contact and further study of the metal-semiconductor interface may aid in the development of accurate predictions. The ionic character of II-VI materials is stronger than in other semiconductors. An understanding of the effects of this bonding difference may lead to new perceptions about semiconductor properties. An evaluation of the behavior of metal thin films on ZnSe will be applicable to other II-VI compounds because of their similar ionic bonding characteristics. Schottky barrier formation may be related to the degree of chemical reaction at the interface (Brillson 1994). This chemical reaction between metal and semiconductor can result in regions with localized bonding, defect

formation, or new chemical phases. The driving force for reaction between the metal and semiconductor decreases from group IV to III-V compounds, and is expected to further decrease for II-VI compounds due to the smaller electronegativity differences (Sands and Keramidas 1994). Electronegativity differences between metals and II-VI semiconductors are small because nearly every metal is electronically similar to either the group II or group VI element. Semiconductors with more ionic bonding are more sensitive to band bending due to metal deposition than covalently bonded semiconductors where the surface Fermi Energy is pinned (Brillson 1994). Schottky barriers on ionic semiconductors have a stronger dependence on the metal work function.

1.2 Metal Contacts

Metal contacts to semiconductors are one of the basic components of every semiconductor device and have been studied for many decades, but are still not well understood. Only the very basics of ideal interfaces will be discussed here. The details of metal-semiconductor contacts are covered in many semiconductor device textbooks, for example see reference (Sze 1981).

The behavior of the Fermi energy equilibrium in a metal to semiconductor contact is similar to that of an abrupt p-n junction. When the metal and semiconductor come into contact the Fermi levels must equilibrate. If we consider a metal whose Fermi level lies below that of an n-type semiconductor, we encounter the situation appearing in figure 1.1. ϕ_M is the work function of the metal, this is defined as the difference between the Fermi

level in the metal and the vacuum level. When the metal and semiconductor come in contact, electrons from the semiconductor will flow into the metal to find lower energy

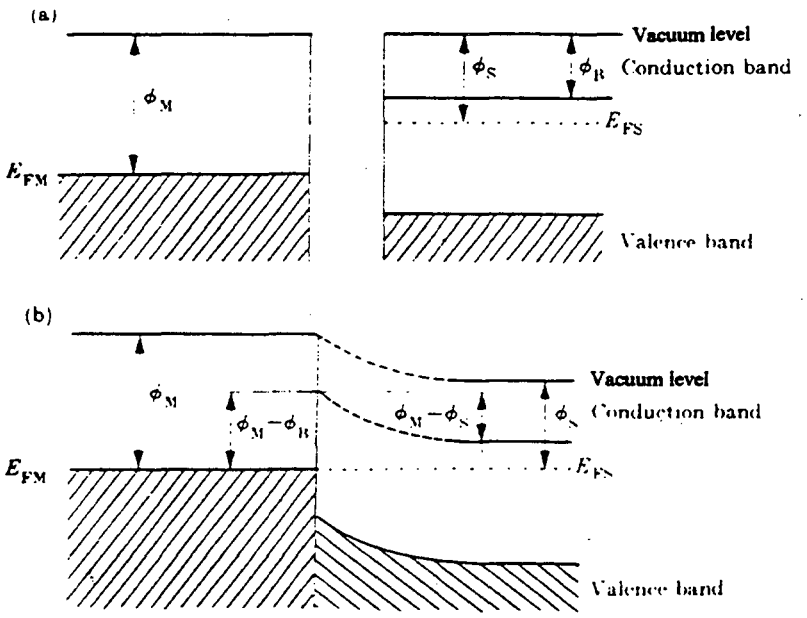

Figure 1.1: Energy diagrams for a junction between a metal and an n-type semiconductor ($\phi_M > \phi_S$), (a) before contact, (b) after contact the Fermi levels agree ($E_M = E_{FS}$) (Solymar and Walsh 1988)

states. This creates a region on the semiconductor side that is depleted of free carriers. The fixed positive space charge results in band bending. Electrons will flow until there are no longer lower energy states available, i.e., the Fermi levels align. This situation has now created a potential barrier for electrons wishing to pass in either direction. The difference between the metal work function, ϕ_M, and the electron affinity, ϕ_B, is the barrier height. These barriers are termed Schottky barriers, after Walter Schottky who was the first to propose a theory for metal-semiconductor junctions (Schottky 1938). Schottky barriers can be useful as diodes. The height of the barrier on the semiconductor side can be adjusted by applying a bias. Depending on the polarity, the bias can make it easier or

harder for electrons to flow in out of the semiconductor. With the polarity in the reverse direction, the barrier is high and few electrons can pass into the metal; with the polarity in the forward direction, electron flow into the metal becomes easy. To first order, applying a bias does not affect the height of the potential barrier for electrons traveling from the metal to the semiconductor. This means that this system can never provide a good Ohmic contact if the barrier is larger than a few kT. Instead, a highly doped surface layer is often used to create an Ohmic contact. A very highly doped shallow layer results in a very narrow barrier which electrons can tunnel through, in either direction, with ease.

When the relative sizes of the metal and semiconductor work functions are different from the previous case, such as in figure 1.2, the equilibration of Fermi levels may not result in a barrier.

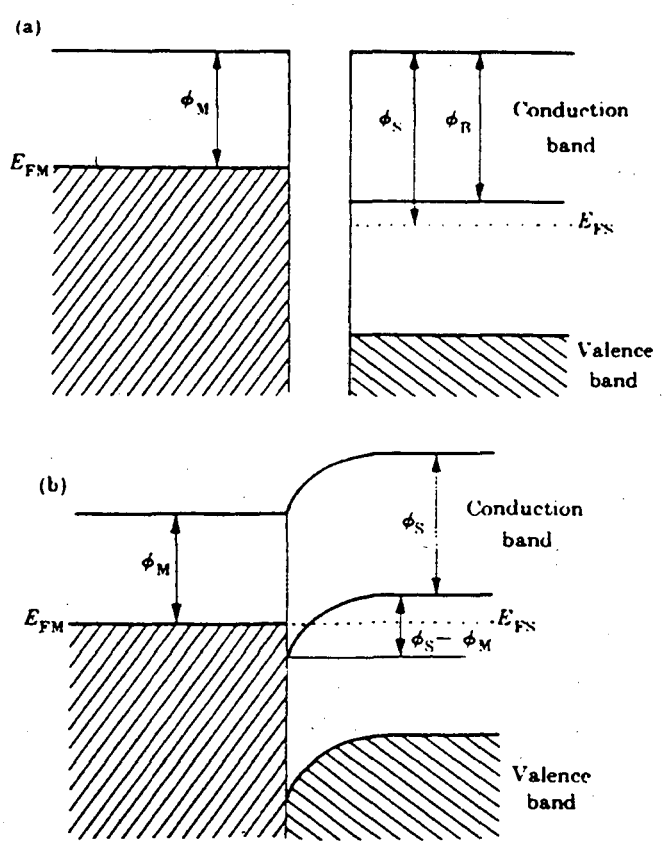

Figure 1.2: Energy diagrams for a junction between a metal and an n-type semiconductor ($\phi_M<\phi_S$), (a) before contact, (b) after contact the Fermi levels agree ($E_{FM}=E_{FS}$) (Solymar and Walsh 1988)

In this case, electrons can flow easily in either direction and there is no potential barrier. This condition is called an Ohmic contact. Ohmic contacts are important for many semiconductor devices. When building a laser, for example, it is important that current be able to flow through the device without significant voltage drop or power loss due to contact resistances.

The barrier height of a contact can be measured in several ways. One of the easiest is to measure the current-voltage (I-V) characteristics of the contact. The current flowing through the contact under bias can be described by the equation below.

$$I = AA^{**}T^{2}e^{\frac{-\phi_{SB}q}{kT}}\left(e^{\frac{qV}{nkT}}-1\right) \qquad (1.1)$$

In this equation, A is the area of the contact, n is the ideality factor, ϕ_{SB} is the barrier height and A** is the effective Richardson constant which is dependent on the material. Data obtained for V>>kT/q and plotted as log(I) vs. V will be linear. The terms outside of the parentheses define the saturation current, I_s. This current can be determined from the y-intercept of the linear portion of the graph. The barrier height can then be calculated using the following equation.

$$\phi_{SB} = \frac{kT}{q}\ln\left(\frac{AA^{**}T^{2}}{I_s}\right) \qquad (1.2)$$

The above discussion gives a idealized view of the electrical behavior of metal-semiconductor contacts. Barrier heights at metal-semiconductor contacts can not actually be predicted with the difference between the work functions. In reality, defects at the

surfaces and interfacial layers must be considered. At this time, all of the intricacies of contacts are not understood, but there are several competing theories which attempt to predict the height of Schottky barriers or where the Fermi level will be pinned. Even though barrier heights can not be predicted based on simple physical principles, they can be formed reproducibly for many metal-semiconductor junctions and both blockage and Ohmic metal-semiconductor contacts are used extensively on practically every semiconductor device.

Certain characteristics are important for any contact to be used in a device. It is important for a good contact to provide the desired electrical behavior, good adhesion, high corrosion resistance, and be compatible with any further processing steps. Quality contacts are vital for high yield and device reliability. To provide high yield and reliability, the thermal stability of the contact must be known. Any interdiffusion or reaction at the interface during processing or use may result in a degradation of electrical or mechanical behavior, therefore it is important to study these systems.

Many studies have focused on the behavior of metals on Si and GaAs. These studies were fundamental for the development of stable Ohmic and Schottky contacts, improved theories for Schottky barrier heights, as well as increased understanding of thin film behavior. Studies of contact behavior on ZnSe and other II-VI semiconductors will aid both in the development of new devices and in the basic understanding of contact behavior.

1.3 Phase formation in thin films

The ability of two materials in contact to form a new stable phase at an interface depends on a competition between kinetic and thermodynamic driving forces. To form, new phases must overcome the thermodynamic barrier to nucleation. To grow, the kinetics of the system must allow enough of each reactant to diffuse to the interface. It can be shown that if the nucleation step is the limiting factor, the system is reaction controlled and follows the relationship $X = Dt$, where X is the layer thickness, D the diffusivity and t the time. If the diffusion of material to the interface is the limiting reaction, the system is diffusion controlled. In this case the layer growth follows the relationship $X^2 = Dt$ and the layer grows with the square root of time.

An important added consideration for thin film systems is the supply of reactants. In bulk systems, reaction under the proper conditions will allow all equilibrium phases in the phase diagram to be observed at once. In thin film systems, many of the equilibrium phases are not observed during a reaction sequence. Moreover , those that are observed usually do not exist simultaneously, but form in succession. An in-depth mathematical description of these interactions is covered in the work by Gösele and Tu (Gösele and Tu 1982). They determined that the first phase to form would be the one that had the lowest nucleation barrier. Their evaluation then showed that while the first phase was growing in a diffusion controlled manner, no other phase would form until it reached a critical thickness. In thin film systems this critical thickness usually can not be attained because of

a limited supply of one reactant. Figure 1.3 indicates the sequence of phases through which the reaction will proceed.

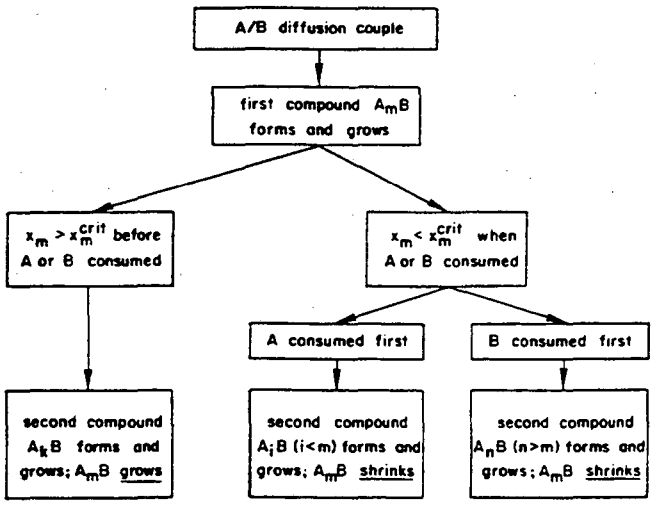

Figure 1.3: The three possibilities for second phase formation under different supply conditions of the component A and B in a planar A/B diffusion couple. The compound A_kB may coincide with either A_iB or A_nB. (Gösele and Tu 1982)

If the supply of a reactant is exhausted before the critical thickness is reached, the relative amounts of the semiconductor and metal determine the phase sequence and final phase. Figure 1.4 shows an example of this phase formation behavior in the Ni-Si system. In this case it has been found that variations in the amount of reactants alters the phase sequence and final phases.

Thin film reactions on compound semiconductors are more complicated because there are two binary systems and one ternary system competing. Few of the ternary phase diagrams are known. Studying the reactions of thin metal films on II-VIs will enhance the understanding of kinetics and phase formation in thin films.

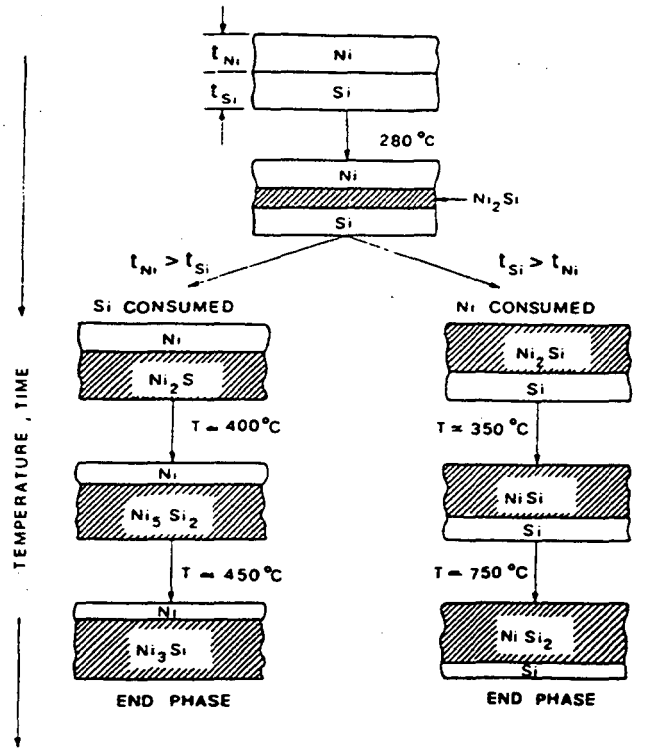

Figure 1.4: Schematic diagrams showing the phase formation in a Si-Ni thin film and Si(crystal)/Ni film system. Initially the Ni_2Si phase is formed and then after one of the elements is consumed the system is driven toward equilibrium by the formation of compounds richer in the remaining element. The indicated temperatures are rough guides for the formation of phases for films a few thousand Å thick and an annealing time of 1 hour. (Ottaviani 1979)

1.4 Issues to be resolved for Pt and Pd on ZnSe

The behavior of Pt and Pd on Si and GaAs has been studied in detail. The phase formation sequences have been characterized as well as the electrical behavior corresponding to these phase changes. Very little research, however, has been done on the thermal stability of metal contacts to ZnSe, or any II-VI compounds. A greater understanding of these systems is necessary to develop good contacts. For example, many of the Ohmic contact schemes on GaAs employ alloys or multilayers. An approach like

this may provide an Ohmic contact to ZnSe, but in order to develop a multilayer system we must have a basic understanding of ternary phase equilibria in thin film M-II-VI systems. A knowledge of the temperatures for phase formation and the morphology of the resulting systems must be pursued.

Pt and Pd provide a desirable starting point. Both metals react at low temperatures on Si and GaAs to form distinct phases. They are good candidates for contact formation because they may react at low temperatures (as on Si and GaAs), are corrosion and oxidation resistant, and are easy to deposit. Also, since they are both relatively heavy elements (compared to Zn and Se) the RBS profiles are more easily interpreted than for other lighter elements.

2. Characterization techniques for analysis of thin film systems

In this work, Rutherford backscattering spectrometry (RBS) and x-ray diffraction are the primary tools used to structurally characterize thin film interfacial reactions. RBS provides composition information and a depth profile of the semiconductor-metal structure in one dimension. X-ray diffraction provides information on solid solution and phase formation. Transmission electron microscopy (TEM) and x-ray photoelectron spectroscopy (XPS) are utilized as complementary techniques. TEM furnishes information on the morphology of the films and phase identification through electron diffraction patterns. XPS is useful for measuring surface composition and bonding. The information that these techniques provide can reliably describe the products of the reactions that occur between the metal film and the substrate.

2.1 Rutherford Backscattering (RBS)

RBS can reveal the extent of diffusion, layer structure with depth, and the relative composition of layers. It provides quantitative measurements without the need for standards. Several articles and texts provide a more rigorous treatment of this technique (Chu and Langouche 1993; Chu, et al. 1973; Chu, et al. 1978; Mayer and Tu 1974).

RBS is based on the very simple premise of energy and momentum conservation during a two-body collision. To perform RBS, ions (usually He^+) are accelerated to an energy of 1-4 MeV and is directed at the sample. Some of these particles will collide with

nuclei in the sample and will be backscattered at large angles, close to 180°. Figure 2.1 shows a schematic of the interaction.

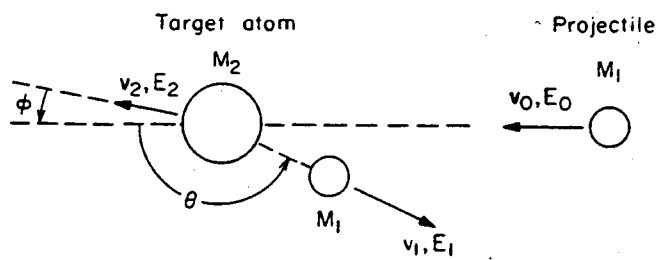

Figure 2.1: Schematic representation of an elastic collision between a projectile of mass M_1, velocity v_o, and energy E_o and a target mass M_2 which is initially at rest. After the collision, the projectile and the target mass have velocities and energies, v_1, E_1, and v_2, E_2, respectively. (Chu, et al. 1978)

In this figure, θ is the backscattering angle. Using equations for the conservation of momentum and the conservation of energy we can find a kinematic factor, K, which is the ratio of the energy after collision to the incident energy.

$$K_{M_2} = \frac{E_1}{E_0} = \left[\frac{(M_2^2 - M_1^2 \sin^2 \Theta)^{\frac{1}{2}} + M_1 \cos\Theta]}{M_2 + M_1} \right]^2 \qquad (2.1)$$

Values for K are tabulated for all elements for a variety of backscattering angles (θ). Measuring the energy of the He ions backscattered from the sample allows the

composition of the sample to be determined because it is only a factor of the mass of the target atom, mass of the backscattered ion and the angle. When a sample contains more than one element and their masses differ by only a small amount ΔM_2, interpretation of the RBS spectra can be difficult. Figure 2.2 shows the variation of K with target mass for ^4He ions.

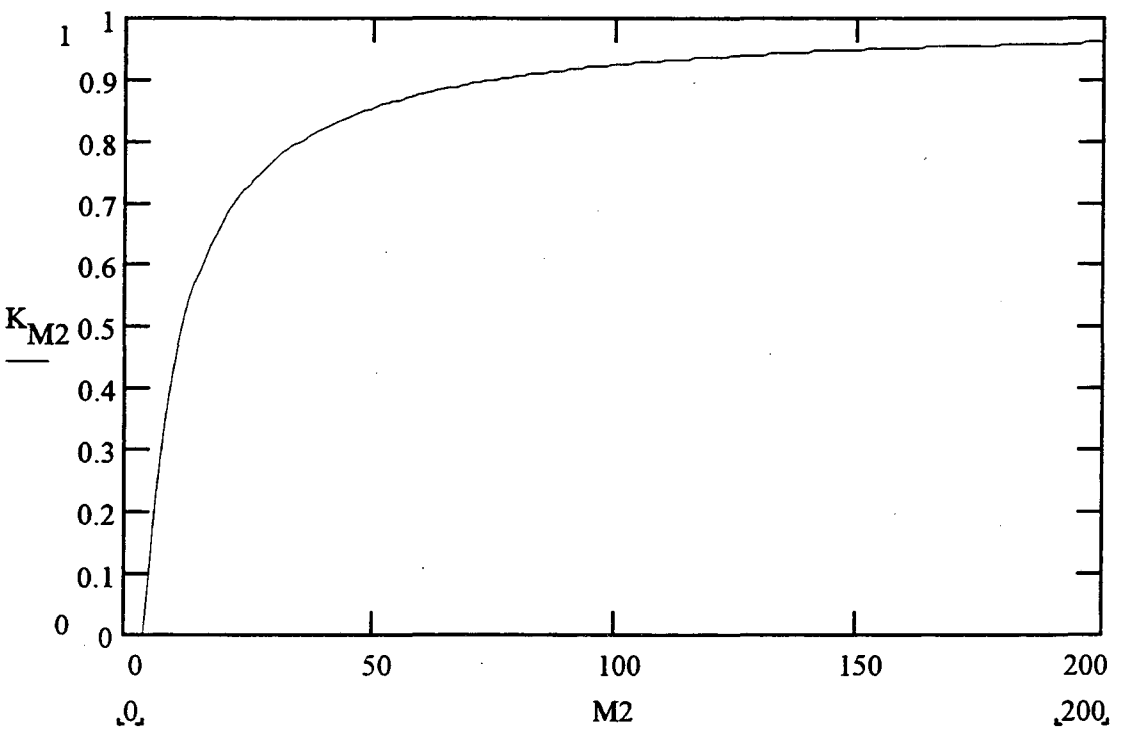

Figure 2.2: Kinematic factor versus target mass for ^4He projectiles calculated for a 170° scattering angle.

From this figure, it is clear that the difference in energy of the backscattered ion will be much smaller for two heavy elements than for two light elements or a light and a heavy element. For this reason, it can be difficult to separate spectra resulting from two heavy elements with similar mass.

The composition ratio of a compound sample can be determined because the number of backscattered ions is dependent on the differential scattering cross section, $\frac{d\sigma}{d\Omega}$, of the target elements. The differential scattering cross section is defined as the ratio of the number of particles scattered into the direction, θ, divided by the incident flux and can be estimated as shown in equation 2 for systems where the mass of the target atom is much larger than that of the incident ion.

$$\frac{d\sigma}{d\Omega} \cong \left(\frac{Z_1 Z_2 e^2}{4E}\right)^2 \bullet \left[\sin^{-4}\frac{\theta}{2} - 2\left(\frac{M_1}{M_2}\right)^2\right] \qquad (2.2)$$

If dΩ is the solid angle spanned by the detector, then $\frac{d\sigma}{d\Omega}$ can be interpreted as the probability that the incident particle will be elastically scattered into the solid angle of the detector and therefore be detected. Equation 2.2 clearly shows that the backscattering yield will be greater with heavier incident ions and heavier target atoms. RBS is much more sensitive for heavy target elements. The yield also increases with decreasing energy, due to the inverse proportionality, and with decreasing scattering angles, due to the inverse proportionality with $\sin^4\frac{\theta}{2}$. Because the probability for scattering, and therefore the height of the signal, is proportional to the square of the atomic number of the target element, the composition of the sample can be determined by the ratio of the heights of the signals divided by the ratio of the atomic numbers.

$$\frac{H_A}{H_B} \bullet \frac{Z_B^2}{Z_A^2} = \frac{N_A}{N_B} \tag{2.3}$$

RBS can also provide a depth profile of the composition of the sample. This is possible because as the He ion moves through the sample it loses energy through inelastic collisions which do not greatly affect its trajectory. An ion which scatters off the surface of the sample has more energy than an ion which travels a distance through the sample before being backscattered. The energy loss, $\frac{dE}{dX}$, of the ion is dependent on the composition of the material through which it is passing. The energy loss is expressed as the volume density of the material, N, multiplied by the stopping cross section, ε. The stopping cross section is tabulated for all elements for a range of incident energies. Determining the energy loss in a compound requires the use of Bragg's rule. The stopping cross section and energy loss are calculated as follows for a compound A_mB_n.

$$\begin{aligned} \varepsilon^{A_mB_n} &= m\varepsilon^A + n\varepsilon^B \\ \frac{dE}{dX}(A_mB_n) &= N^{A_mB_n} \bullet \varepsilon^{A_mB_n} \\ t &= \frac{\Delta E}{N^{A_mB_n} \bullet \varepsilon^{A_mB_n}} \end{aligned} \tag{2.4}$$

Figure 2.3 shows a schematic representation of backscattering from a multilayered thin film system.

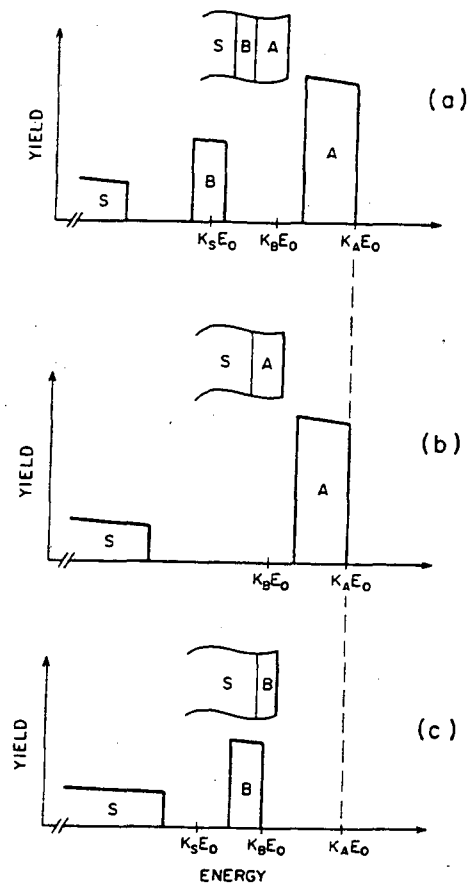

Figure 2.3: Schematic representation of the backscattering spectrum of a bilayered film on a substrate S. The monoisotopic element A is the heaviest, B is intermediate, and S is the lightest. (b) Spectrum for a sample without the intermediate layer B. (c) spectrum for a sample without the top layer A. (Chu, et al. 1978)

This spectrum shows how the presence of an overlayer affects the spectra from the layers underneath. The three labeled energies on the x-axis represent the backscattered energy of the incident ion if those layers were on the surface. The top layer is unaffected and the measured energy is what is expected from the kinematic equation. In figure 2.3a, the energy of the backscattered ions from layer B is not the same as in figure 2.3c when layer B is on the surface. This reduction in energy is due to energy loss as the ions travel through layer A to reach layer B. The ion no longer has energy E_0 when it reaches the

interface between layers A and B, therefore it is backscattered with less energy. The backscattered energy can be calculated if the energy loss through the top film is known.

$$E_1 = K(E_0 - \Delta E_{Ain}) - \Delta E_{Aout} \qquad (2.5)$$

The backscattered ion continues to lose energy as it travels back out of the sample, thus decreasing the measured energy, E_1, even further. Determination of the composition and thickness are not affected.

Figure 2.4 shows an example of how the RBS spectra can change as a new phase forms in a multilayer sample. In this case, Ni was deposited on Si and then annealed at 250°C. At this temperatures Ni_2Si begins forming at the interface between the Si and Ni.

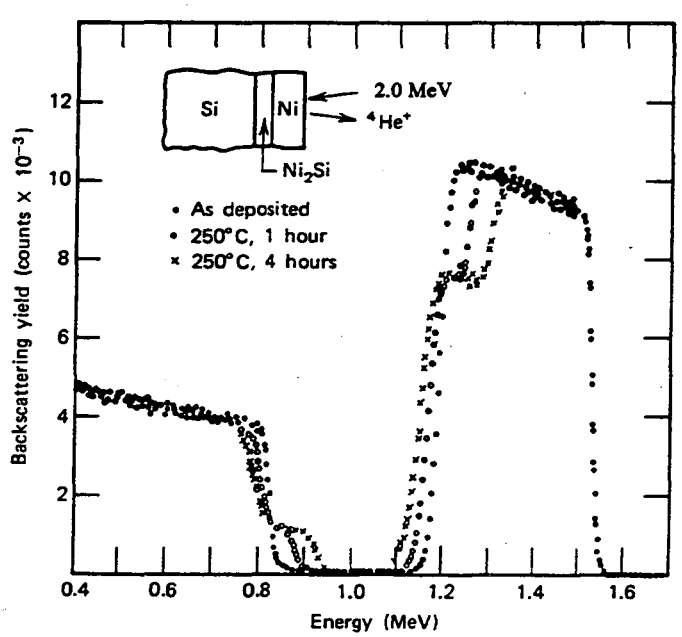

Figure 2.4: RBS spectra of a 2000Å Ni film on Si before and after annealing at 250°C for 1 and 4 hours. (Chu, et al. 1978)

The spectrum taken after annealing for one hour shows a very distinct step down at the end of the Ni signal and a new step at the front of the Si signal. This is a very clear indication that a new layer has formed between the Si and the remainder of elemental Ni. The composition of this new layer can be determined by a ratio of the heights of the two new areas. The thickness can be determined by calculating the energy loss for this region. The abruptness of the steps indicates that the interface is planar over the area within the RBS beam and that there is little diffusion beyond this new layer. The observation that the height of the Ni peak did not decrease anywhere else also indicates that there is no diffusion into the remainder of the Ni. After the sample has been annealed for an additional three hours the new layer grows in thickness, however, the height ratio does not change indicating that the composition of the new layer is still Ni_2Si. The observation of distinct steps in reacted samples is a useful tool for determining the presence and composition of new phases.

2.2 X-ray diffraction

While RBS provides a convenient method for observing diffusion in thin film systems, x-ray diffraction affords an easy method to determine whether the composition is changing only by diffusion or if new phases are forming. The details of x-ray diffraction are covered in depth in a text by B.D. Cullity (Cullity 1978).

When x-rays are incident on a crystal, they can be diffracted by the lattice planes of the crystal. If the wavelength of the radiation is on the order of the spacing between the planes, constructive and destructive interference will take place, as shown in figure 2.5.

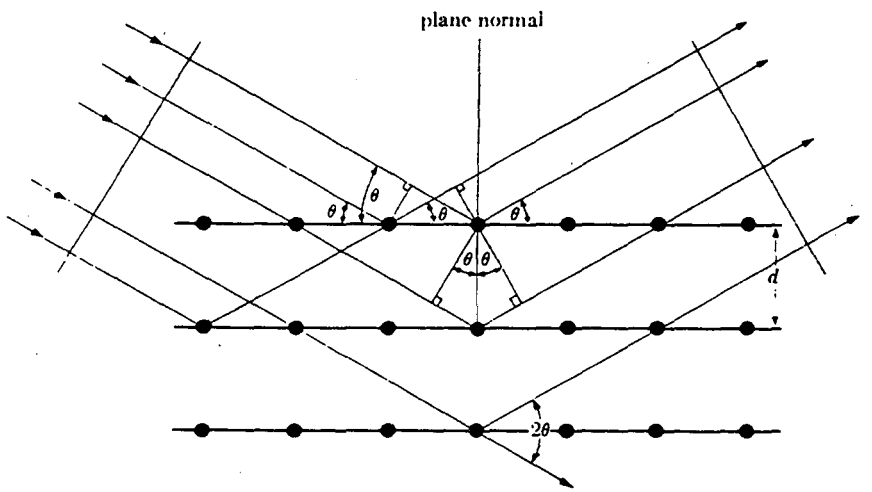

Figure 2.5: Diffraction of x-rays by a crystal (Cullity 1978)

Structure analysis involves using x-rays of a known wavelength and measuring the angle of the constructively diffracted beam. This provides information about the lattice spacing through the application of Bragg's law: $\lambda = 2d\sin\theta$, where d is the lattice spacing. The diffraction angles are determined only by the size and shape of the crystal cell and can easily be calculated using Bragg's law if the crystal structure is known. The intensities of the peaks are more difficult to calculate, because they depend on the positions of the atoms in the cell and the atomic scattering factors of the various elements.

The diagram and formula above give an idealized picture. In a real crystal there are many imperfections which result in variations in peak width and location. The peak width is affected by several variables including the x-ray source size and angular spread, defects,

and strain. The monochromatic x-ray beam which is used is never perfectly monochromatic or parallel. This means that there is some spread in the diffracted beam which increases peak width. Imperfections in the crystal also play a role. Defects, such as dislocations, will cause the diffraction condition to be met for a small spread of angles. Also, if the crystals are too small there will be incomplete destructive interference adding to the width of the peak. As the crystal gets smaller the peak width will increase. The relation between peak broadening, B, and the diameter of the crystal particle, t, is shown below.

$$B = \frac{0.9\lambda}{t\cos\theta} \tag{2.6}$$

The broadening caused by the particle size, B, must be separated from other causes of broadening. This can be done by measuring the peak breadth for the sample, B_M, and for a standard, B_s. The broadening due to particle size can then be determined from the equation below.

$$B^2 = B_M^2 - B_S^2 \tag{2.7}$$

Strain in the crystal also affects the peak. Uniform strain causes the lattice spacing to increase or decrease, thus shifting the peak, while nonuniform strain causes some lattice spacings to increase while others decrease or do not change. This results in an increase in peak width. The relationship between the nonuniform strain and the peak width is given below.

$$B = \Delta 2\theta = -2\frac{\Delta d}{d}\tan\theta \tag{2.8}$$

Deconvoluting all of these contributions to the peak width is difficult. In most cases a sample will exhibit broadening due to the particle size and strain, in addition to the inherent instrumental broadening. If the instrumental broadening is known, then these contributions can be separated using a Fourier analysis technique initially developed by Scherrer (Klug and Alexander 1974; Warren 1969). These mathematical methods were developed for powder diffraction.

X-ray analysis is used to determine whether new phases have formed or only diffusion is taking place. When a metal is deposited near room temperature it is generally polycrystalline. An x-ray spectrum will show several peaks corresponding to different lattice spacings. If diffusion is taking place, the peaks of the metal element will shift as the addition of a new element causes an increase or decrease in the lattice parameter. If a new phase forms, the peaks indicative of the metal element will decrease while new peaks corresponding to the new phase will begin to grow. All of the experimentally measured, and some calculated, x-ray spectra are catalogued in the powder diffraction data file. This aids in the identification of phases because it is not necessary to calculate the spectrum from the crystal structure in most cases.

Most x-ray structure analysis is performed in a diffractometer with the geometry shown in figure 2.6. In a diffractometer, x-rays with a known wavelength are incident on a sample with unknown crystal structure. The angles of the diffracted beams are then measured and the crystal structure can be determined.

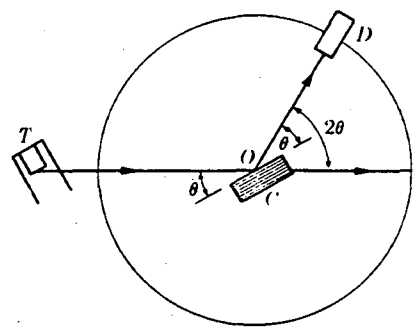

Figure 2.6: The x-ray spectrometer, Bragg-Brentano configuration (Cullity 1978)

The configuration shown in figure 2.6 is called a Debye-Scherrer camera or the Bragg-Brentano configuration. The detector and sample are coupled so that rotating the detector by 2x degrees causes the sample to rotate by x degrees. (For this reason it is also commonly called θ-2θ diffraction.) This coupling preserves focusing conditions and assures that all diffraction peaks are measured. This geometry works well for most applications, but it is not optimum for analysis of thin film systems on single crystal substrates. Because the film can be very thin, the diffracted intensity will be small and perhaps undetectable. Also, when using a single crystal substrate the diffracted intensity from the substrate will be very large and overwhelm all other signals.

To overcome these disadvantages a Read camera is often used to analyze thin film systems. Figure 2.7 shows the glancing angle geometry of this diffractometer. In this case the x-ray source and sample are held fixed and only the detector is rotated. The x-ray beam is incident on the sample at a small (usually 1°-3°) angle. This increases the path length of the x-rays in the thin film and thus increases the intensity of the diffracted

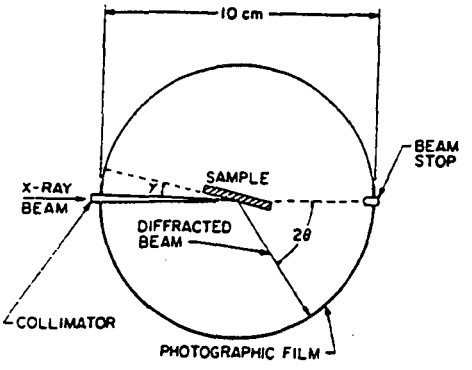

Figure 2.7: Schematic diagram of the geometry of the Read camera (Lau, et al. 1974)

beam. The Read geometry still limits detection to films thicker than approximately 200-500Å (Lau, et al. 1974). This geometry also never satisfies the diffraction conditions for the single crystal substrate, so these peaks will not overwhelm the signal from the thin film. This can be a disadvantage. However, if the new phase is epitaxial with the substrate the diffraction pattern may show no peaks at all.

2.3 Complementary techniques

RBS and x-ray diffraction provide much useful information regarding the development of the thin film system. They do not easily provide information on lateral uniformity or morphology at the interface, and the depth resolution is limited to approximately 100 Å. Also, these techniques can not identify low level contaminants in the system or on the surface.

2.3.1 Transmission Electron Microscopy (TEM)

TEM is a very complex, far-reaching technique and it can provide a great deal of high-spatial-resolution information. It is, however, a very time and labor intensive technique and it is much better to use other techniques first to determine the basic characteristics of the system. It is also important to remember that it only analyzes very small volumes of material. Only the very basic issues which apply to the characterization used in this study will be discussed here. In the TEM, a monoenergetic beam of electrons is impinged upon a very thin sample. The electrons are diffracted as they travel through the material. Electromagnetic lenses are then used to focus the electron beams into a diffraction pattern or an image. This diffraction pattern provides information about crystal structure, much in the same way as x-ray diffraction. The image of the sample can provide information about morphology, crystal structure, and epitaxy on an atomic scale. At the highest magnifications, the epitaxial relations between the substrate and the film can be observed. TEM provides a method to observe the lateral uniformity of the system and verify phase formation and epitaxial relationships.

2.3.2 X-ray Photoelectron Spectroscopy (XPS or ESCA)

In XPS, electrons are ejected from the sample due to bombardment by monoenergetic x-rays. This is primarily a surface technique because the photoelectrons can only escape

from approximately 2-20 atomic layers. The kinetic energy of the ejected electron depends on the energy of the x-ray and the binding energy of the electron.

$$KE = h\upsilon - BE \qquad (2.9)$$

The binding energy differs depending on which element the electron was ejected from. Thus, a measurement of the kinetic energy and a knowledge of the x-ray energy allows the determination of the composition. The binding energy changes slightly depending on the bonding configuration of the atom. By measuring the chemical shift it is possible to determine what chemical environment the atom is in. Depth profiling can be done by sputtering the sample and then sampling the newly exposed surface. This may not give a valid picture of sample composition because of differential sputtering rates. The sensitivity of XPS is between 0.01 and 0.3 % depending on the element observed. XPS is a useful technique for observing the presence of contaminants or oxides on the surface of a sample.

3. Metal contacts on semiconductors

Contact behavior is interesting from a scientific standpoint because metal-semiconductor reactions affect the electrical behavior of the contact. The studies of Pt and Pd on Si and GaAs have aided in the development of theories for determining Schottky barrier heights. Gaining information on how these barriers form on ZnSe will help determine which theories are correct and promote the development of new contacts.

Many characteristics affect the quality of a metal contact. A contact for a device must provide the proper electrical behavior, have a shallow depth and lateral uniformity, and be resistant to mechanical stresses. In the case of II-VI materials, the metal must be very ductile or well-matched in thermoelastic properties to prevent injection of defects inoth the II-VI material. The contact must also not degrade due to thermal stresses or ambient exposure. In order to understand how a contact will behave during use, it is vital to study its thermal stability and electrical behavior. Pt and Pd contacts on Si and GaAs have been studied in depth because they have been widely used in devices. In-depth studies of thermal stability and phase formation for contacts on ZnSe have not been done, partially because of the lack of high quality material for practical device development. As more devices are developed, it is essential to increase the understanding of contact systems on this semiconductor.

3.1 Overview of Pt and Pd silicides

Aluminum provides low resistivity, good processability, and was until recently almost exclusively used as a metal contact on Si until decreasing device dimensions caused

problems due to electromigration and spiking of aluminum through the contact. Investigations began to focus on the behavior of metal silicides as an alternative to aluminum contacts. Silicides are now often used for reliable Ohmic contacts and Schottky diodes. They are used in a multilayer structure with Al. The silicide acts as a contact layer and diffusion barrier between the Si and the Al interconnect. Pt and Pd silicides in particular have generated interest because of their good thermal and electrical stability.

3.1.1 Phase formation behavior

Pt has been observed to react with underlying Si to form Pt_2Si at temperatures as low as 200°C (Muta and Shinoda 1972). The Pt_2Si grows until all of the Pt has been consumed (Canali, et al. 1977; Crider and Poate 1980; Hiraki, et al. 1971; Wittmer 1983). PtSi then begins growing from the Pt_2Si-Si interface, until all of the Pt_2Si is consumed. The RBS spectra in figure 3.1 show the stages of the reaction for isothermal anneals at 350°C.

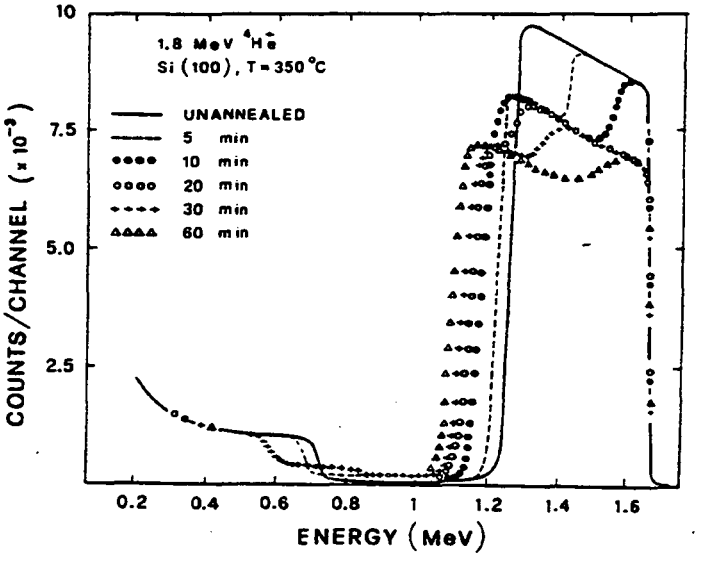

Figure 3.1: Backscattering spectra of samples annealed at 350°C for different times. The as-deposited Pt layer is 2700Å thick. For clarity in the silicon spectra, only a few cases are reported. (Canali, et al. 1977)

The first distinct step down in the RBS spectra indicates the formation of a Pt_2Si layer. The final lower and wider step indicates a one to one ratio of Pt and Si in the final phase. A thin layer of SiO_2 has been observed to cover the PtSi layer after annealing (Bindell, et al. 1976; Poate and Tisone 1974; Rand and Roberts 1974). This has been observed in RBS spectra, Auger spectra, and etching behavior. A slight depression in the Pt signal at the surface has been seen in RBS spectra and interpreted as an oxide layer at the surface (Bindell, et al. 1976). This interpretation is supported by an O surface signal which appears in an Auger spectrum of annealed PtSi. Rand and Roberts (Rand and Roberts 1974) propose that this is due to fast Si diffusion along the grain boundaries to the surface where it is oxidized. They observed that PtSi is easily etched by aqua regia only if this oxide layer is first removed by a buffered HF etch.

The activation energies for the growth of Pt_2Si and PtSi are very similar and have been reported between 1.3 and 1.6 eV (Bindell, et al. 1976; Canali, et al. 1977; Crider and Poate 1980; Poate and Tisone 1974; Wittmer 1983). Figure 3.2 shows data for the growth rates of the two phases as determined by several groups. The growth rates are the same regardless of the substrate orientation (Canali, et al. 1978; Poate and Tisone 1974; Wittmer 1983). The growth of Pt_2Si follows an $X^2 = Dt$ relationship, where X is the film thickness, D the diffusivity, and t the time. PtSi follows an $X^2 = D(t - t_o)$ relationship where t_o is the time required for the growth of the Pt_2Si layer (Crider and Poate 1980). This square root of time dependence is indicative of a diffusion limited growth process. The heat of formation of Pt_2Si is higher than PtSi, therefore the initial

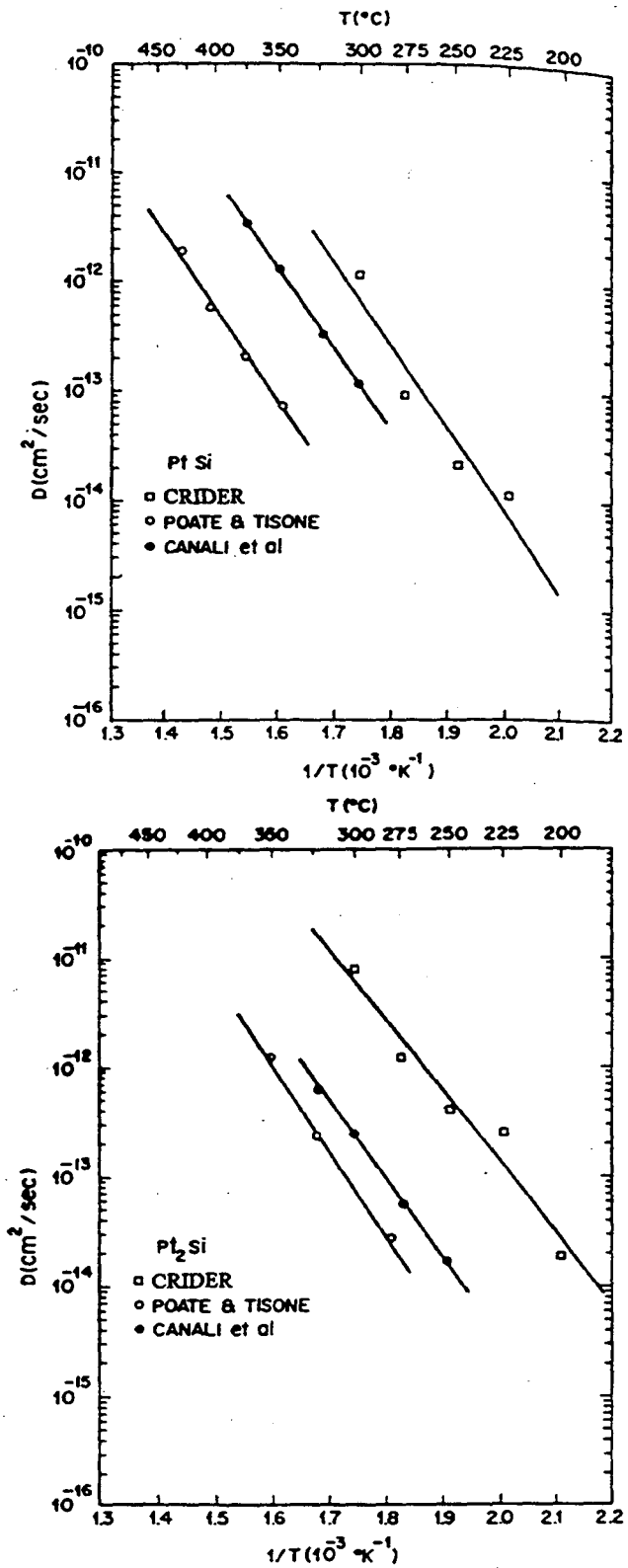

Figure 3.2: Arrhenius plots for Pt silicide growth from several comparable works. Clean Pt films on Si were deposited at 25Å/minute on room temperature substrates and annealed in UHV. (Crider and Poate 1980)

growth process must be dominated by reaction kinetics rather than thermodynamics since the Pt_2Si grows first (Canali, et al. 1978). An experiment utilizing radioactive ^{31}Si was used to determine that Pt is the diffusing species in this reaction (Pretorius 1981). The radioactive Si decays by the emission of a beta-particle with a half life of approximately 2.6 hours. This means that all experiments must be performed within a time window of about 15 hours, while there is still enough radioactivity to measure. A layer of ^{31}Si was deposited before the Pt layer and then the system was annealed. The activity profile measured after annealing indicated that the majority of the ^{31}Si was segregated to the surface, indicating that the metal is the diffusing species (Comrie and Egan 1988).

Some studies reported the initiation of growth of the second phase, PtSi, before the complete consumption of Pt by Pt_2Si (Bindell, et al. 1976; Muta and Shinoda 1972; Poate and Tisone 1974). This was most likely due to the presence of impurities at the interface or in the deposited Pt. Crider, et al. (Crider and Poate 1980), showed that as the Pt_2Si phase grew, impurities such as O and Al were segregated to the Pt-Pt_2Si interface. Figure 3.3 is an Auger spectrum indicating the expulsion of O from the Pt_2Si phase. Canali, et al. (Canali, et al. 1977), postulated that the accumulation of impurities may have hindered the Pt_2Si growth and allowed PtSi to begin growing before complete consumption of the Pt. Crider and Poate (Crider and Poate 1980) indicated that various surface conditions do not greatly affect the phase sequence, therefore this effect must be due to impurities within the Pt film. In their studies, higher O_2 contamination of the Pt resulted in lowered diffusivities

(D) for both Pt_2Si and PtSi, and therefore slower growth rates. A sufficiently high level of contamination resulted in a PtSi layer growing before the Pt was completely transformed

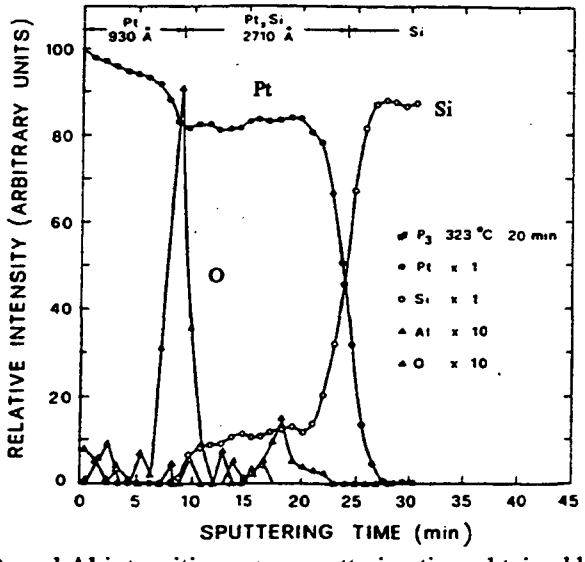

Figure 3.3: Pt, Si, O, and Al intensities versus sputtering time obtained by Auger spectroscopy in a Si (bulk)/Pt_2Si/Pt structure. (Canali, et al. 1977)

to Pt_2Si.

A preferred orientation of PtSi films has been observed in a few studies (Nemanich, et al. 1987; Sinha, et al. 1972). This orientation seems to be dependent on the thermal history, mode of preparation, and orientation of the substrate. A preferred orientation appeared in silicide films which were annealed at temperatures of about 300°C and transformed directly to PtSi.

Pd silicides have also been used as Schottky barriers and Ohmic contacts. Pd_2Si provides an alternative to PtSi. Their electrical behavior is similar, however Pd_2Si is stable up to 700°C, it can be fabricated at lower temperatures, and the etchant used to remove excess Pd is less corrosive and is compatible with photoresist. The formation of Pd_2Si has

been reported during deposition at room temperature (Buckley and Moss 1972; Fertig and Robinson 1976; Ho, et al. 1979). Pd_2Si is usually formed by annealing at 100-200°C.

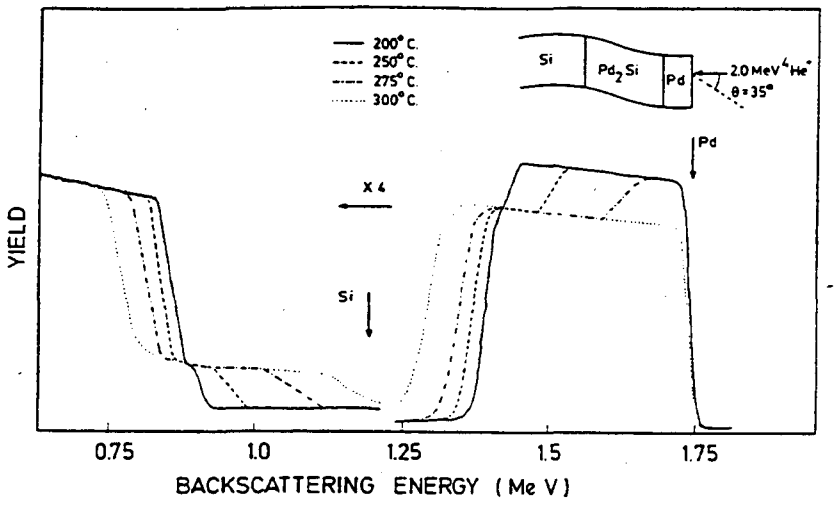

Figure 3.4: RBS spectra for Pd on Si annealed at 200, 250, 275, and 300°C for 30 minutes. (Clement, et al. 1988)

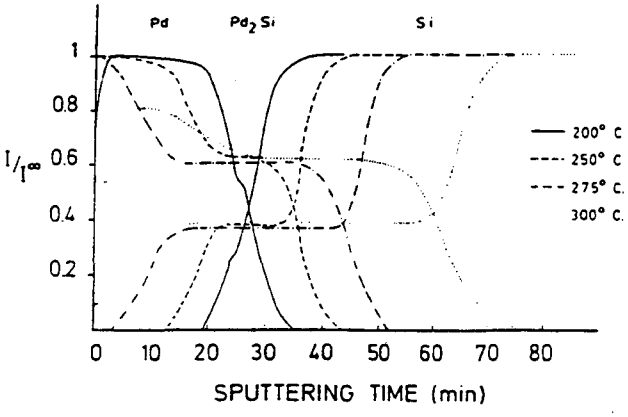

Figure 3.5: Auger spectra for Pd on Si annealed at 200, 250, 275, and 300°C for 30 minutes. (Clement, et al. 1988)

The RBS and Auger spectra in the figures above show the growth of Pd_2Si during isochronal anneals. The distinct steps in the RBS spectra clearly indicate the composition

and thickness of the newly formed phase. Note that the Pd_2Si-Si interface remains very abrupt during growth, while the Pd-Pd_2Si interface becomes more sloped as the reaction proceeds. The more sloped region indicates a diffusion gradient and thus a wider interface. This may be due to differing growth rates between crystallites (Clement, et al. 1988).

Pd_2Si is stable up to approximately 700°C, when PdSi nucleates at damaged areas along the substrate surface. PdSi can also be formed directly from the Pd-Si structure by annealing at temperatures between 735 and 840°C. Extended annealing at high temperature results in a microstructure of PdSi islands (Hutchins and Shepela 1973).

The activation energy for Pd_2Si growth has been measured at approximately 1.4 eV by several groups (Fertig and Robinson 1976; Little and Chen 1988) as shown in the

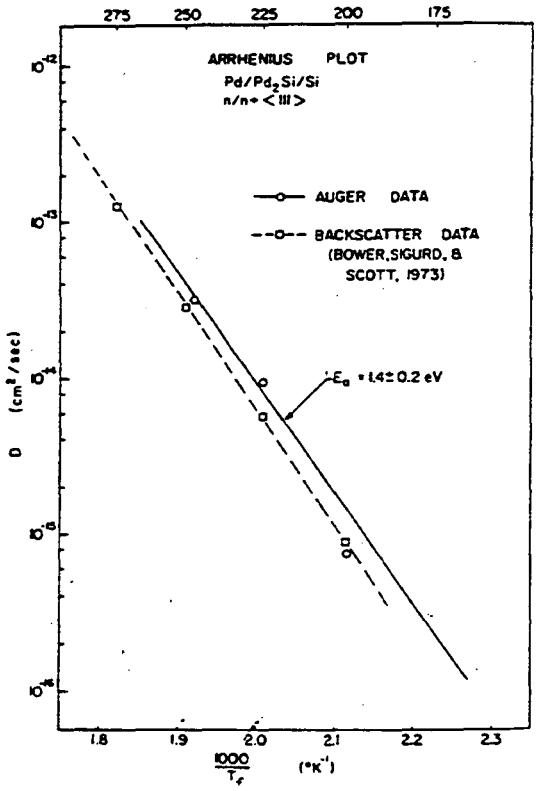

Figure 3.6: Arrhenius plot of the diffusion coefficient, D, characterizing the formation of Pd2Si on <111> Si. The AES data is fitted by the solid line with slope proportional to E_a=1.4±0.2 eV. for comparison, the broken line and associated data points were found from the study by Bower, et al. (Fertig and Robinson 1976)

Arrhenius plot above. The growth rate is independent of substrate orientation. The presence of an oxide between the substrate and Pd caused a delay in the onset of silicide formation, but once the silicide formed, the rate of growth was the same (Bower, et al. 1973).

Pd_2Si growth also follows a $X^2 = Dt$ dependence. Figure 3.7 shows the linear dependence of thickness squared with annealing time for various temperatures and substrate orientations.

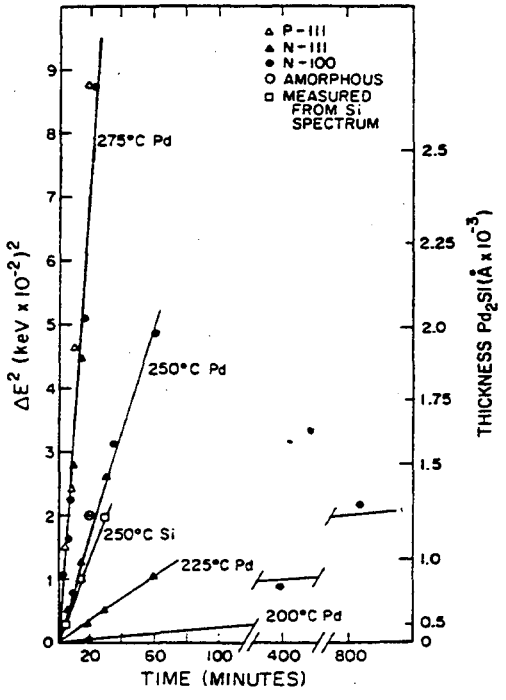

Figure 3.7: The figure shows the square of the energy loss ΔE in the silicide region (left scale) and the corresponding Pd2Si thickness (right scale) as a function of heat treatment time. Data points for four temperatures and a variety of Si substrates are presented. The horizontal scale is segmented at two points. (Bower, et al. 1973)

This dependence indicates that the formation of this silicide is also diffusion dependent. Radioactive Si tracer experiments have shown that an initial layer of ^{31}Si between the

substrate and Pd results in a uniform distribution of ^{31}Si in the silicide phase (Comrie and Egan 1988). This indicates either Si diffusion during growth or a high self-diffusion rate of Si in the Pd_2Si. Supporting experiments show that Si does not have a high self-diffusion rate at the temperatures used, therefore the ^{31}Si must diffuse by the vacancy mechanism during silicide formation.

Pd_2Si films often grow with a preferred orientation. Oriented grains are observed in silicides grown on <100> and <110> oriented substrates and Pd_2Si grows epitaxially on <111> oriented substrates. Channeling experiments have shown that the film is most epitaxial on <111>, while the film is least oriented when grown on amorphous substrates(Bower, et al. 1973; Hutchins and Shepela 1973; Sigurd, et al. 1974). This

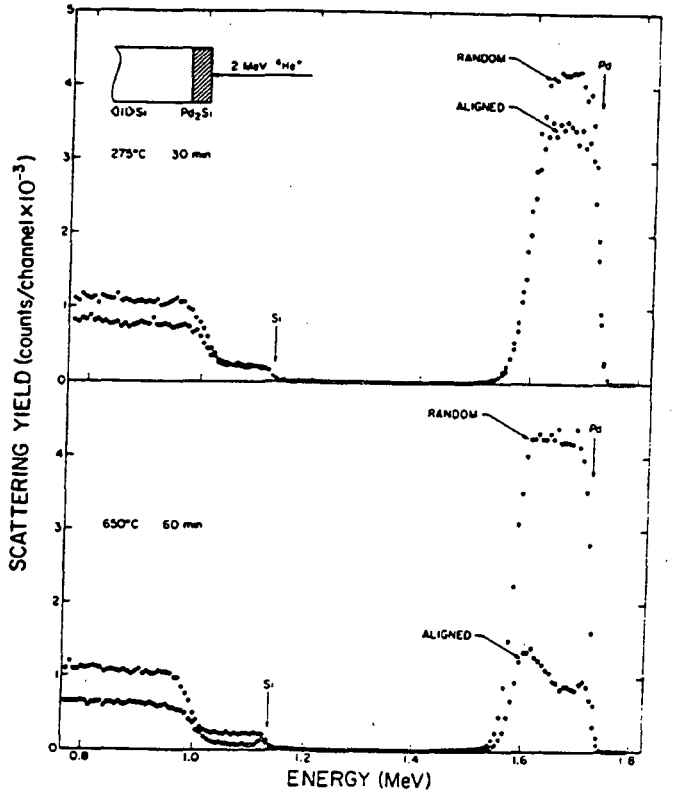

Figure 3.8: Random (•) and aligned (O) energy spectra for 2 MeV 4He ion scattering from Pd_2Si layers on <111> Si substrates. The upper spectra are for a sample heat treated at 275°C for 30 minutes. The lower spectra are for a sample heat treated at 650°C for 60 minutes. Arrows indicate energies for scattering from surface atoms. (Sigurd, et al. 1974)

epitaxial alignment becomes more pronounced for anneals at higher temperatures, as shown by the channeling data above. The variation in preferred orientation is also seen in the relative full width half maximum (FWHM) of the primary x-ray peak. The FWHM is only 1.3° for the silicide on the <111> oriented substrate, while it increases to 10.5° for the <110> and <100> oriented substrates, and 18° for a film grown on the amorphous substrate (Bower, et al. 1973). The relative crystalline perfection of this silicide affects its stability at high temperatures. PdSi nucleates at lower temperatures on Pd_2Si grown on <110> and <100> substrates. It also nucleates uniformly along the sample surface, whereas on the <111> oriented sample PdSi nucleates only at damaged areas.

3.1.2 Electrical Characteristics

The electrical behavior of PtSi is of special interest because it is stable up to high temperature. The barrier height of Pt on n-type Si is 0.9 eV (Sze 1981). After annealing the Schottky barrier height decreases to 0.87 eV when PtSi forms at the interface (LaVia, et al. 1988; Ohdomari and Tu 1980; Toyama, et al. 1985). The sheet resistivity of PtSi is $15\pm5\mu\Omega$cm (Sinha, et al. 1972). Annealing PtSi causes this resistivity to decrease slightly and then increase dramatically as shown in figure 3.9. The decrease is attributed to grain growth and a decrease in the grain boundary contribution to resistivity. The final increase is seen mainly in thin films (~20nm) and is due to agglomeration which causes voids in the film.

One of the reasons Pd_2Si can be substituted for PtSi is that their barrier heights are similar. As deposited, Pd on n-type Si gives a barrier height of 0.86 eV. After annealing, the formation of Pd_2Si results in a decrease of the barrier height to 0.74 eV (Fertig and

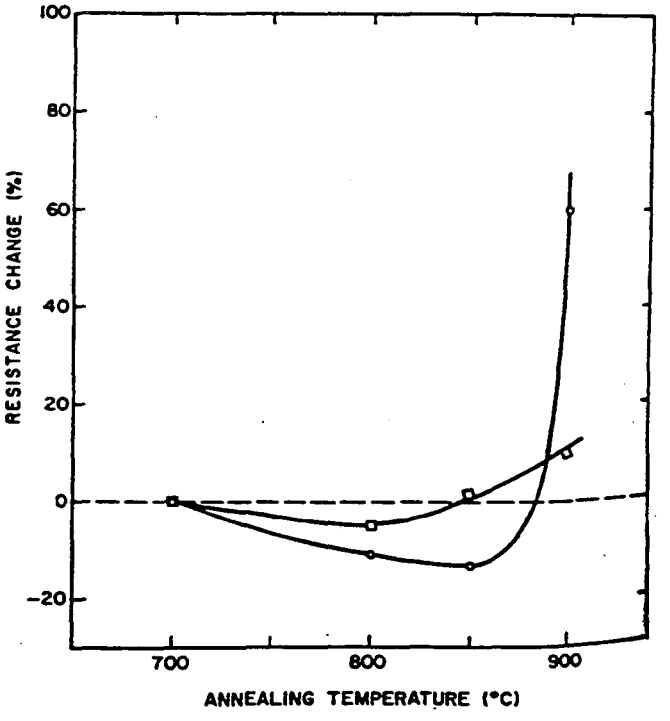

Figure 3.9: Change in sheet resistance of PtSi films vs. annealing temperature. The annealing was done for 10 minutes at 700°C, and 1 hour each at 800, 850, and 900°C. □ represents 900Å thick PtSi and O represents 200Å thick PtSi. (Sinha, et al. 1972)

Robinson 1976; Okumura and Tu 1983). This decrease may be due to part of the contact initially being covered by a native oxide, which is reduced during annealing. Figure 3.10 shows typical C-V data for a Pd_2Si contact. This data gives a barrier height of 0.74 eV. The observed dependence of the current density on the applied voltage indicates that thermionic emission is the dominant current flow mechanism (Kircher 1971). The

measured sheet resistance for Pd_2Si is 40 $\mu\Omega$cm and the contact resistance is 4 $\mu\Omega cm^2$ (Kircher 1971) for a doping level of $2x10^{20}$ cm^{-3}.

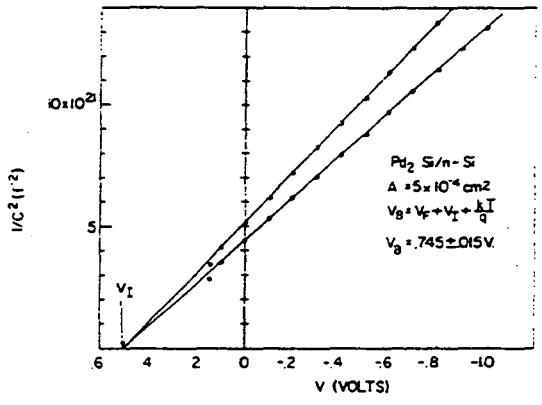

Figure 3.10: Capacitance-voltage data for reverse biased Pd_2Si/Si diodes. (Kircher 1971)

3.2 Overview of Pt and Pd on GaAs

Contacts for GaAs applications have grown in importance as GaAs has become more widely utilized. In order to guarantee the continued performance of these systems, it was vital to understand the stability of these metal systems. Near-noble metals have been used for contacts because of their ease of deposition, low reaction temperature with GaAs, ability to form compounds with GaAs, and resistance to oxidation.

3.2.1 Phase formation behavior

Pt/GaAs contacts have been widely used as Schottky barriers in Impatt diodes for microwave applications (Poate, et al. 1978). The degradation of these diodes and increased barrier heights have been observed after annealing. This is due to the

interdiffusion and phase formation taking place in the system. At temperatures as low as 250°C shifts of the Pt x-ray peaks are observed as Ga diffuses into the Pt and changes the lattice parameter. This is followed by precipitation of a $PtAs_2$ phase at the interface and Pt_3Ga in the Pt film (Fontaine, et al. 1983; Kumar 1975; Murarka 1974). The diffusion of Ga slows down dramatically as it has to diffuse through the $PtAs_2$ layer. Ga continues to slowly diffuse through into the Pt, and at completion of the reaction a layered structure exists with $PtAs_2$ in contact with the GaAs, and a PtGa layer on top. Films greater than 0.2μm do not react to completion because of the inability of Ga to diffuse through the $PtAs_2$ layer. The x-ray spectra below shows the phase progression during the reaction and the RBS data shows the depth distribution of the components.

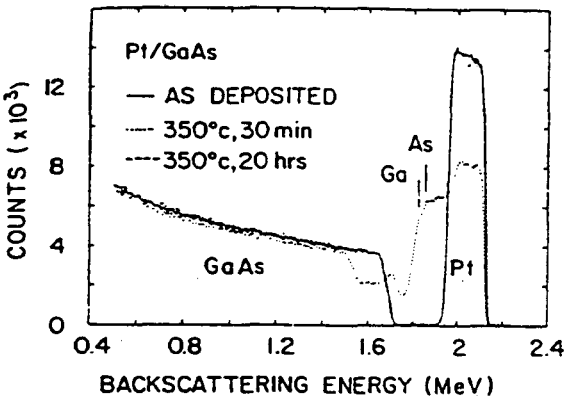

Figure 3.11: RBS spectra using 2.3 MeV $^4He^+$ ions of 1000Å Pt/<100> GaAs sample before and after annealing. (Fontaine, et al. 1983)

The RBS spectra in figure 3.11 shows that a large amount of GaAs is consumed in the reaction. Several studies have shown that for a complete reaction, the thickness of GaAs

consumed is approximately twice the thickness of the Pt film (Kumar 1975; Sinha and Poate 1973). Fontaine, et al. (Fontaine, et al. 1983), suggested that the $PtAs_2$ may form next to the GaAs because this interface has a lower free energy than a GaAs-PtGa interface. Sands, et al. (Sands, et al. 1987b), postulated that this stratification was simply due to the relative diffusivities of the various elements. Ga diffuses much more quickly than As, and thus can diffuse into the Pt in much greater quantity. They supported this by the observation that if a native oxide is present, that oxide remains between the $PtAs_2$

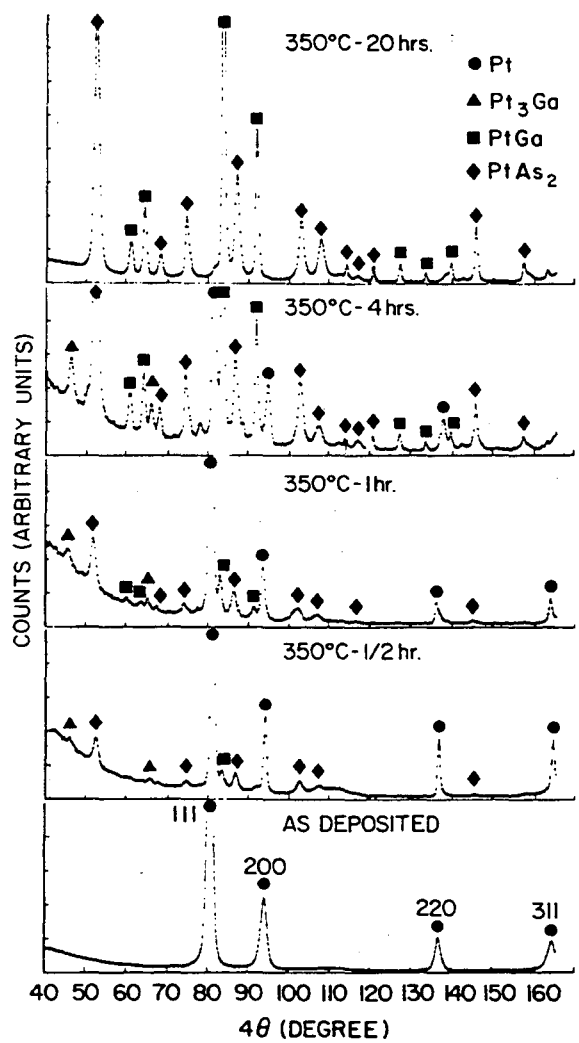

Figure 3.12: Glancing angle Seeman-Bohlin x-ray diffraction spectra of a 1000Å Pt/<100> GaAs sample before and after annealing. (Fontaine, et al. 1983)

layer and the PtGa layer. This indicates that the Ga is diffusing out of, while the Pt is diffusing into the GaAs. The presence of a native oxide does not affect the rate of reaction. Etched, unetched, and backsputtered samples all behaved similarly (Murarka 1974). The reaction was slowed, however, if the samples were pre-annealed in air (Kumar 1975). Ellipsometry measurements of the oxide showed that the thickness only increased by approximately 5 Å, but the oxide became denser. This pre-annealing did not change the final products of the reaction, it only slowed the onset.

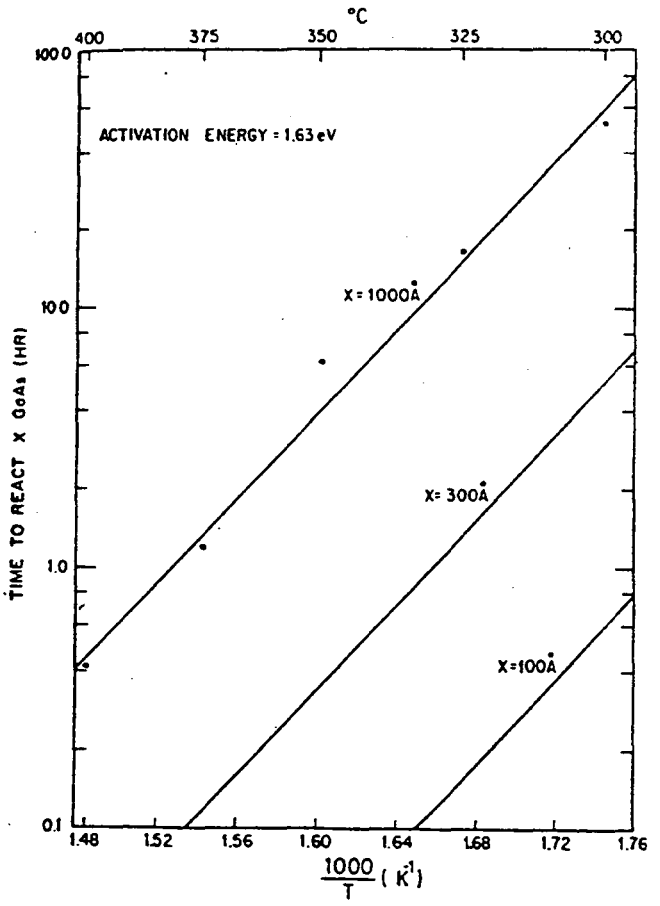

Figure 3.13: Arrhenius plot for the time to react a specified amount of GaAs with Pt. (Coleman, et al. 1974)

Measurements of the activation energy are not in complete agreement. Coleman, et al.(Coleman, et al. 1974), measured the growth rate for various thicknesses and temperatures. The Arrhenius plot of their data is shown in figure 3.13. They determined an activation energy of 1.63 eV. Kumar (Kumar 1975), however, found an activation energy of 2.3 eV.

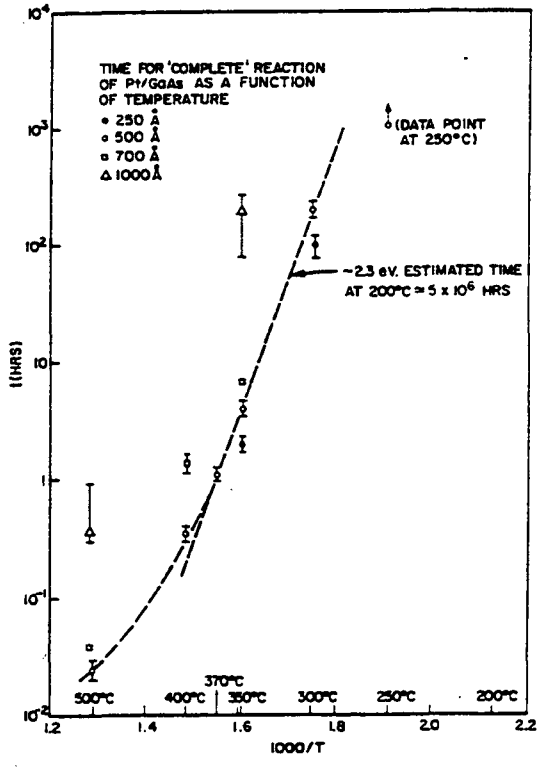

Figure 3.14: Time for complete reaction of Pt/GaAs as a function of temperature. (Kumar 1975)

He observed that the reaction times do not all lie on a straight line, thus implying that this is not a singly thermally activated process. Other groups also observed that at low temperatures the reaction took a very long time (Murarka 1974). At temperatures

between 200 and 250°C, the process was observed to take approximately 100 hours. The reaction is seen to follow a $X^2 = Dt$ dependence, indicating that it is also diffusion limited (Coleman, et al. 1974). Some texturing of the $PtAs_2$ was observed, however the film is not epitaxial (Fontaine, et al. 1983; Sands, et al. 1987b).

A number of Ohmic contacts to GaAs have been developed using Pd as well. Early studies of the Pd-GaAs interface system detected the presence of $PdAs_2$ and PdGa phases after annealing at temperatures below 350°C (Olowolafe, et al. 1979; Oustry, et al. 1981). These phases were identified through the use of x-ray diffraction. Figure 3.15 shows an RBS spectrum after annealing at 500°C. The very slanted profile makes it difficult to estimate compositions or determine if these binary phases are present.

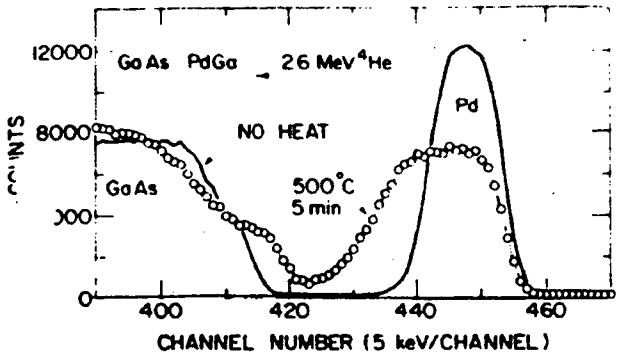

Figure 3.15: He-ion backscattering spectra for a Pd/GaAs sample before and after annealing at 500°c for 5 minutes. (Olowolafe, et al. 1979)

Further studies utilizing tools such as TEM and energy dispersive spectroscopy showed that rather than $PdAs_2$, ternary PdGaAs phases were formed. At temperatures below 250°C a hexagonal, oriented ternary phase is nucleated (Delrue, et al. 1985; Kuan, et al. 1985; Lin, et al. 1988; Oelhafen, et al. 1983; Sands, et al. 1985; Sands, et al. 1987a). This phase, designated phase I, has the approximate composition $Pd_5(GaAs)_2$. The x-ray

peaks from this phase coincide with the major peaks from $PtAs_2$ which may explain the earlier misassignment. The exact composition is still under debate and the phase appears to exist under a range of compositions (Sands, et al. 1987a). Sands, et al. (Sands, et al. 1987a), reported that this phase forms in grains which are each slightly misoriented and do

Figure 3.16: Cross-sectional TEM micrograph of phase I layer formed during deposition of Pd onto (100) GaAs. (Sands, et al. 1987a)

not make a complete layer at the interface. The native oxide layer is visible above this ternary layer and does not inhibit the reaction (Lin, et al. 1988). Above 250°C a second ternary phase, phase II, nucleates at large-angle grain boundaries in the phase I film (Lin, et al. 1988; Sands, et al. 1987a). This phase is not epitaxial, and with annealing at higher temperatures is the only phase observed. Its composition is not fixed and ranges between Pd_2GaAs and Pd_4GaAs. Finally, at anneals above 400°C a PdGa phase grows as the As:Ga ratio drops due to sublimation of As from the film. The final products in this reaction are dependent on the annealing ambient. Films annealed in vacuum lose more As and are dominated by a PdGa phase, while films annealed in forming gas have more As retained and the ternary phase is still observed (Kuan, et al. 1985). The final components

of films annealed with an SiO_2 cap are PdGa and $PdAs_2$ (Yu, et al. 1986), because little As is lost during annealing. Yu, et al., (Yu, et al. 1986) also report that there is some stratification of the two phases, with the surface region being PdGa rich, while the interface region is $PdAs_2$ rich.

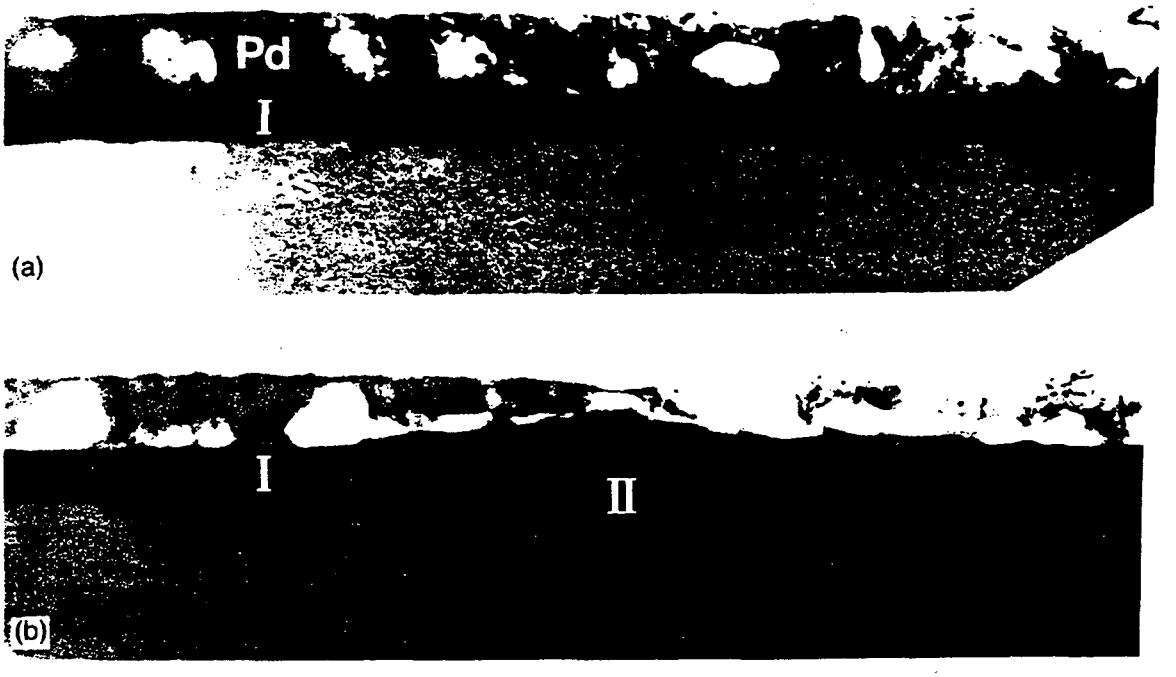

Figure 3.17: Cross-sectional TEM images showing phase II penetration. (Sands, et al. 1987a)

Activation energies for these reactions were not measured. The native oxide layer which is seen above phase I disperses and voids are visible above the layer after annealing at 220°C. This indicates that the Pd is the moving species at low temperature (Sands, et al. 1987a). Olowolafe, et al., (Olowolafe, et al. 1979) observed that there is simultaneous interdiffusion of Pd, Ga, and As. Their Auger spectra, shown in figure 3.18, indicate outdiffusion of both Ga and As along with penetration of Pd into the GaAs layer.

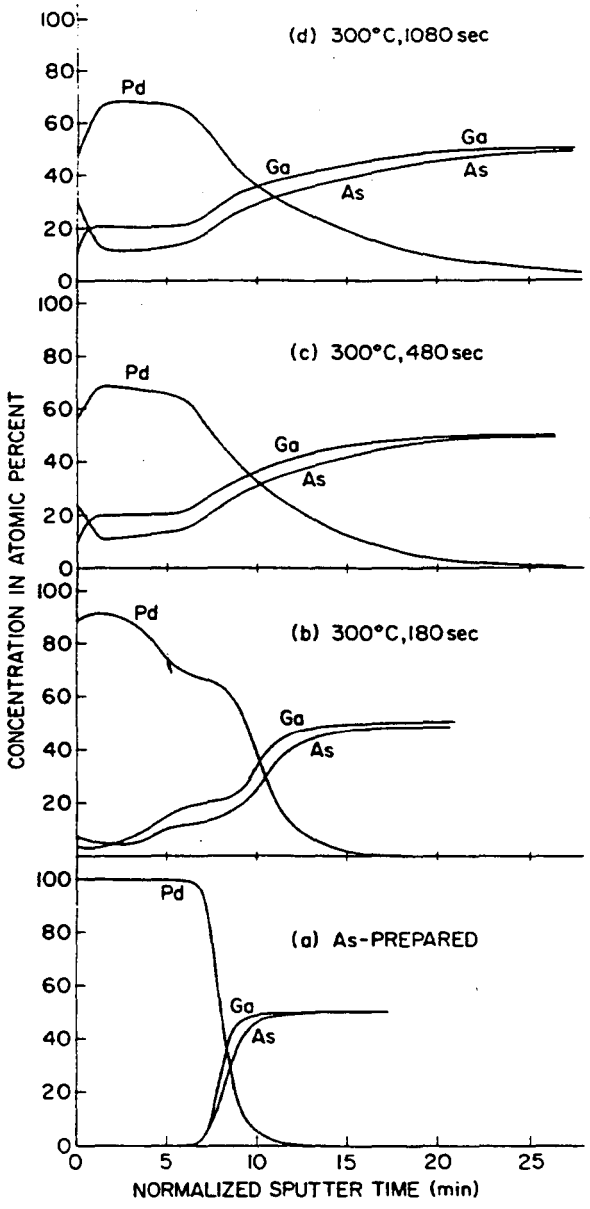

Figure 3.18: A series of Auger sputter profiles showing contact reactions in Pd/GaAs junctions as a function of annealing time at 300°C. (Olowolafe, et al. 1979)

3.2.2 Electrical Characteristics

The electrical behavior of Pt on GaAs has been studied in great detail in an attempt to help develop models of Schottky barrier formation. Unlike Pt on Si, the barrier height for Pt on n-type GaAs increases after annealing. As deposited Pt on n-type GaAs has a barrier height of 0.84 eV. After annealing, the barrier height increases to 0.89 eV due to the formation of $PtAs_2$ at the interface (Sinha and Poate 1973; Sze 1981) and the dispersion of any oxide (Yu, et al. 1987). Pt on p-type GaAs has been reported to form a good Ohmic contact (Okumura and Tu 1987; Poate, et al. 1978). The barrier height has also been reported at 0.48 eV (McCants, et al. 1987) for a 0.67 monolayer coverage. Theoretically the barriers on n-type and p-type should add up to the band gap energy, therefore the p-type barrier height is expected to be 0.5 eV. The lower barrier may mean that the pinning levels are different between n and p type (Okumura and Tu 1987). The initial barrier height on n-type GaAs has been observed in systems with a coverage of less than one monolayer (McCants, et al. 1987). Aydinli and Mattauch (Aydinli and Mattauch 1982) report that the barrier height is also dependent on the initial surface termination of the GaAs. Surfaces which are Ga rich have a higher barrier height than those that are As rich. The barrier height has also been measured using the photoresponse technique (Fontaine, et al. 1983; Okumura and Tu 1987), in this case the barrier height was measured to be 0.9 eV both as deposited and after annealing. These groups argue that this method is more accurate because it is not affected by defects at the interface.

Murarka (Murarka 1974) has shown that continued annealing of the system causes a degradation of the barrier. This is not due to continued reaction at the interface, but

instead to diffusion of oxygen through the Pt layer and into the GaAs. The oxygen acts as a deep donor. Systems which are annealed in vacuum, rather than air, do not exhibit this degradation. The sheet resistivity also changes with annealing time as shown in figure 3.19.

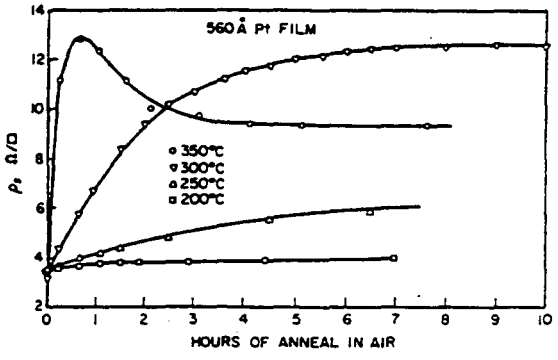

Figure 3.19: Sheet resistivity of platinum film on *n*-GaAs as a function of time of anneal in air at different temperatures. (Murarka 1974)

These results show that at 350°C the reaction to form $PtAs_2$ and $GaPt_3$ is very fast. The resistivity then decreases slowly as the reaction proceeds towards completion and the final products of $PtAs_2$ and GaPt.

The electrical behavior of Pd on GaAs has not been studied in as great a detail. Pd on n-type GaAs forms a barrier height of 0.865 eV, which does not change during anneals up to 350°C (Hokelek and Robinson 1981; Yu, et al. 1987). The barrier height is fixed because the reaction at the interface has already occurred during deposition. Anneals above 350°C cause the degradation of the Schottky contact (Vyatkin, et al. 1981; Yu, et al. 1987). This is due to the precipitation of binary phases and the creation of a laterally irregular interface morphology. Vyatkin, et al. (Vyatkin, et al. 1981), found that when the contact was annealed in a hydrogen atmosphere it could withstand anneals up to 500°C without any contact degradation. The barrier height on p-type GaAs has been

reported to be 0.485 eV (Hokelek and Robinson 1981), and Olowolafe, et al. (Olowolafe, et al. 1979), determined that Pd made a good Ohmic contact to lightly doped ($<10^{18}$ cm^{-3}) p-type GaAs. They reported the contact resistance to be 1.5mΩcm. The Pd sheet resistivity increases with annealing as shown in figure 3.20.

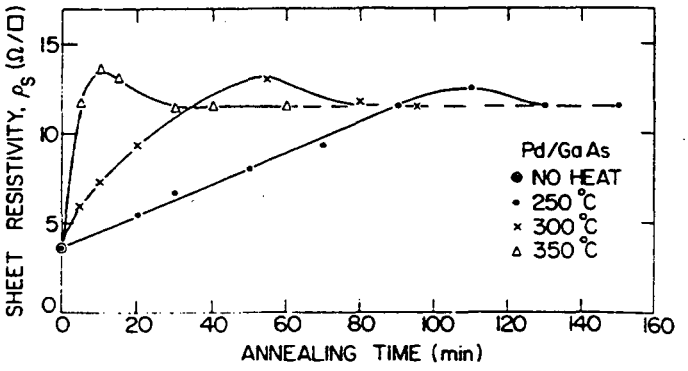

Figure 3.20: A plot of sheet resistivity, ρ, versus annealing time at different temperatures. (Olowolafe, et al. 1979)

The time required to reach the resistivity saturation point corresponds to the time required to complete the Pd-GaAs reaction.

3.3 ZnSe literature review

Unlike the Si and GaAs systems, there is a dearth of information on metal-ZnSe systems. The increased ionic character of the bonding in ZnSe provides a new variable with regard to reaction and Schottky barrier formation. Sands, et al. (Sands and Keramidas 1994), predict that the driving forces for reaction should be smaller than the driving forces for reaction on GaAs. Brillson (Brillson 1982), however, reports that the diffusion coefficients of metal in II-VI's are generally greater than those in III-V's and that

interdiffusion can be substantial even at room temperature for metals on CdS. The diffusion coefficients were measured in bulk ZnSe in the early 1960s and may not reflect the behavior of pure single crystal epitaxial layers. The strength of the chemical bonding between the metal and semiconductor anion will likely determine the extent of reactive anion outdiffusion and the concentration of dissociated cations near the interface (Brillson 1982). Electrically, the wide band gap causes problems for forming good Ohmic and Schottky contacts. Ohmic contacts to p-type ZnSe are particularly difficult because of the deep valence band of ZnSe. Because the valence band is deep, relative to the vacuum level, the offset between the Fermi level of the metal and the Fermi level of p-type ZnSe is very large. The figure below illustrates the large barrier on p-type ZnSe. This offset lends itself to making Schottky barriers and makes the formation of Ohmic contacts very difficult. This difficulty exists with all metals because the metal Fermi level is always much higher than the ZnSe valence band.

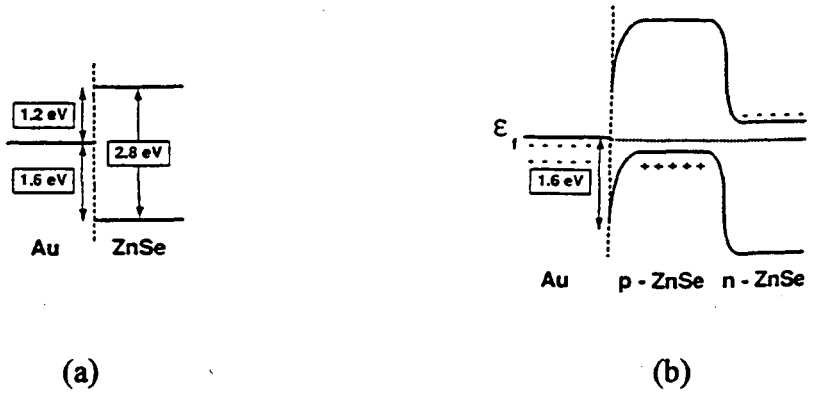

Figure 3.21: Band diagrams for (a) gold/ZnSe (b) gold/*p*-ZnSe/*n*-ZnSe heterojunction at zero bias. Energy offsets are estimates obtained from literature. (Lansari, et al. 1992)

Most of the work performed on ZnSe systems falls into two categories: studies of the interface reaction with monolayer coverages using photoemission spectroscopy, or brief reports of barrier heights used in studies of electrical properties of ZnSe. No studies have been done on the thermal stability of contacts.

3.3.1 Metal contact behavior

Table 3.1 lists known Schottky barrier heights on ZnSe. Most work has been done on n-type ZnSe because until recently, p-type was not available. A large amount of interest in contacts has been generated because of the new found ability to dope p-type using N radicals in MBE (DePuydt, et al. 1989). Au and In have been the most commonly used contacts for n-type ZnSe. Indium has been in use since 1961 and provides an Ohmic contact (Kaufman and Dowbor 1974; Livingstone, et al. 1973; Wang and Holloway 1992), however annealing is required. It is stable and Ohmic after anneals up to 350°C, but above 350°C, the contact resistance increases and it becomes rectifying (Dreilus, et al. 1990). The contact resistance has been measured to be 0.05 Ωcm^2 at a doping level of $2x10^{18}$ cm^{-3} (Wang and Holloway 1992). Au contacts have been used as Schottky barriers. Photoemission spectroscopy has shown that deposition of a few monolayers of Au does not disrupt the surface and that there is an abrupt interface (Anderson, et al. 1989). Mathematical modeling has shown that on p-type ZnSe Au should have a barrier height of 0.6 eV (Suemune 1993). Au has also been used in more elaborate contact systems. Several groups have reported that a Au/oxide/p-ZnSe contact, with 50 to 100Å of oxide, exhibits Ohmic behavior (Akimoto, et al. 1991). It has been speculated that the

Metal	ϕ_{SB} n-type (eV)	ϕ_{SB} p-type (eV)	Metal	ϕ_{SB} n-type (eV)	ϕ_{SB} p-type (eV)
Al	0.58(Vos, et al. 1989)		Fe	1.09 (calc) (Continenza, et al. 1990)	
Ag	1.06(Vos, et al. 1989)		Hg	1.4-1.5(Marshall, et al. 1989)	
Au	1.45(Vos, et al. 1989) 1.41 (Anderson, et al. 1989) 1.35-1.4(Marshall, et al. 1989) 1.5 (Akimoto, et al. 1991)		HgSe		Ohmic (Hiei, et al. 1993) 0.6-1.0 (calc) (Lansari, et al. 1992)
Ce	0.50(Vos, et al. 1989)		In	Ohmic(Dreilus, et al. 1990)	
Co	1.0(Vos, et al. 1989) 0.98(Anderson, et al. 1989)		Pd	1.48(Vos, et al. 1989)	
Cu	1 .1(Vos, et al. 1989) 1.1 (bulk) (Mead 1965)		Pt	1.4 (bulk) (Mead 1965)	
			Ti	0.85(Vos, et al. 1989) 0.7 (bulk) (Mead 1965)	

Table 3.1: Schottky barrier heights for metals on ZnSe

metal/oxide/semiconductor sequence allows a voltage drop across the oxide which raises the valence band of the ZnSe above the Fermi energy of the metal as shown in figure 3.22 (Thompson and Allen 1990). Akimoto (Akimoto, et al. 1991) proposed that the oxidized layer dopes the ZnSe and forms a heavily doped p-type layer at the surface. Considering the difficulties encountered in attempting to dope ZnSe p-type, this explanation seems implausible.

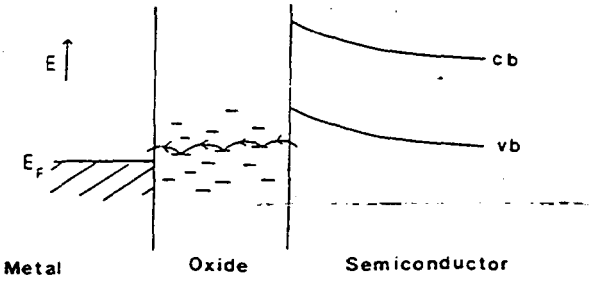

Figure 3.22: Schematic diagram of creation of holes in the valence band of ZnSe by electrons hopping between defects in an oxide layer. (Thompson and Allen 1990)

Ag has also been found to have a nondisruptive behavior when evaporated on ZnSe (Vos, et al. 1989). This means that the deposition of Ag does not alter the bonding of the ZnSe as measured by photoemission. It grows as three-dimensional islands. Photoemission has shown that the barrier height does not change if the Ag is ionized and accelerated toward the surface at up to 300-400 eV (Vos, et al. 1990). The long range order of the ZnSe surface degrades much more quickly for the ionized deposition, therefore the constancy of the Schottky barrier height indicates that the properties of the metal overlayer are more important than the interface morphology.

Observations of Al, Co, Cu, and Pd with photoemission show that these elements are disruptive to the surface when evaporated, even when the substrates were held at room temperature (Vos, et al. 1989). Co, Cu, and Pd grow in a layer by layer mode, while Al exhibits island growth. All four materials show evidence of Zn atoms dissolving into the growing overlayer, but no new phases are observed. Figure 3.23 shows the photoemission spectra for these four metals as a function of deposition thickness.

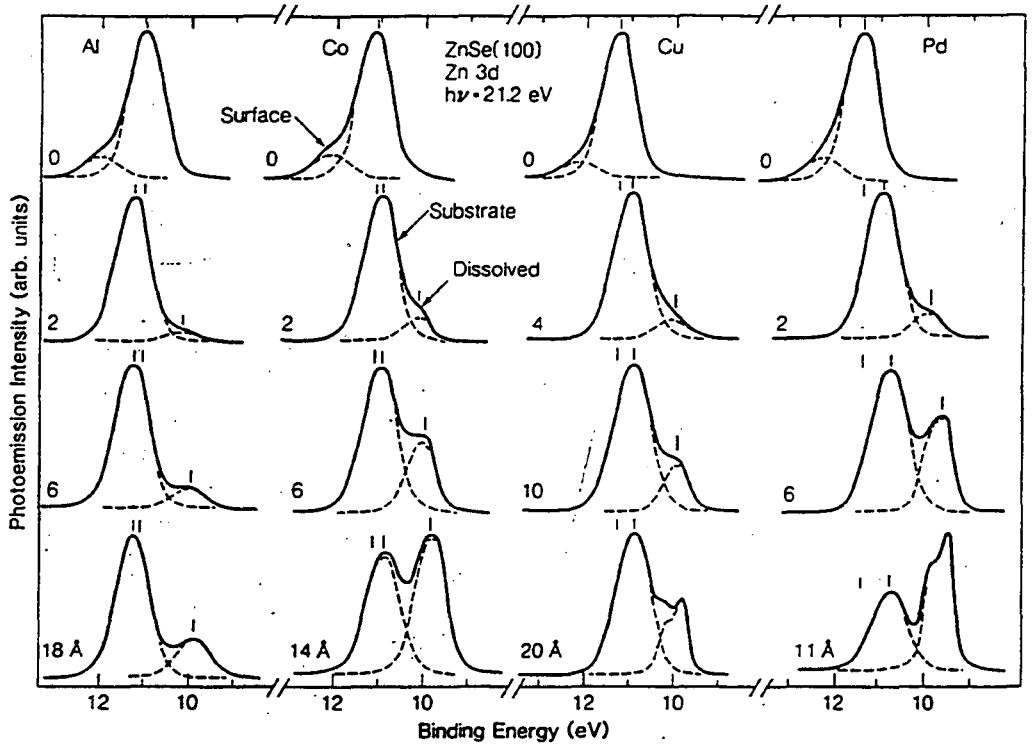

Figure 3.23: Zn 3*d* emission as a function of deposition for Al, Co, Cu, and Pd. Surface disruption is reflected by the appearance of a low-binding-energy component which is related to Zn atoms dissolved in the surface and near-surface region of the metal overlayer.

The growing peak on the right side of the substrate peak is attributed to Zn dissolved in the overlayer. Further study of Co showed that there is segregation of Se to the surface of the Co layer (Anderson, et al. 1989). Anderson, et al., found that by layering Au and Co and varying the thicknesses of the layers they could alter the measured barrier height. They determined that they could slightly lower both the Au and Co Schottky barrier heights and observed that with Au as the bottom layer, Co still diffused through to interact with the ZnSe. With Co as the bottom layer, Zn was extracted from the Co layer into the Au layer.

Ti and Ce were also studied using photoemission and were found to react with ZnSe. The photoemission spectra showed a peak indicating Zn dissolved in the overlayer, and a peak attributed to a reaction of Zn with the metal (Vos, et al. 1989). All of these photoemission measurements and the barrier heights determined were done with a maximum coverage of 15Å.

Some more complex, multilayered contacts have also been investigated. A Au/Pt/Ti contact to n-type ZnSe, with an electron concentration of $2x10^{19}$ cm^{-3}, was found to have a contact resistance of $3.4x10^{-4}\Omega cm^2$ (Miyajima, et al. 1992). This contact was stable up to 300°C and had good adhesion due to the reactivity of the Ti. Miyajima, et al., put Au on the contact to allow wirebonding to the device and used Pt as a diffusion barrier. Ohmic contacts to p-type ZnSe have been developed using graded Zn(Se,Te) or ZnSe/ZnTe multiquantum wells (Fan, et al. 1993; Hiei, et al. 1993). Au is a good Ohmic contact to p-type ZnTe and by gradually changing the semiconductor composition to p-type ZnTe or using a multiquantum well structure it is possible to develop an Ohmic contact. This structure must be grown in situ after MBE growth of the desired p-type ZnSe layer.

Several studies have shown that annealing above approximately 300°C causes a degradation of the contact (Dreilus, et al. 1990; Heuken, et al. 1992; Miyajima, et al. 1992; Wang and Holloway 1992). Photoluminescence has shown evidence of the formation of point defects when ZnSe is annealed and it has been postulated that the deep defects formed are Zn vacancies (Heuken, et al. 1992; Kaufman and Dowbor 1974). It is

possible that capping the surface during annealing may decrease the formation of these defects.

3.3.2 Surface preparation methods

Many different methods for the preparation of ZnSe surfaces have been used. Few of these have been carefully characterized to determine the quality of the surface after the etch or cleaning. In addition to those mentioned here, the list of ZnSe etchants from Landolt and Börnstein is given in appendix I. Most etchants listed only clean the surface, they do not actually etch the ZnSe. An actual etchant for ZnSe is a mixture of 1g. $K_2Cr_2O_7$: 10 ml. H_2SO_4: 20 ml. H_20 (Dreilus, et al. 1990; Miyajima, et al. 1992). This etches both ZnSe and ZnTe. ZnSe is etched at a rate of approximately 50-60 Å per minute. Wet etches for cleaning include $HF:H_2O$ (1:30) (Marshall, et al. 1989) and $HCl:H_2O$ (1:1) (Dreilus, et al. 1990; Miyajima, et al. 1992) and are used to remove any oxide or surface contaminants. A solution of Br in methanol has also been used (Al-Bassam 1990; Livingstone, et al. 1973). The Br in methanol etch has been reported to leave Se and ZnO on the surface (Livingstone, et al. 1973). The photoemission studies discussed earlier were performed on metals deposited on a dry etched surface. This surface was sputtered with 500 eV Ar^+ ions and then annealed at 400°C for 20 minutes. The annealing was intended to remove surface damage caused by the sputtering.

4. Experimental

4.1 Sample preparation

ZnSe samples were grown by OMVPE by Jim Walker and Edith Bourret at Lawrence Berkeley Lab. Di-ethyl zinc (DEZ) and di-isopropyl selenide (DISE) were used as precursors. All samples were grown at a Se/Zn ratio of 4.0, a growth temperature of 464°C, and a chamber pressure of 300 Torr. Growth times varied from 41 minutes to 60 minutes and thicknesses ranged from 0.47 μm to 0.9 μm . A more detailed specification of the growth parameters is given in appendix II.

4.1.1 Surface preparation

Several cleaning methods were tried, based on those reported in literature, to obtain reliable contacts. Degreasing was done with a sequence of solvents. The samples were first boiled in trichloroethane for three minutes, then boiled in acetone for three minutes, followed by a final three minute boil in methanol. The samples were then rinsed in room temperature methanol and blown dry with N_2. Table 4.1 lists the variety of wet etches that were tried along with the experimental parameters used. Only the potassium dichromate etch actually etches the ZnSe, the remainder are for removing oxides or other contaminants.

Etch	Composition	Time (seconds)	Quench
HF vapor	full strength	20	distilled H_2O
HF dip	full strength	5-25	distilled H_2O
HF dip	full strength	10	none
NH_4OH:methanol	1:3	10	methanol
NaOH	6M, 100°C	60	distilled H_2O
$K_2Cr_2O_7$:H_2SO_4:H_2O	5 g:50 ml:100 ml	30	distilled H_2O

Table 4.1: Wet etches used on ZnSe samples

One dry etch was used. The samples were backsputtered in a model 2400 Perkin-Elmer sputtering system for 6 minutes. Ar ions were used with a forward power of 100 W. The tune was set to 1238, the load at 860, and the target bias was 650 V. The tune and load are used to match the impedance of the substrate table system with that of the coaxial cable bringing the RF power from the generator. The tune controls the parallel capacity in the target circuit, while the load controls the coupling between the primary and secondary circuits of the network. Profilometer measurements showed that 1900Å were removed in a 12 minute backsputter, indicating that about 1000Å should be removed in the 6 minute backsputter.

4.1.2 Deposition

Two systems were used for depositing approximately 800Å thick Pt and Pd films. Sputtered films were deposited using the model 2400 Perkin-Elmer sputtering system. Base pressures were usually around $3x10^{-6}$ Torr. Parameters used for depositing Pt and Pd are shown in table 4.2.

	Pt	Pd
load	891	914
tune	815	938
forward power (W)	300	300
target bias (V)	1500	1500
reflected power (W)	2.5	3.0
deposition rate (Å/sec)	9.3	13.0

Table 4.2: Sputtering parameters

Films were also deposited using the Veeco electron beam evaporator. Base pressures in the evaporator were usually $5x10^{-7}$ Torr. Pt evaporation was found to be difficult because of the high temperature required. The Pt source would not give a uniform coating of Pt unless the source was heated uniformly and the surface was cleaned of contaminants by rastering the electron beam across it. Both methods gave polycrystalline films with similar x-ray peak widths. The relative purity of the films was not investigated.

4.1.3 Annealing

Samples were annealed in a Type 54241 Lindberg Hevi-Duty tube furnace in flowing nitrogen. The furnace was allowed to reach the desired annealing temperature and then the sample, in a quartz holder, was inserted. The temperature would initially drop and then restabilize at the desired temperature in a few minutes. At the end of the annealing period, the samples were placed at the end of the annealing tube, which was at room temperature. They were cooled at room temperature in flowing nitrogen for approximately ten minutes.

4.2 Characterization - experimental setup

4.2.1 RBS

RBS was performed with the system at LBL. Spectrometry measurements were performed with a 1.95 MeV $^4He^+$ beam with a scattering angle of 165°, as defined in chapter 2. The beam spot was 1 mm in diameter on the sample. A Si surface barrier detector was used with an acceptance of approximately 2 msr and a resolution of approximately 20 keV. 4 μC of charge was collected at a current of 6-10 nA. A circular shield biased to -900V surrounded the sample to suppress any secondary electrons.

4.2.2 X-ray diffraction

X-ray diffraction was performed with a Siemens D500 diffractometer. Cu Kα x-rays of energy 8 keV were used. Both glancing angle and Bragg-Brentano geometries were used. Spectra were generally taken over a 2θ angular range of 28-85°. This range was chosen because it contains the majority of the peaks for Pt and Pd phases with Zn and Se that are listed in the powder diffraction file data base. A listing of all of these phases catalogued in the power diffraction file is in appendix III.

For glancing angle measurements a 3° incident angle was used. 1° and 0.3° slits were used in slots 1 and 2 at the exit of the x-ray source. This combination was found to be most sensitive to the presence of new compounds in these systems. For θ-2θ diffraction, slits of 1° and 1° were used in slots 1 and 2 on the x-ray source and 1° and 0.1° in slots 3 and 4 on the x-ray detector. The x-ray scans were performed with a 0.1° step size and 2 seconds of data collection per step. Each scan took approximately 20 minutes to perform. This step size was small enough to resolve all peaks in the spectra.

4.2.3 X-ray photoelectron spectroscopy

XPS was performed with a Phi 5300 system. A 1.1 mm diameter circular aperture and the Kα-line of a Mg x-ray source were used. A pass energy of 179 eV was used which gave a analyzer resolution of 4.5 eV. Data was acquired for 3 minutes and the detector was at an angle of 15°. Sputtering was done with the Ar ion gun with a sputter rate of approximately 100Å per minute over a 2 mm diameter area.

5. Results and Discussion

5.1 Surface Characteristics

The surface characteristics of ZnSe were investigated because of the difficulty in obtaining consistent reactions of Pt on ZnSe. Prior to deposition, samples were initially treated with the degreasing steps and the HF vapor etch described in section 4.1.1. These Pt coated samples would then react unexpectedly as demonstrated in figure 5.1.

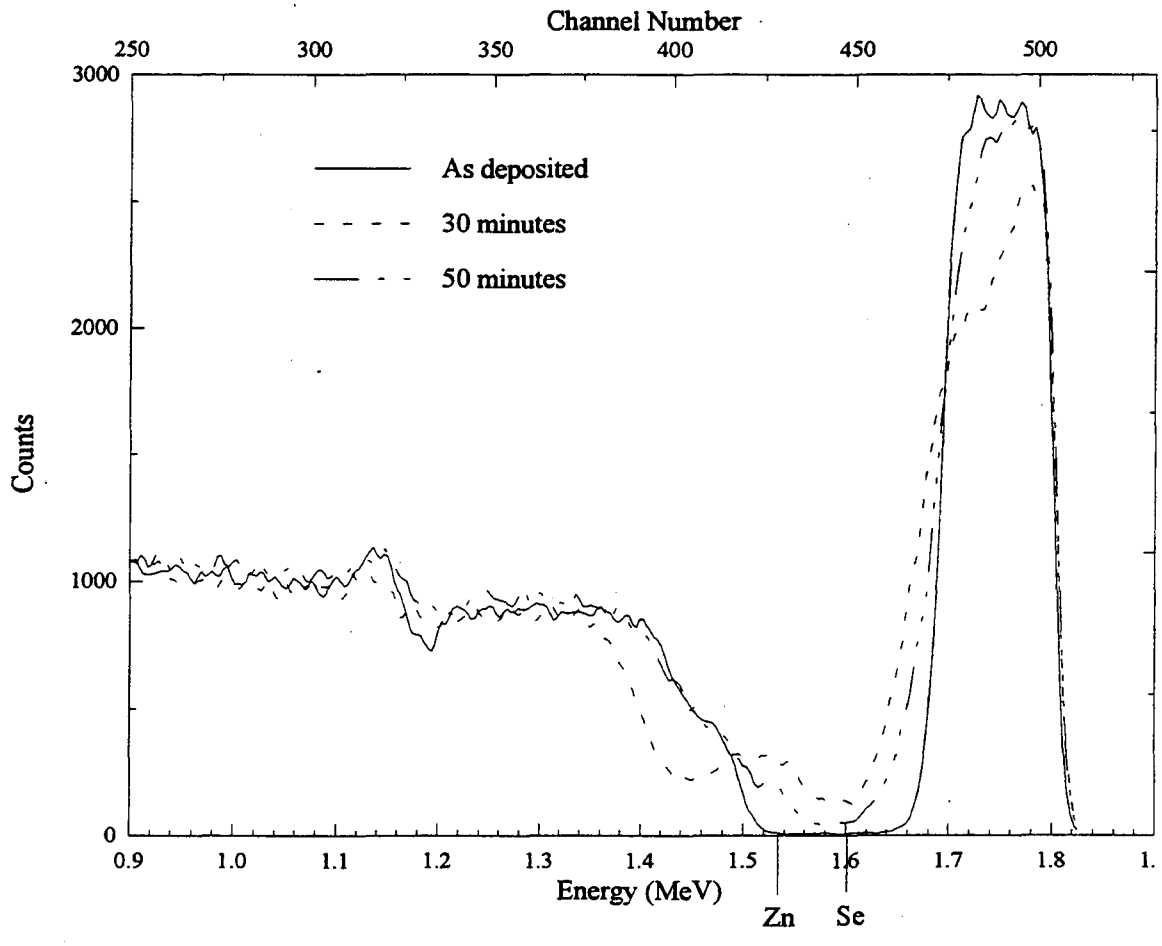

Figure 5.1: RBS spectra of Pt/ZnSe samples cleaned only with a wet etch annealed at 575°C for various times.

Note that the sample annealed for 50 minutes appears to have reacted less than the one annealed for 30 minutes. These two samples were from the same wafer and were etched and sputtered together. The dip and rise in the spectra at 1.15 MeV is due to the interface between the GaAs and ZnSe. This inconsistency in the solid-state reactions was typical of that seen in samples which were only wet etched. Pd samples which were treated in the same manner had consistent reaction behavior. Pd is known to react more strongly on Si and GaAs, as discussed in chapter 3, and is generally not hindered by contamination at the surface. For this reason, it was speculated that the inconsistency in the Pt reactions was due to contamination or an oxide at the surface. XPS was utilized to investigate the surface characteristics of the ZnSe.

XPS measurements were performed on a variety of ZnSe surfaces prepared in different manners. These measurements were intended to determine the amount of contaminants on the surface of the as-grown layers and the changes after various surface treatments.

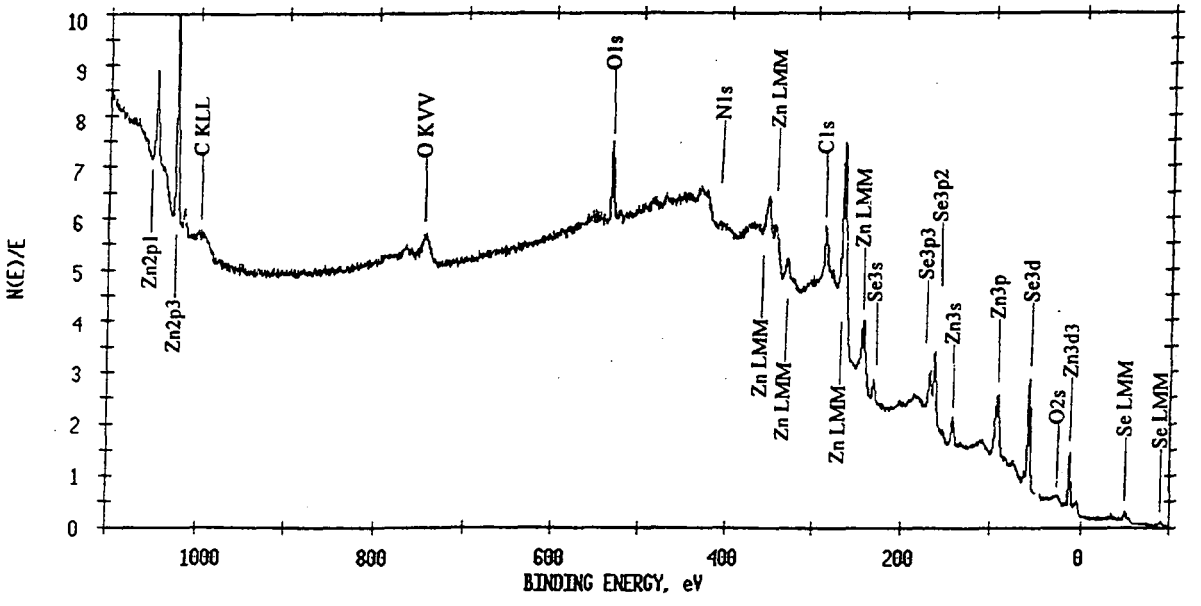

Figure 5.2: XPS spectrum of an as-grown ZnSe surface.

Figure 5.2 shows an XPS spectra for an as-grown ZnSe wafer. Wafer number 181 was not etched or cleaned and was grown three months prior to taking this spectrum. Note that there is an obvious presence of O and C on the surface. Both XPS and Auger peaks are visible. The XPS peaks are labeled with the orbital from which the electron came, while the Auger peaks are labeled with the transition type (KLL, LMM, etc.). No appreciable amount of other contaminants is observed. Figure 5.3 shows XPS spectra for samples from wafer 181 that were treated with two different etchants. One was etched for 25 seconds in 49% HF, the other was etched for 15 seconds in the $K_2Cr_2O_7$ etch described in chapter 4. The $K_2Cr_2O_7$ etch removed approximately 750Å of ZnSe. Both samples were rinsed in distilled water and blown dry with N_2. The spectra were taken after the samples had been in air for approximately two hours.

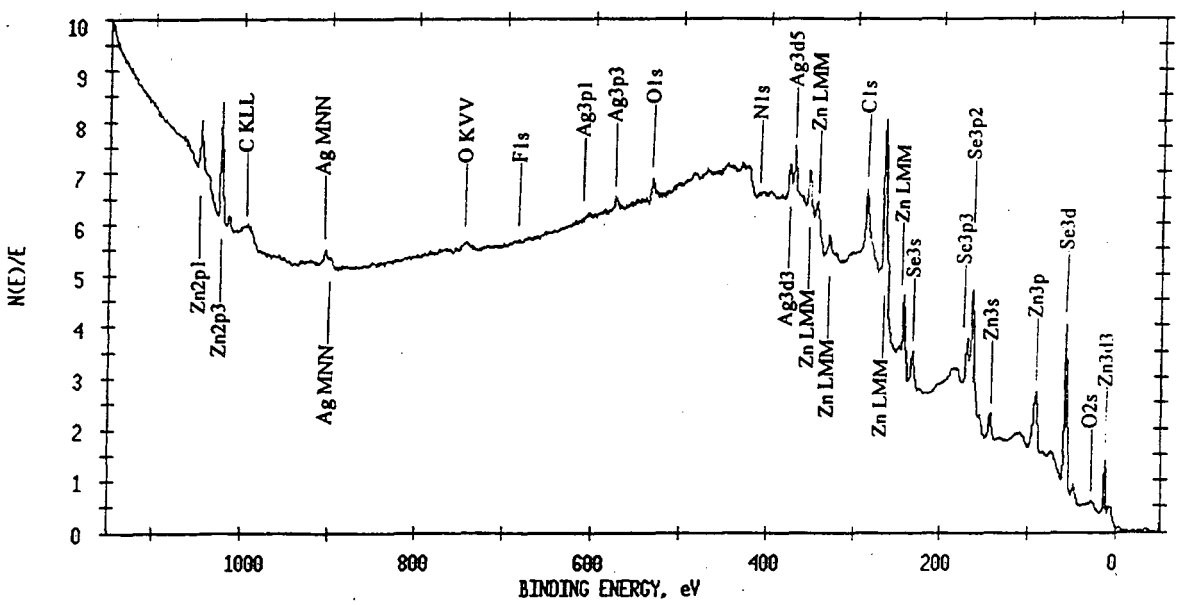

Figure 5.3a: XPS spectrum from a sample etched for 25 seconds in HF.

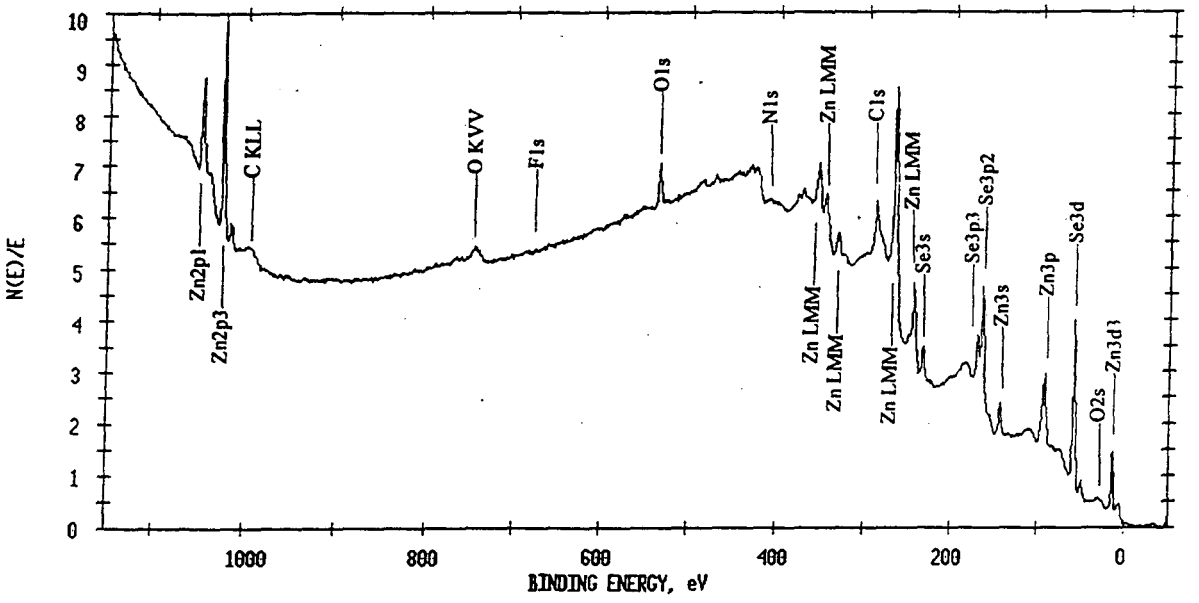

Figure 5.3b: XPS spectrum from a ZnSe sample etched for 15 seconds in $K_2Cr_2O_7$:H_2SO_4:H_20.

These spectra show that the C peak is approximately the same as that observed on the as-grown layer. Atomic concentration percentages for C, O, Se, and Zn on the various sample surfaces are shown in table 5.1. The O peak is diminished after both etching techniques, however the peak is smaller on the sample etched with the $K_2Cr_2O_7$ mixture. The surface oxide must be completely removed by the $K_2Cr_2O_7$ etch since it consumes approximately 750Å of the ZnSe. Therefore, the measured O peak on this sample is due to oxide regrowth in the two hour period between etching and measurement. The O peak is higher on the HF etched sample which indicates that in addition to oxide regrowth, less of the oxide was originally removed from the surface. In addition, the HF etch did not

	As grown	Sputter Etched	5 minute air exposure	$K_2Cr_2O_7$ etch	HF etch
C 1s	51.00	18.56	46.85	58.67	50.27
O 1s	17.99	2.12	6.67	7.31	13.50
Se 3d	24.09	52.04	36.44	31.58	29.41
Zn 2p3	6.92	27.28	10.05	2.44	6.82
Se:Zn	3.48	1.91	3.63	12.94	4.31

Table 5.1: Atomic concentration percentages for C, O, Se, and Zn on samples prepared with various surface treatments.

reduce the C peak substantially. Although the $K_2Cr_2O_7$ etch adequately removed the oxide, it also did not remove the C and introduced Ag contamination on the surface. This contamination is likely due to impure $K_2Cr_2O_7$. Neither of these wet etches provided an adequate method for reducing both O and C contamination.

An in situ Ar^+ ion sputter was performed on an as-grown ZnSe sample from wafer 181. The sample was sputtered for two minutes using the parameters given in section 4.2.3. This sputter should have removed approximately 200Å of ZnSe. Figure 5.4 shows the XPS spectra from the sample immediately after sputtering and then after a five minute exposure to air. The time of exposure may have been slightly greater due to time required to load and unload the sample.

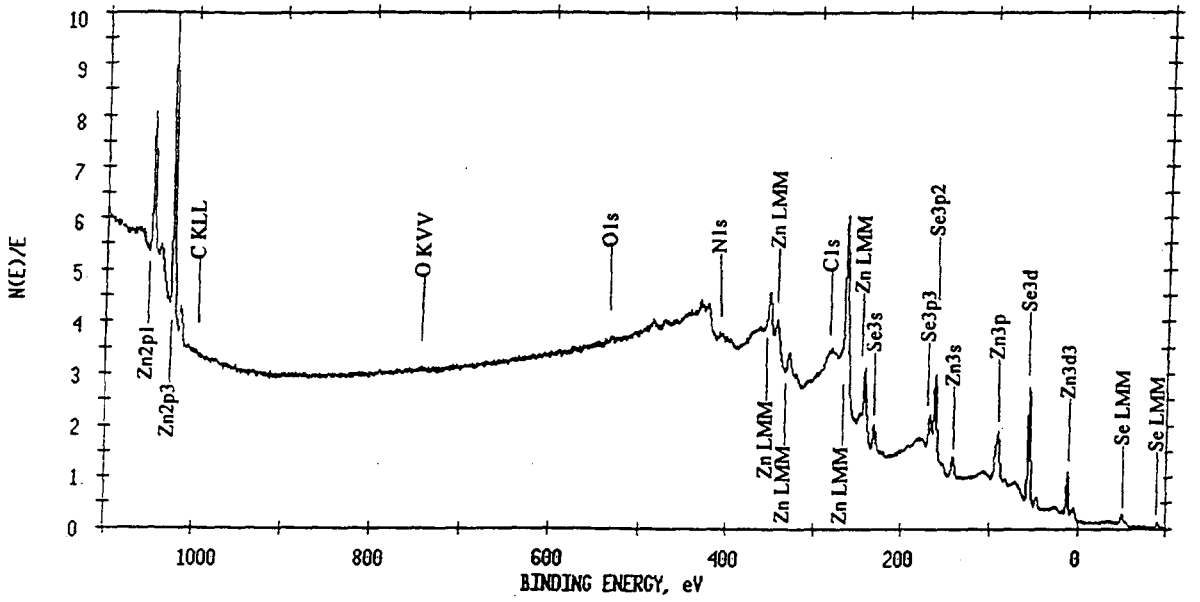

Figure 5.4a: XPS spectrum from Ar^+ sputtered ZnSe sample immediately after sputtering.

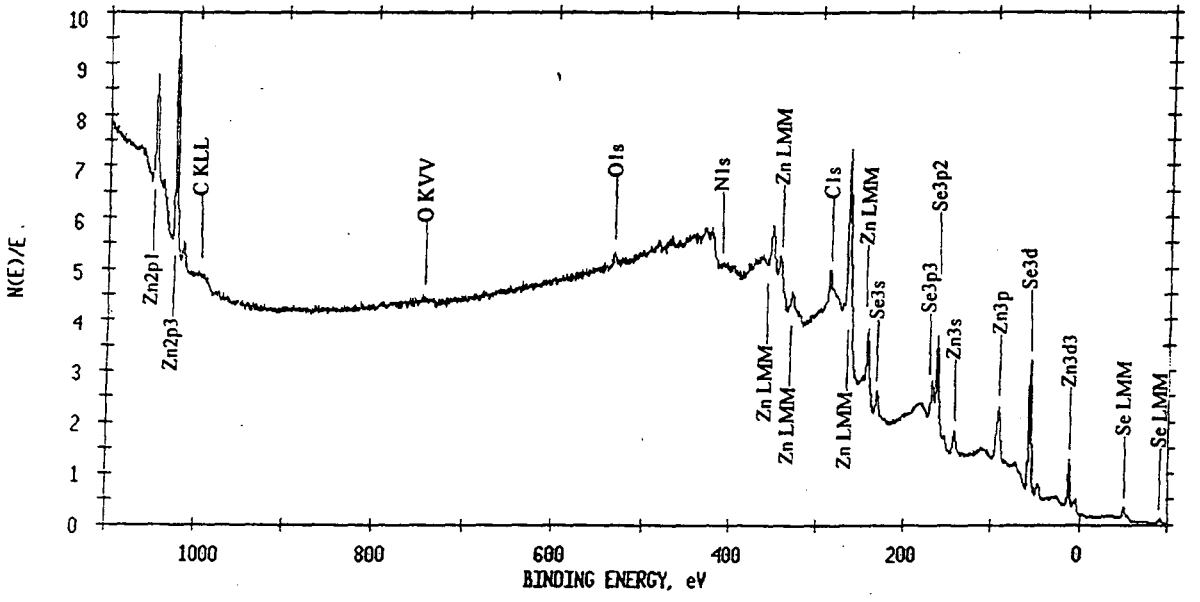

Figure 5.4b: XPS spectrum from Ar^+ sputtered ZnSe sample after sputtering followed by a five minute exposure to air.

Sputter etching significantly reduced the amount of O and C contamination on the surface. The O AES peak is not visible, and the O XPS peak is almost unidentifiable. The C peak is significantly reduced but not eliminated. After a five minute exposure to air there is a slight increase in the amount of O on the surface and an increase in the amount of C. The O AES peak is still not visible. Ar^+ sputtering appears to be the preferred method for removing contaminants from the surface. A detrimental aspect of sputtering is that it can cause damage to the surface. The amount of damage after sputtering can be investigatedusing channeling RBS. When the incident ion is aligned with a channel in a perfect crystal very few ions will be backscattered. A comparison of the number of ions backscattered from a channel gives an indication of the degree of perfection of the crystal. Figure 5.5 shows 1.8 MeV RBS channeling results along the <111> direction from an

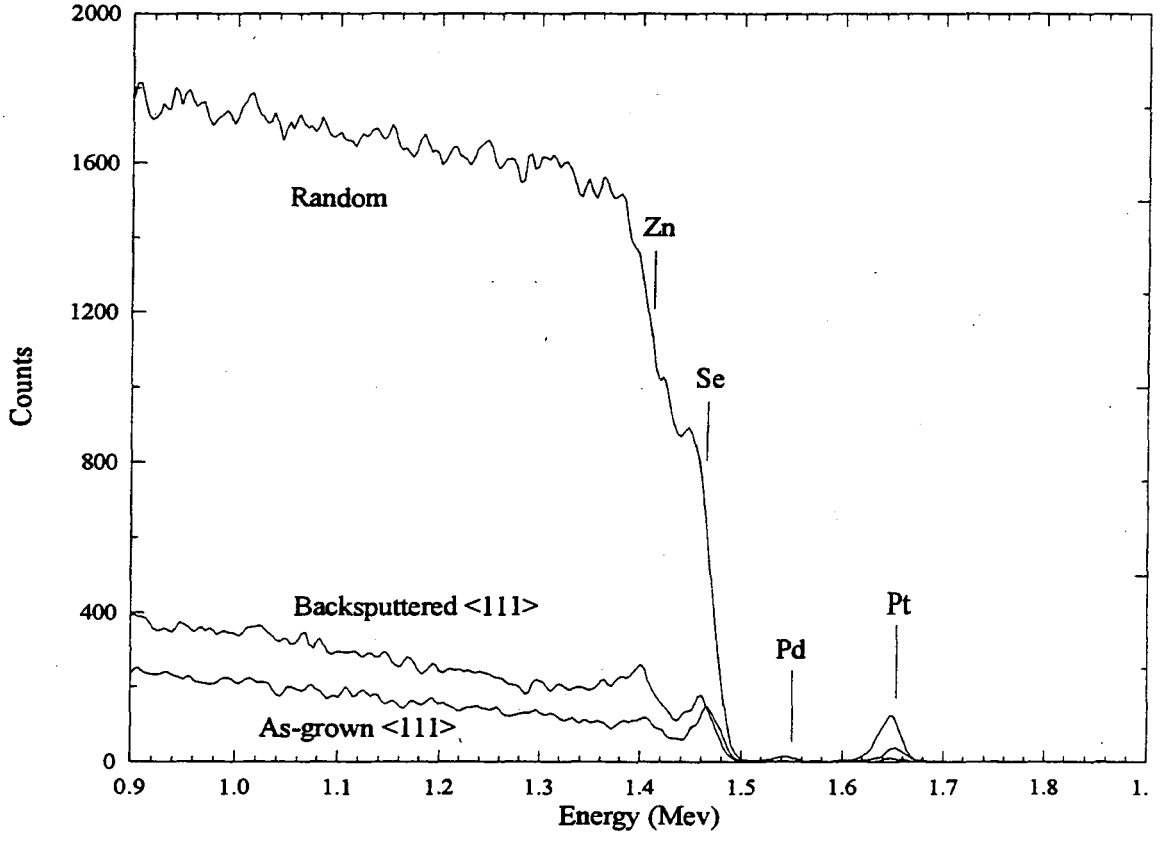

Figure 5.5: 1.8 MeV RBS channeling experiments on as-grown and Ar^+ sputtered ZnSe.

as-grown and a sample backsputtered in the Perkin-Elmer sputtering system following the parameters given in section 4.1.1. The signal for the backsputtered sample increases only slightly, indicating very little damage at the surface. The small peak at 1.65 MeV is due to Pt contamination and the peak at 1.55 MeV is due to Pd. This contamination came from backsputtering off the sample holder in the chamber. This can be reduced by careful mounting of the samples and the use of clean sample holders. The use of Ar^+ sputtering provides a good method for removing contamination from the sample surface without creating a great deal of damage.

The cleaning method also affects the ratio of Zn and Se on the surface of the sample. Table 5.1 gives the Se to Zn ratio for each of the samples. The O and C concentrations are most reduced after sputtering. This treatment, however, also changes the ratio of Se and Zn on the surface. An HF etch increases the Se to Zn ratio. It was found that Pt reacted more consistently after an Ar^+ sputter treatment, but Pd would not react after this same treatment. The Pd reacts better after the surface is treated only with an HF etch. This discrepancy may be due to the difference in surface coverage of Se and Zn. Pd may react more strongly on a surface with a higher percentage of Se while Pt may prefer to react with a Zn terminated surface

The final cleaning method used to obtain consistent results for Pt reactions included the Ar^+ sputter as one of the steps, but it is not clear whether this single step improved the consistency. This will be discussed in more detail in section 5.3.

5.2 Pd

Pd begins to react with ZnSe during annealing at 200°C. A series of isochronal anneals was used to determine the onset of the reaction. Figure 5.6 shows the spectra from a series of 10 minutes anneals.

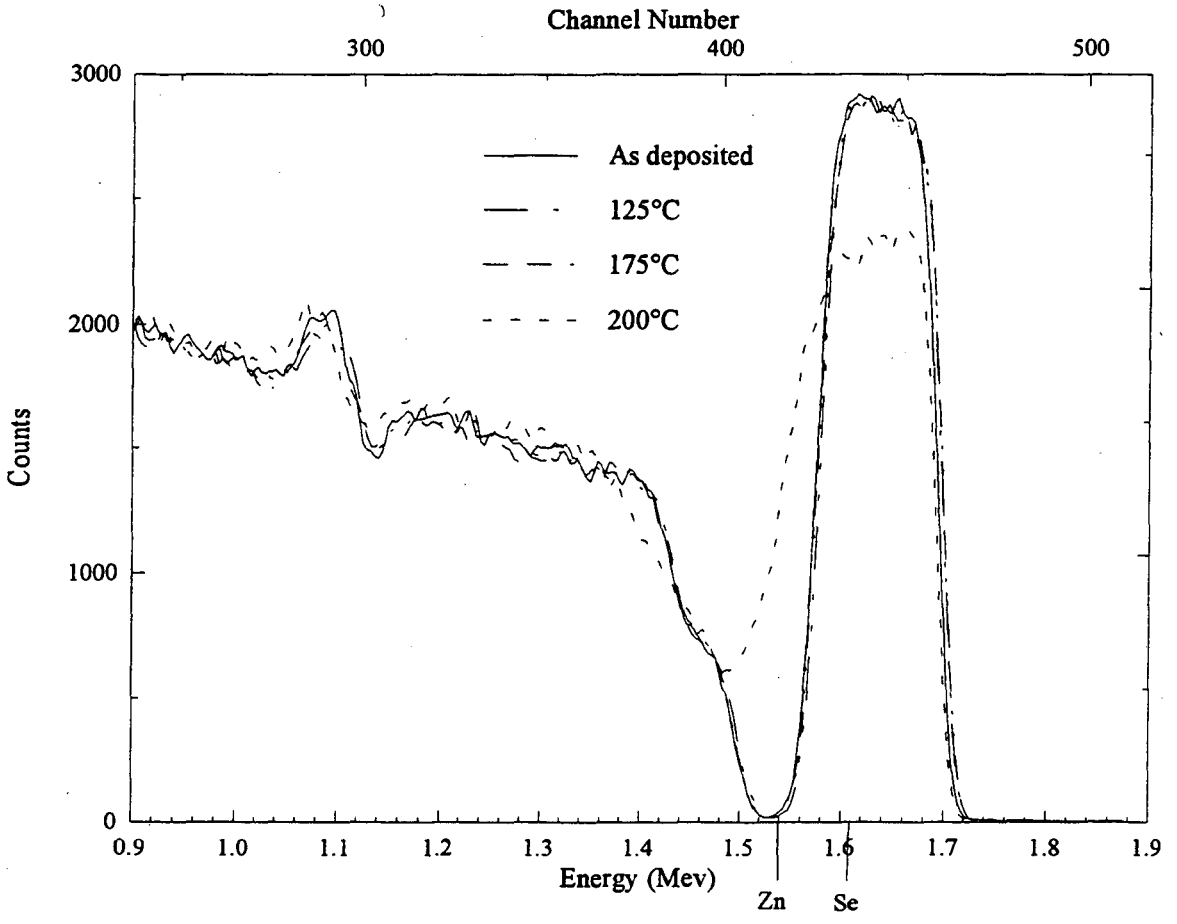

Figure 5.6: RBS spectra of Pd/ZnSe annealed for 10 minutes at various temperatures.

There is no observable diffusion at the metal/ZnSe interface in the samples annealed at 125° and 175° C, but annealing at 200°C results in a distinct change in the RBS spectrum indicating solid-state reaction between Pd and ZnSe. This low temperature for reaction is analogous to the low temperatures required for reaction of Pd on Si and GaAs. The reaction progresses quickly at 200°C and distinct steps are not visible in the RBS spectra. The lack of distinct steps in the Pd signal in the RBS spectra is similar to the case of Pd reactions on GaAs (Olowolafe, et al. 1979). This suggests the formation of a ternary phase, as in the Pd/GaAs system, the presence of mixed binary phases in a single layer

without vertical separation, or non-uniformity in the plane perpendicular to the beam. Figure 5.7 shows typical RBS spectra for a series of isothermal anneals at 200°C.

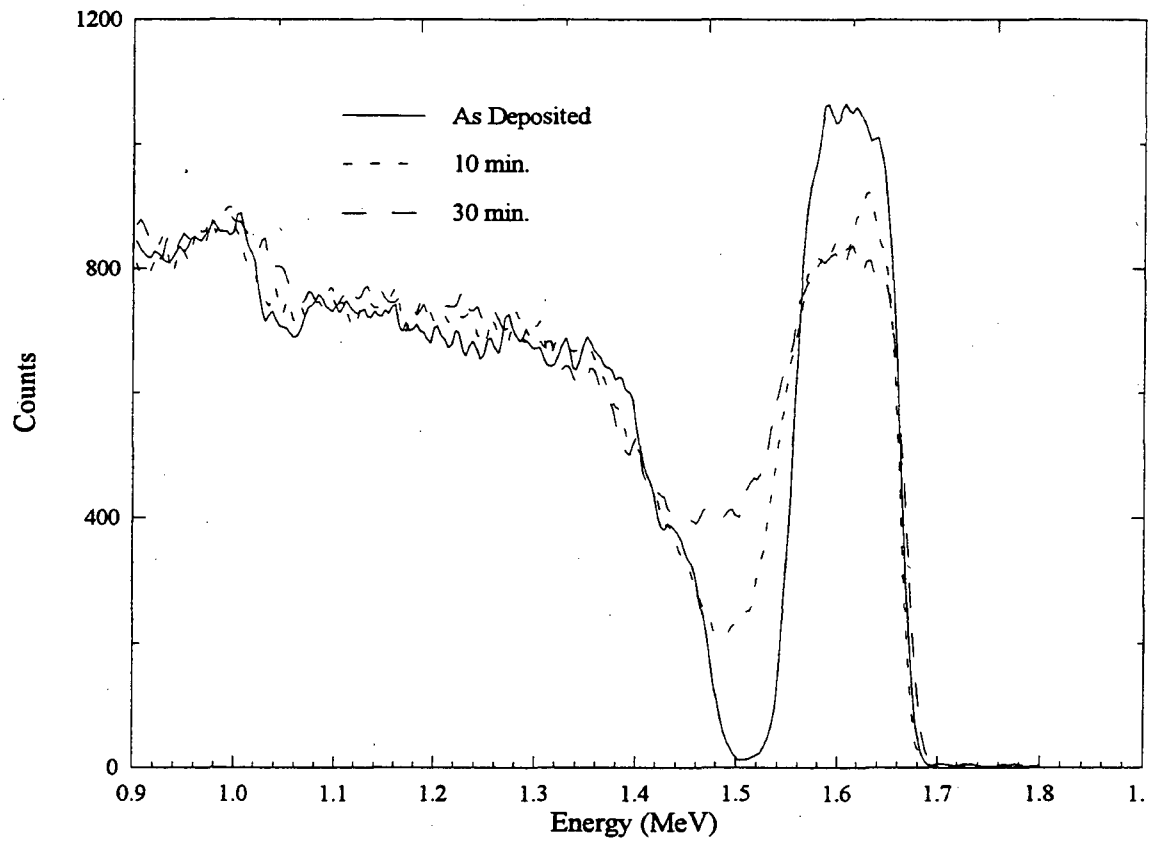

Figure 5.7: RBS spectra of Pd/ZnSe annealed for various times at 200°C.

From this figure it is clear that there is interdiffusion between the Pd and ZnSe, but there is no accumulation of Zn or Se on the surface. If a layer of Zn or Se had formed on the surface, the onset of the Pd energy would be decreased by the energy lost as the ions traveled through the Zn or Se layer. Since the onset energy does not change, there must not be any segregation to the surface. The Pd signal from the 10 minute annealed sample in figure 5.7 shows a small peak on the surface suggesting that a small layer of unreacted Pd exists on the surface. After 30 minutes of annealing the uniform decrease in the peak

height of the Pd signal indicates that there is no longer any unreacted Pd, while the movement of the ZnSe edge to lower energies indicates that some of the ZnSe has been consumed in the reaction. The lack of a layered structure makes it difficult to determine whether a phase is forming and to estimate the composition from the RBS results alone. If we assume that a laterally uniform ternary phase has been formed, as in the Pd/GaAs system, and that all of the Pd has reacted, the composition ratio between reacted Pd and consumed ZnSe can be estimated. The amount of ZnSe that has reacted with the Pd layer can be calculated from the change in the spectrum. Averaging over a number of samples annealed for 30 minutes each, calculations show that the composition ratio between Pd and ZnSe should be close to 6. This predicts a ternary phase of the composition Pd_6ZnSe. An estimate of the composition can also be made by using RUMP, an RBS simulation program (Doolittle 1985). The composition of the ternary Pd_xZnSe phase can be simulated by varying the Pd and ZnSe concentrations until the simulated Pd peak height matches the measured peak height. The simulation estimates the composition as Pd_5ZnSe. The x-ray results in figure 5.8 help clarify the amount of Pd reacted in the film.

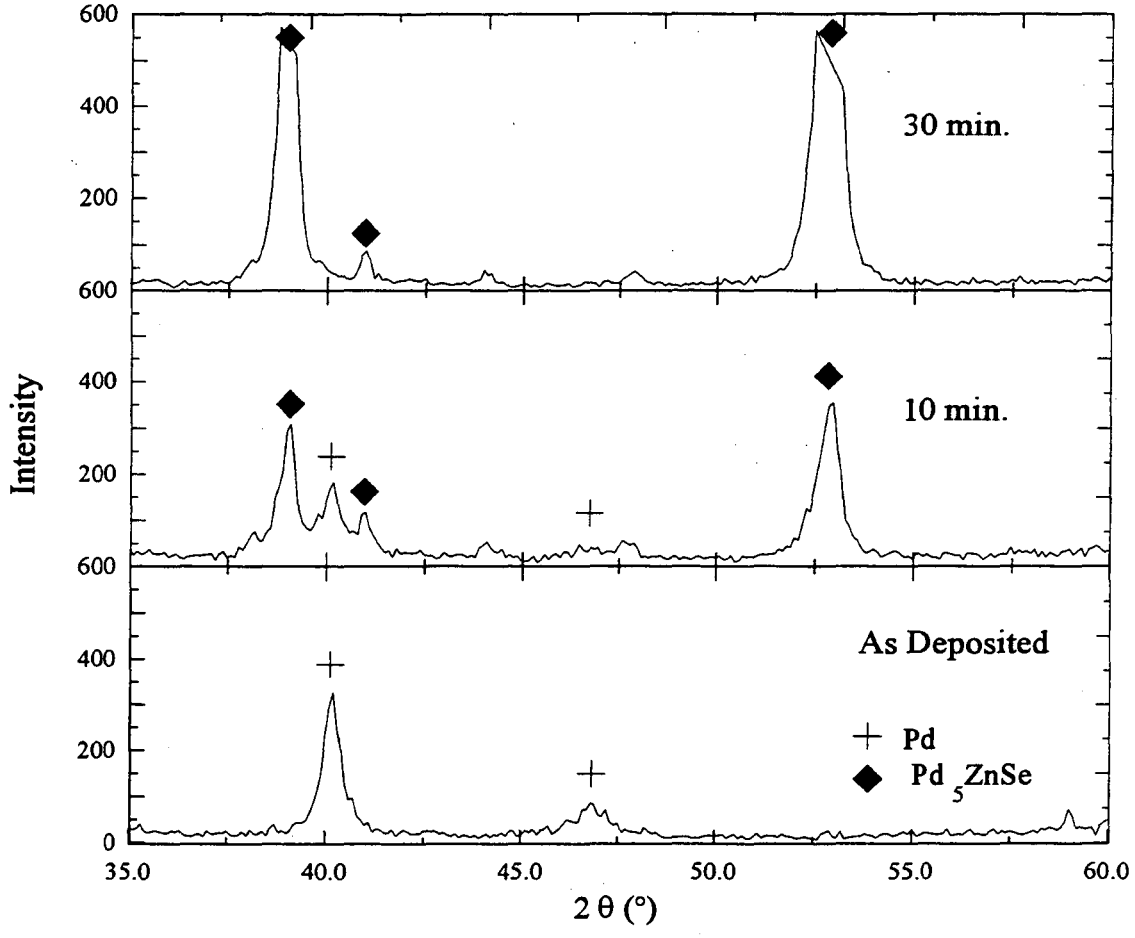

Figure 5.8: X-ray spectra of Pd/ZnSe for as-deposited and samples annealed for various times at 200°C

In the x-ray spectrum from the 30 minute annealed sample in figure 5.8 the Pd peaks have disappeared indicating that all of the Pd has reacted. In the x-ray spectra, the as deposited sample shows two polycrystalline Pd peaks in this angle range at $2\theta = 40.1°$ and 46.7°. Note that these angles are expressed as 2θ, not θ. After annealing for ten minutes at 200°C the Pd peak intensity decreases and two new peaks appear at $2\theta = 39.0°$ and 52.9°. This is consistent with the RBS results which show a small amount of unreacted Pd remains after a 10 minute anneal, but that no unreacted Pd remains after the 30 minute anneal. After a longer anneal the Pd peaks almost completely disappear and the new

peaks become very intense. This indicates that this phase is stable at this temperature and that during the longer anneal either more of the phase is formed or it becomes more epitaxial.

The identity of the new phase can be precisely identified by doing an x-ray scan over a wide range of angles. A wider range x-ray scan provides more peaks with which to identify the new phase. The relative peak intensities of the new phase are better represented in figure 5.9. These x-ray scans were done in the Bragg-Brentano geometry.

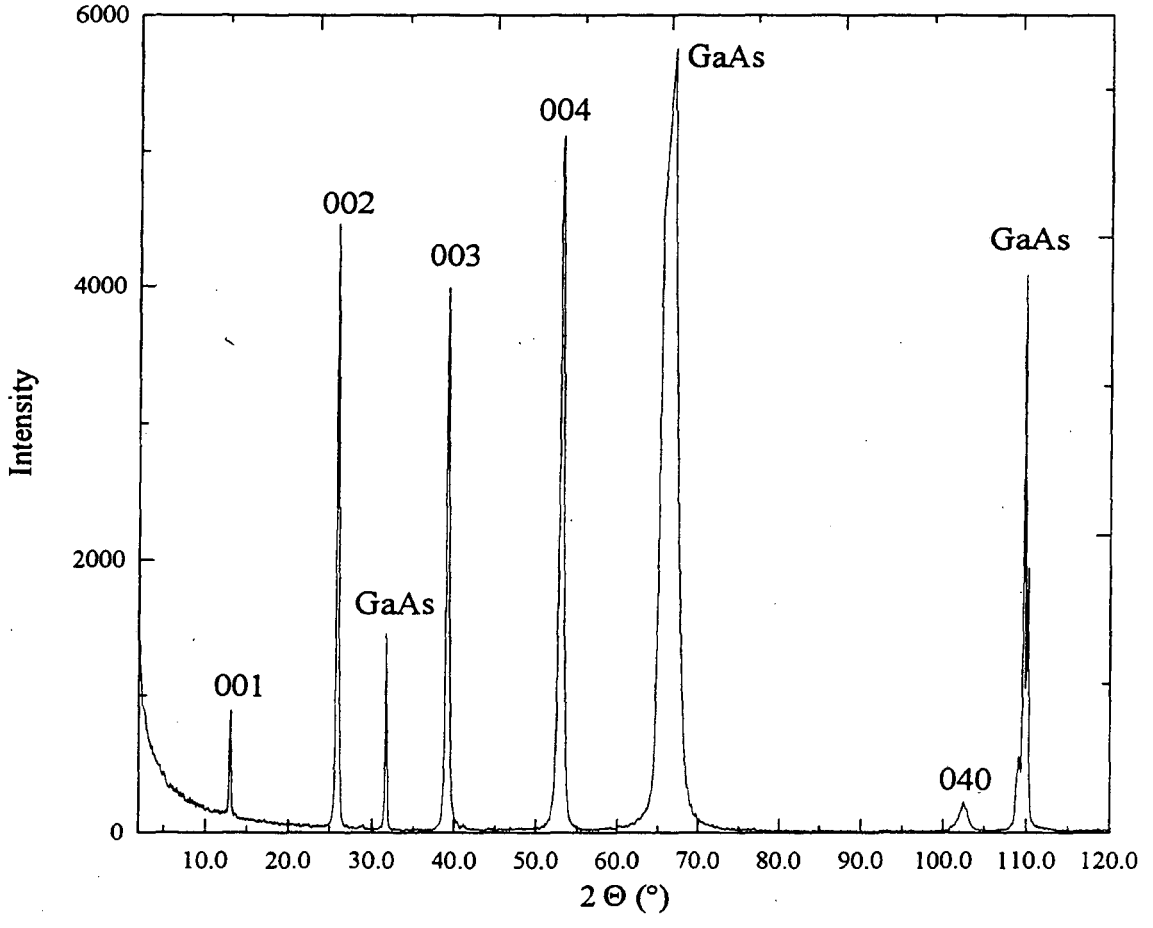

Figure 5.9: Wide range Θ-2Θ scan of Pd/ZnSe sample annealed at 200°C for 4 hours and 40 minutes. Labels give (hkl) values for Pd_5ZnSe.

The new peaks were not observed in scans using the glancing angle geometry. This indicates that the new phase has a definite orientational relationship with respect to the substrate. Figure 5.9 shows the x-ray spectra for a sample which was annealed for 4 hours and 40 minutes at 200°C. This is the same phase which appears during shorter anneals which indicates that this phase is very stable at this temperature. The high intensity of the diffraction peaks is only possible if the new phase formed has a preferred orientation with respect to the substrate. These peaks do not correspond to any Pd/Zn/Se phases in the powder diffraction data file. Calculations based on the crystal structure and Bragg's law showed that the strongest peaks were due to the (00l) reflections of the ternary Pd_5ZnSe phase. This is a tetragonal phase with a = 0.4005 nm and c = 0.7042 nm. The details of the crystal structure are given in appendix IV.

d (Å) measured	d (Å) calculated	(hkl)	Relative Intensity
6.896	6.914	(001)	16
3.450	3.457	(002)	89
2.304	2.305	(003)	79
1.727	1.729	(004)	100
0.988	0.988	(040)	4
0.947	0.949	(141)	11

Table 5.2: Comparison of measured and calculated lattice spacings for Pd_5ZnSe.

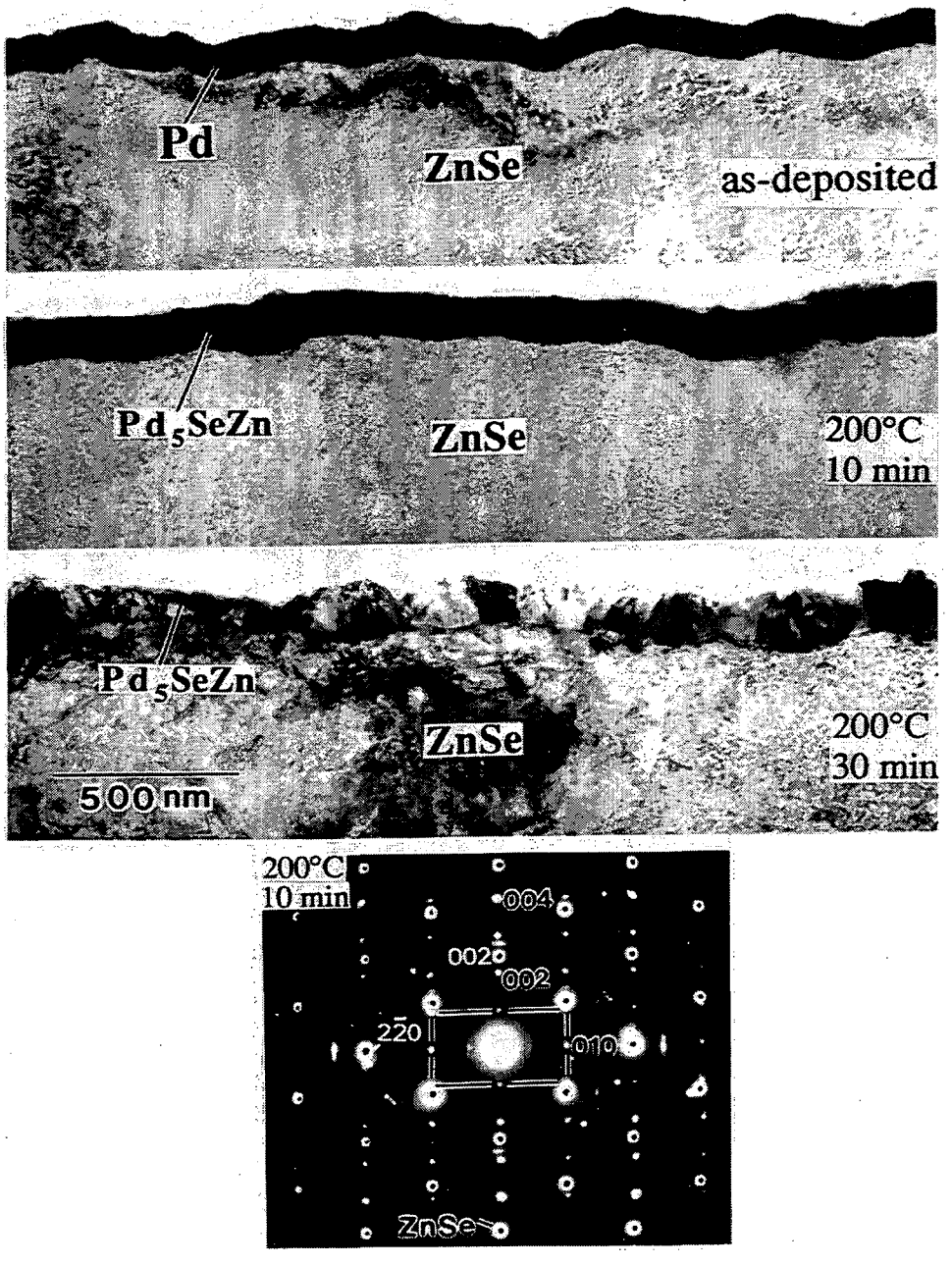

Figure 5.10: TEM micrographs showing the progression of phase formation in the Pd/ZnSe system. (a) morphology of as-deposited sample, (b) Pd_5ZnSe layer formed in sample annealed at 200°C for 10 minutes, (c) increase in thickness of Pd_5ZnSe layer after annealing for 30 minutes at 200°C, (d) selected area diffraction showing orientational relationship of Pd_5ZnSe with substrate, ZnSe[110]//Pd_5ZnSe[100].

A few smaller peaks, such as (040), also aligned with calculated peaks. Table 5.2 gives the measured and calculated d spacings for the peaks. Selected area diffraction (SAD) from TEM, as shown in figure 5.10d, verified that this was the phase. The formation of a ternary phase with an orientational relationship to the substrate is analogous to the formation of a ternary, oriented phase on GaAs at temperatures below 250°C (Sands, et al. 1985). Pd_2Si also forms with an epitaxial relationship (Bower, et al. 1973).

The lattice mismatch between the two materials in the orientation observed by SAD is only 0.05 percent. Most of the grains have the same orientational relationship, but not all are epitaxial with the substrate. Figure 5.10 shows the morphology of the as deposited layers and layers annealed at 200°C. The micrographs show that the new phase forms a complete layer. The interface in the annealed sample is smoother than that in the as deposited sample. As the reaction proceeds the grains become more epitaxial and the interface seems to become deeper. The reacted layer above the ZnSe becomes less uniform in thickness after annealing for thirty minutes.

The stability of this phase at higher temperatures was also investigated. Figure 5.11 shows RBS spectra for isochronal 30 minute anneals at temperatures above 200°C. Up to 500°C the spectra remain fairly similar, although the depth of the reaction increases slightly during the 300° and 400°C anneals as compared to the 200°C anneal. X-ray results verify that the ternary Pd_5ZnSe phase is still present up to 400°C. The intensities of the Pd_5ZnSe peaks increase with the 300° and 400°C anneals, also indicating that either the amount of the ternary phase or the degree of orientation has increased. This increase in degree of orientation is also seen in the Pd/Si system (Sigurd, et al. 1974). At 500°C

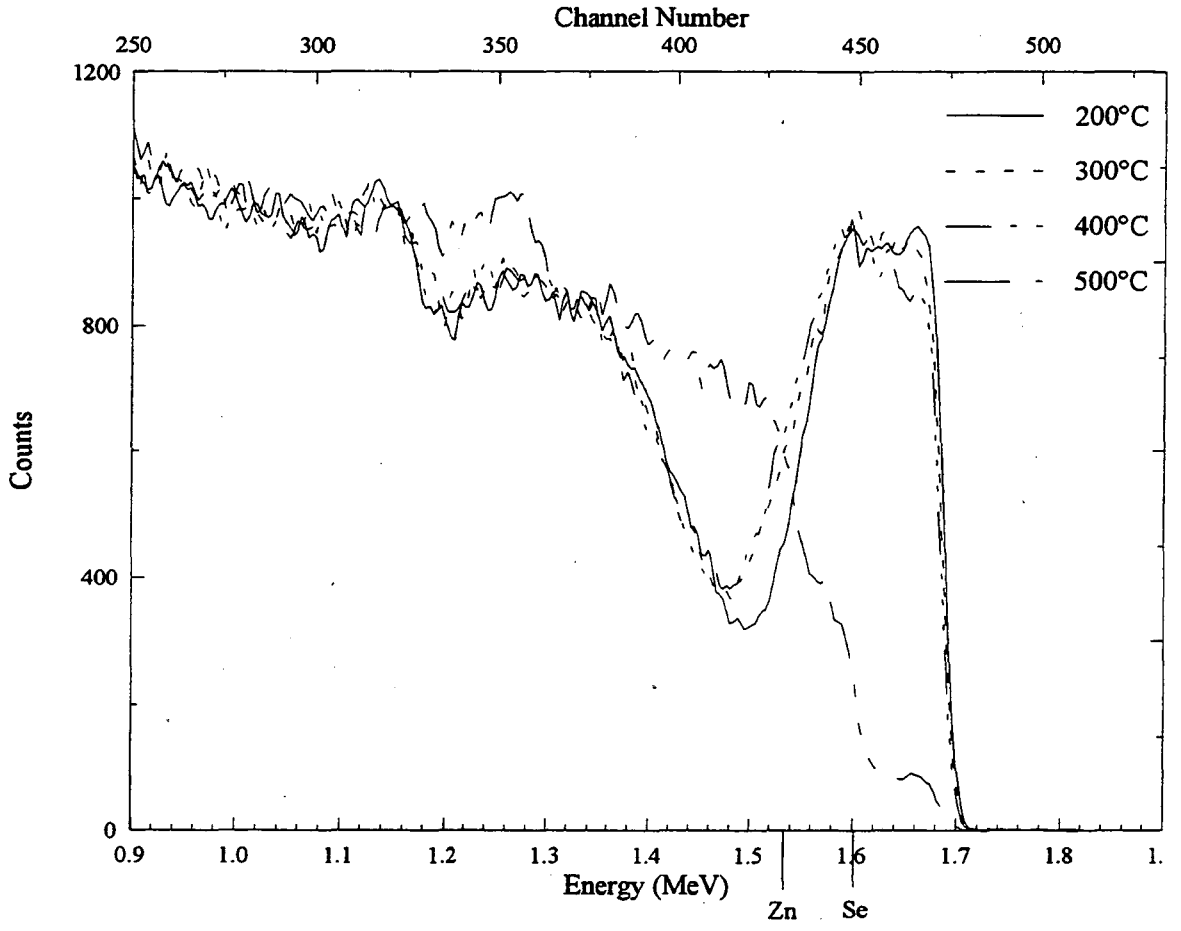

Figure 5.11: RBS spectra of Pd/ZnSe samples annealed for 30 minutes at temperatures between 200° and 500°C

the RBS spectrum changes dramatically. The Pd peak is almost gone and the ZnSe has migrated almost to the surface. This may indicate that the Pd has deeply diffused into the ZnSe. The x-ray spectrum also changes dramatically after the 500°C anneal. A multitude of new peaks appear as shown in figure 5.12. The two major peaks from the ternary phase are still visible, although their intensities are much reduced.

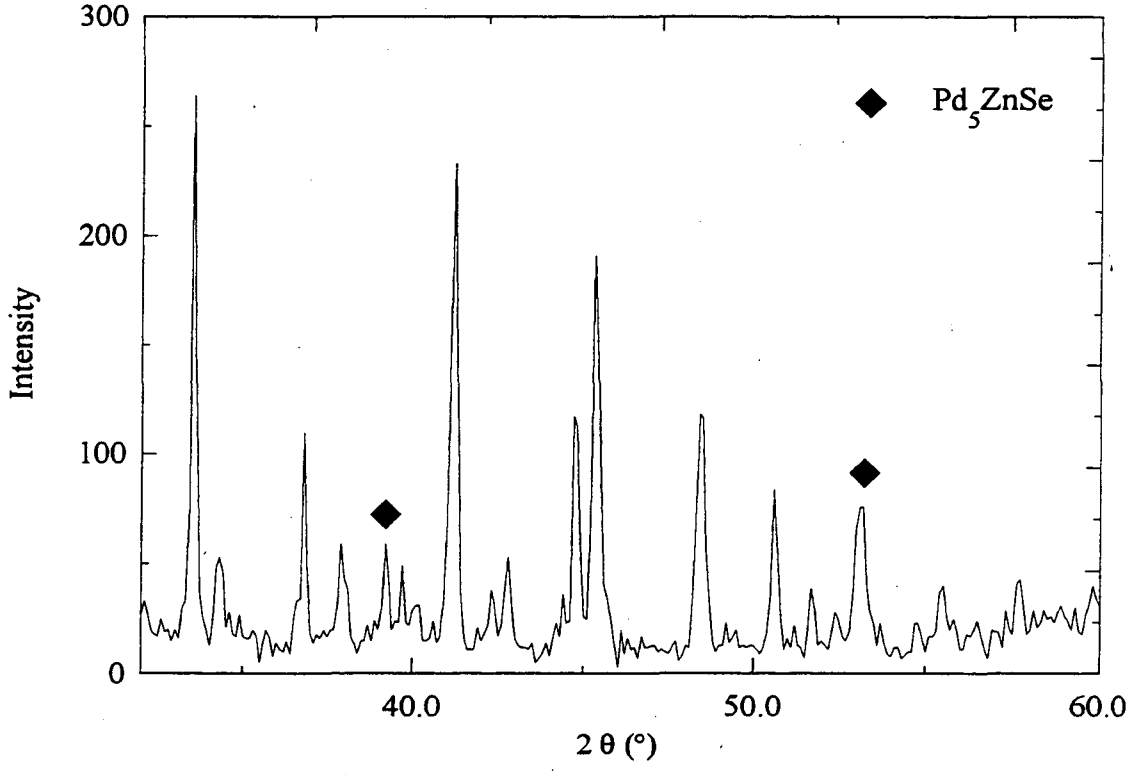

Figure 5.12: X-ray spectrum for Pd/ZnSe sample annealed at 500°C for 30 minutes.

The number of peaks which have appeared probably indicates that more than one phase has formed. The lack of steps in the RBS spectrum indicates that these phases are not formed in a layered structure. The phases to which these peaks belong have not been identified. If, however, this system behaves similarly to that of Pd on GaAs it is possible that several binary phases may have formed during annealing. Some, but not all, of the peaks can be assigned to $PdSe_2$, Pd_4Se, and $PdZn_2$. The stability of the ternary phase up to 500°C is similar to the stability of the Pd_2Si phase and the formation of binary phases at higher temperatures on GaAs (Hutchins and Shepela 1973; Yu, et al. 1986). There is, however, no evidence of a second ternary phase forming at temperatures just above the formation temperature for the first ternary, as in GaAs (Lin, et al. 1988; Sands, et al. 1987a).

Reactions of Pd on ZnSe are not very sensitive to surface conditions. Before deposition, cleaning consisted of the solvent clean and HF dip etch described in section 4.1.1. The small amount of O and C that remains, as indicated by the XPS results, does not seem to inhibit the reaction, indicating that the Pd has a strong driving force to react with the ZnSe. In comparison, native oxide also did not hinder the reaction in the Pd/GaAs system, although it did postpone the reaction in the Pd/Si case (Bower, et al. 1973; Lin, et al. 1988).

5.3 Pt

No significant reaction or interdiffusion is seen in the Pt/ZnSe system until it is annealed at temperatures of 550°C or above. The need for a higher temperature to initiate the reaction of Pt than Pd is a trend which is observed in the Si and GaAs systems as well. The series of RBS spectra of isochronally annealed samples in figure 5.13 shows that after a 30 minute anneal at 550°C interdiffusion has occurred. After the 30 minute anneal at 650°C there is a significant amount of Zn diffusion through the Pt film to the surface, and after the 750°C anneal the onset of the Pt signal has moved to lower energy. This observation indicates that the ions must be losing energy from travel through a layer on top of the Pt and therefore the surface is covered by Zn, Se, or a combination. The peaks in the spectra indicative of Zn at the surface (at an energy of 1.54 MeV) clearly show that Zn must be incorporated into this surface layer. In the Pt/GaAs system, outdiffusion of the Ga into the Pt is observed, just as Zn outdiffuses into the Pt, however accumulation of Ga at the surface is not observed (Fontaine, et al. 1983; Kumar 1975; Murarka 1974).

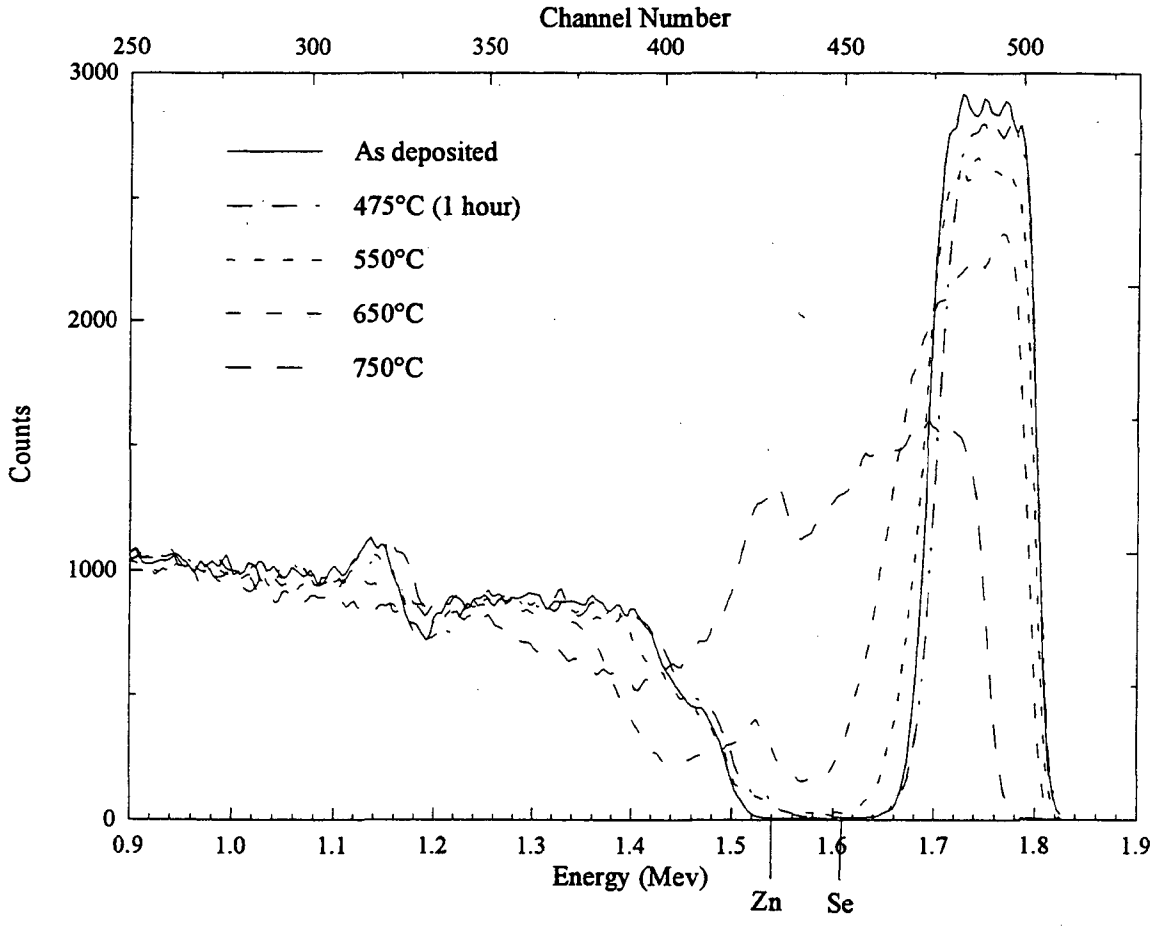

Figure 5.13: RBS spectra of Pt/ZnSe samples after 30 minute anneals, except where noted, at various temperatures

Since interdiffusion occurs in the temperature range of 550° to 600°C, a series of samples was annealed at 575°C. RBS spectra for samples isothermally annealed at 575°C for 10 and 30 minutes are presented in figure 5.14. These show a more gradual interdiffusion of Zn and Pt.

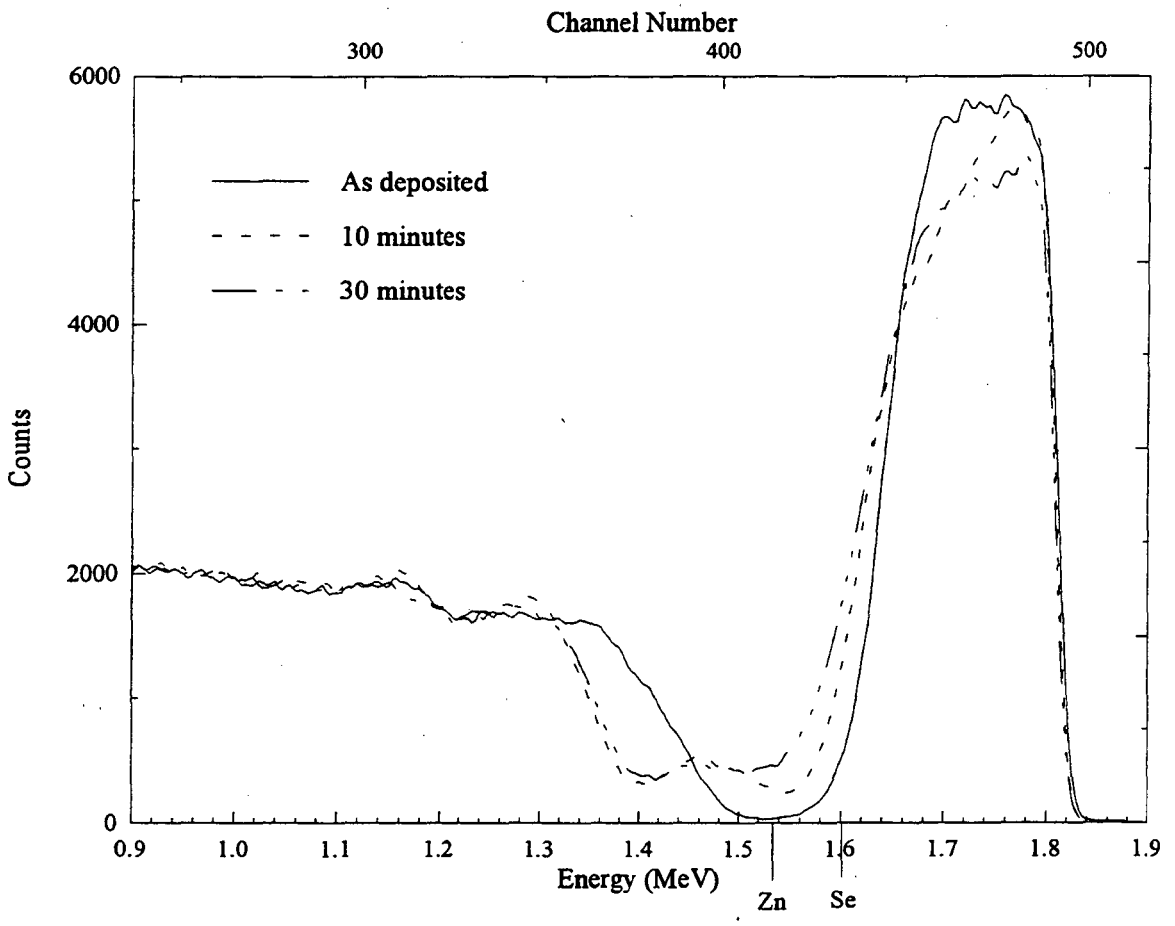

Figure 5.14: RBS spectra of isothermal anneals of Pt/ZnSe samples at 575°C for various times.

After 10 minutes Zn has diffused part of the way through the Pt layer, but has not reached the surface. This indicates that about half of the Pt layer has reacted. After 30 minutes the entire Pt layer has reacted, but there has not been any build up of Zn at the surface. Since Zn is seen to accumulate on the surface at high temperatures it is reasonable to assume that Zn is the main diffusing species during solid-state reaction. Although there is a significant amount of Zn in the Pt layer, no Zn-Pt compound can be identified in the x-ray results. Selected area diffraction in the TEM verifies that there is no phase formation between the Pt and Zn. This behavior differs from that of Pt and Ga, which form PtGa

compounds (Fontaine, et al. 1983). The amount of Zn in the layer can be estimated by matching the peak height simulated with RUMP to the experimental peak height. This simulation gives an estimate of the Pt to Zn ratio of 5:1.

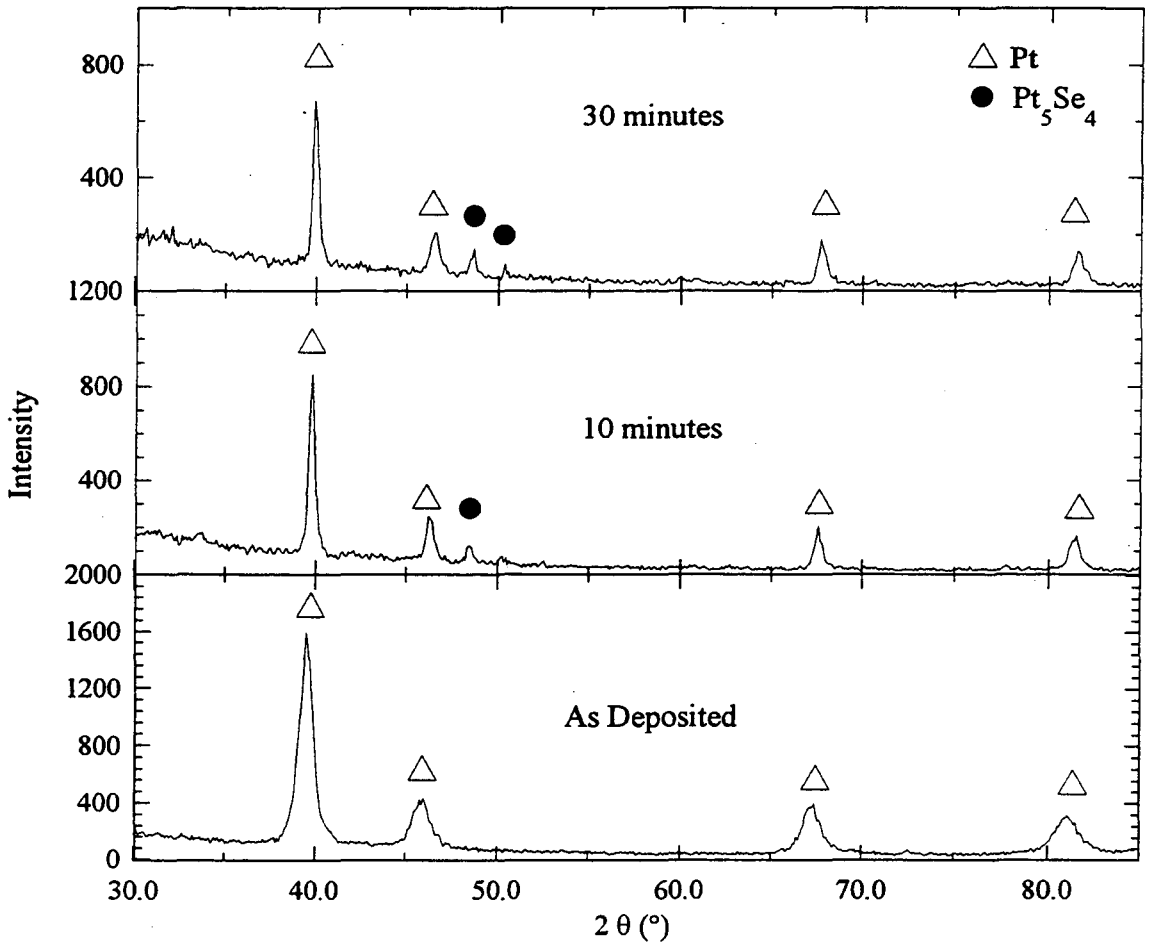

Figure 5.15: X-ray spectra of Pt/ZnSe samples annealed at 575°C for various times.

The x-ray spectra in figure 5.15 show that no new peaks for a Pt-Zn phase are present. Figure 5.15 shows the progression in the x-ray diffraction spectra for anneals at 575°C for times which correspond to those shown in the RBS spectra in figure 5.14. The Pt peaks (indicated by Δ) shift to slightly higher angles in the annealed samples. This shift denotes a

decrease in the lattice parameter of 0.017Å, which may be due to the incorporation of Zn into the Pt lattice. The peaks for Pt and the Pt_3Zn phase can be difficult to distinguish because they are in almost the same locations. They are separated by only 0.1° to 1.0°. Table 5.3 shows the peak positions and relative intensities of the phases compared to the measured peak positions. If the Pt_3Zn phase had formed, the relative intensities of the peaks should have changed, because in the Pt_3Zn phase all four of the peaks that coincide with Pt should have equal intensities. The relative intensities may also be affected by texture in the film.

Meas.	Pt			Pt_3Zn			Pt_5Se_4		
d(Å)	d(Å)	Rel. Int.	(hkl)	d(Å)	Rel. Int.	(hkl)	d(Å)	Rel. Int.	(hkl)
2.253	2.265	100	(111)	2.26	100	(111)			
1.953	1.962	53	(200)	1.948	100	(200)			
1.875							1.874	100	(302)
1.811							1.811	51	(123)
1.383	1.387	31	(220)	1.378	100	(220)			
1.180	1.183	12	(222)	1.171	100	(311)			

Table 5.3: Comparison of measured lattice spacings to tabulated lattice spacings and relative intensities from the powder diffraction file.

In addition the (300) peak should have appeared at $2\theta = 72.7°$. Since the peak intensities did not change, the (300) peak was not observed, and no phase was seen by selected area diffraction in the TEM, it is clear that a solid solution of Pt and Zn is formed rather than a

Pt-Zn phase. The Pt peaks also become narrower after annealing which implies grain growth in the film (see section 2.2). Most of the narrowing occurs in the first 10 minutes of annealing. The increase in grain size as estimated from equation 2.6 is approximately 145Å, although some of the narrowing may also be due to the relief of strain in the layer. After the 10 minute anneal, a new peak appears at $2\theta = 48.5°$ (indicated by a •) which grows stronger after 30 minutes. A second peak at $2\theta = 50.5°$ (indicated by a •) may be faintly visible in the sample annealed for 10 minutes and is definitely visible in the sample annealed for 30 minutes. These two peaks coincide with the (302) and (123) peaks for the Pt_5Se_4 phase, as shown in table 5.2. The formation of a binary anion-metal phase at the interface is also observed in the Pt/GaAs system with the formation of a $PtAs_2$ layer (Fontaine, et al. 1983). The identification of the Pt_5Se_4 phase has been verified by selected area diffraction as shown in figure 5.16c.

The presence of this binary phase is evident in the TEM micrograph presented in figure 5.16b shows that after a 30 minute anneal the Pt_5Se_4 has formed a continuous layer, although it is not of uniform thickness. The reaction of the ZnSe with the Pt seems to affect the ZnSe layer differently than the Pd reaction. It is observed that the ion milling, which is required to form the TEM samples, results in some holes in the ZnSe near the interface, which is the light area directly below the Pt_5Se_4 layer in figure 5.16b . This behavior is not normally seen after preparing ZnSe for TEM, and was not observed on the Pd/ZnSe samples. It is possible that the outdiffusion of Zn or the reaction between Pt and Se has weakened the ZnSe layer, or affected it in some other way.

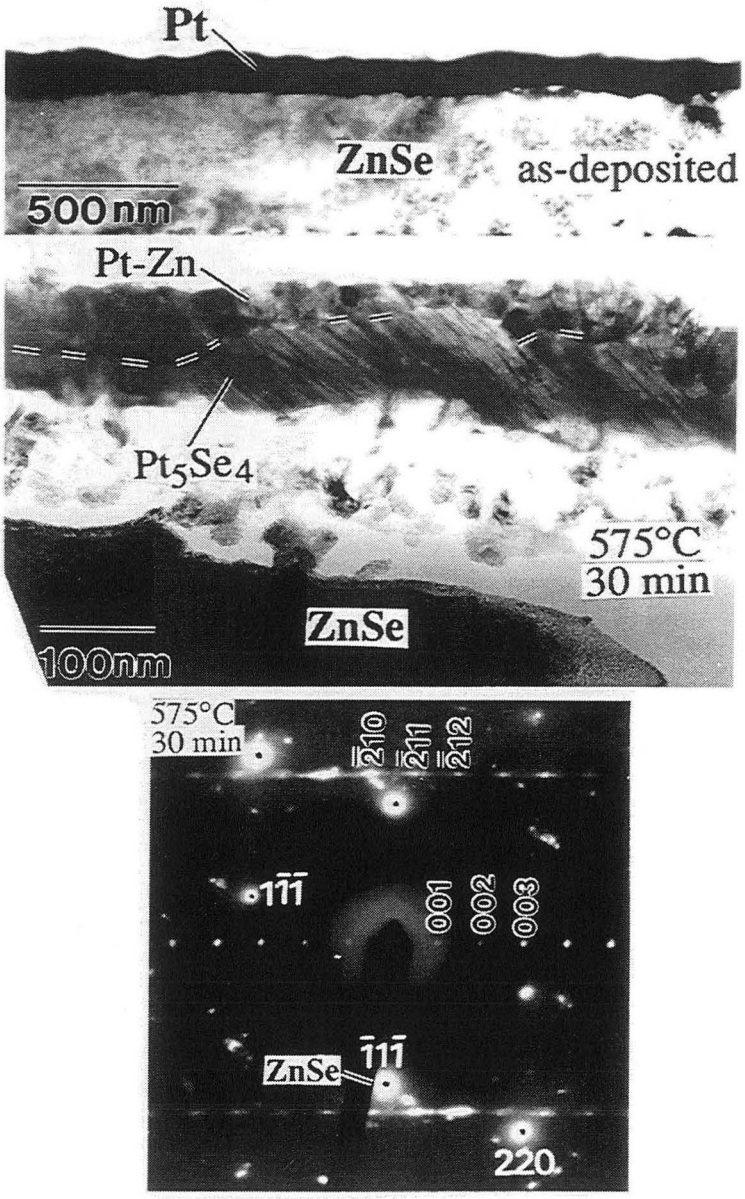

Figure 5.16: TEM micrographs showing progression of phase formation in Pt/ZnSe system during anneals at 575°C. (a) morphology of as-deposited Pt on ZnSe substrate, (b) Pt_5Se_4 layer formed after annealing at 575°C for 30 minutes, (c) selected area diffraction showing orientational relationship of Pt_5Se_4 with substrate. Pt_5Se_4 [$\bar{1}$ $\bar{2}$0]//ZnSe [110].

The binary phase remains evident after annealing the sample for one hour at 575°C. This annealing resulted in a decrease in the intensity of the Pt peaks, indicating that more of the Pt was consumed in the reaction. After annealing at 750°C for 30 minutes (RBS spectrum shown in figure 5.13) new diffraction peaks in the x-ray spectrum appear. The Pt_5Se_4 peaks are no longer evident and new peaks that align with those expected for $PtSe_2$ appear. Several other peaks also appear which have not been attributed to any Pt-Zn, Pt-Se, or ternary phase in the powder diffraction file database.

The Pt system is more affected by impurities than the Pd system. Consistent reactions could not be obtained without a comprehensive cleaning. To get consistent reactions the samples had to first have a 25 second etch in 49% HF, followed by a 6 minute Ar^+ backsputter to remove approximately 1000Å of ZnSe. Before depositing Pt, the Pt target was pre-sputtered for 2 minutes. This treatment should clean contaminants off the surface and reduce any contamination in the Pt film deposited from the target. It is not clear which of these two steps, or if both, are necessary to get consistent reactions. The Pt/Si system was shown to be affected by contaminants in the Pt film (Canali, et al. 1977; Crider and Poate 1980), while reaction in the Pt/GaAs system was hindered by the presence of a dense oxide at the interface (Kumar 1975).

6. Conclusions

Solid-state reactions of Pt and Pd on ZnSe are initiated by thermal annealing at 550° and 200°C, respectively. In the Pt system, Zn outdiffuses to form a solid solution of Pt and Zn while the remaining Se reacts to form a layer of Pt_5Se_4 at the interface. In the Pd system, a ternary compound, Pd_5ZnSe, is formed with an orientational relationship to the substrate. This ternary compound is stable during further annealing at 200°C and at temperatures up to approximately 500°C. The reactions of Pt and Pd on ZnSe are similar in many ways to their reactions on Si and GaAs.

The reactions of Pd are characterized by oriented films which often form in a granular structure. Pd_2Si forms with an epitaxial relationship to a <111> Si substrate while the ternary compound on GaAs forms in slightly misoriented grains. Pd_5ZnSe also forms in oriented grains which become more epitaxial as the reaction proceeds. Reactions of Pd metal on Si, GaAs and ZnSe, are not affected by impurities or surface cleanliness. Also, as on GaAs, Pd on ZnSe forms an oriented ternary compound. In the GaAs system, a new ternary phase forms when annealed at higher temperatures. This possibility has not been carefully investigated for the ZnSe system, but it appears that no new ternaries form up to 500°C when new binary phases form. As on Si and GaAs, the reaction of Pd with the substrate takes place at a lower temperature than the Pt reaction. The reactivity of the Pd/semiconductor interface is higher than that of the Pt/semiconductor interface.

The Pt/ZnSe system also behaves very much like the respective Si and GaAs systems. Pt forms binary compounds on ZnSe as it does on GaAs. The reaction is characterized by cation outdiffusion (Zn and Ga) and the formation of a binary anion-metal compound

(Pt_5Se_4 and $PtAs_2$) near the interface. Unlike the Pt/GaAs case, no binary cation-metal compound is observed in the Pt/ZnSe system. Pt is observed to have little orientational behavior in most cases and forms layered structures. Some texturing was observed in the GaAs system and also in the Si system, however this was dependent on the treatment of the samples. Textured layers may be observed in the GaAs system with the proper processing conditions. It was also found that impurities hindered the reaction at the Pt/ZnSe interface as in the Pt/Si system. In the Si system the reaction was altered due to impurities in the Pt film, in the ZnSe system it is not clear whether it is due to impurities in the film or at the interface.

These systems are not yet fully characterized. Further studies should determine what the final stable phases are in this system at a variety of temperatures. Also, the phase stability of the Pt_5Se_4 system should be determined. Preliminary studies of the behavior of Pd at higher temperatures indicates that other phases are formed. The barrier height and changes in electrical behavior must be investigated in order to evaluate the possible use of these systems for contacts. This information will also help verify or contradict some of the theories of Schottky barrier height. Finally, there are a wide variety of other metals whose thin film behavior should be interesting. The photoemission studies that have been done have pointed to several metals which have a variety of behaviors with low coverages. Investigating their behavior with thicker coverages and their thermal stability should prove interesting.

The information determined from these studies should be vital to the development of better quality and more highly reliable ZnSe devices. The desire for blue/green light

emitting devices and higher storage capacity optical disk drive systems continues to encourage further investigation of the ZnSe system. The knowledge derived from these studies should also be applicable to other II-VI systems and should aid in the advancement of devices for various applications. Moreover, theories of Schottky barrier height, ternary phase equilibria, and thin film interdiffusion and reaction should be improved based on the influx of data from a new system. Comparisons between ZnSe, with more ionic bonding, and the behavior of more covalently bonded semiconductors may lead to new perceptions about semiconductor properties and a better ability to predict electrical behavior and interfacial thermal stability.

7. References

K. Akimoto, T. Miyajima and Y. Mori, Journal of Crystal Growth **115**, 683 (1991).

A.A.I. Al-Bassam, The Arabian Journal for Science and Engineering **15**, 367 (1990).

S.G. Anderson, F. Xu, M. Vox, J.H. Weaver and H. Cheng, Phys. Rev. B **39**, 5079 (1989).

A. Aydinli and R.J. Mattauch, Solid State Electronics **25**, 551 (1982).

R.N. Bhargava, Journal of Crystal Growth **117**, 894 (1992).

J.B. Bindell, J.W. Colby, D.R. Wonsidler, J.M. Poate, D.K. Conley and T.C. Tisone, Thin Solid Films **37**, 441 (1976).

R.W. Bower, D. Sigurd and R.E. Scott, Solid-State Electron. **16**, 1461 (1973).

L.J. Brillson, Surface Sciences Reports **2**, 123 (1982).

L.J. Brillson, Surface Science **299/300**, 909 (1994).

W.D. Buckley and S.C. Moss, Solid-State Electron. **15**, 1331 (1972).

C. Canali, C. Catellani and M. Prudenziati, Appl. Phys. Lett. **31**, 43 (1977).

C. Canali, F. Catellani, G. Ottaviani and M. Prudenziati, Appl. Phys. Lett. **33**, 187 (1978).

W.K. Chu and G. Langouche, MRS Bulletin **January**, 32 (1993).

W.K. Chu, J.W. Mayer, M.-A. Nicolet, T.M. Buck, G. Amsel and F. Eisen, Thin Solid Films **17**, 1 (1973).

W.K. Chu, J.W. Mayer and M.A. Nicolet. *Backscattering Spectrometry* (Academic Press, N.Y., 1978).

C. Chung, F. Jain and G. Drake, Journal of Crystal Growth **117**, 1062 (1992).

M. Clement, J.M. Sanz, A. Climent and J.M. Martinez-Duart, Surface and Interface Analysis **12**, 334 (1988).

D.J.J. Coleman, W.R. Wisseman and D.W. Shaw, Appl. Phys. Lett. **24**, 354 (1974).

C.N. Comrie and J.M. Egan, J. Appl. Phys. **64**, 1173 (1988).

A. Continenza, S. Massidda and A.J. Freeman, Phys. Rev. B **42**, 2904 (1990).

C.A. Crider and J.M. Poate, Appl. Phys. Lett. **36**, 417 (1980).

B.D. Cullity. *Elements of X-ray Diffraction* 1978).

J.P. Delrue, M. Wittmer, T.S. Kuan and R. Ludeke, in *Materials Research Society Symposia Proceedings*, edited 1985), p. 455.

J.M. DePuydt, M.A. Haase, H. Cheng and J.E. Potts, Appl. Phys. Lett. **55**, 1103 (1989).

L.R. Doolittle, Nucl. Instrum. Methods **B9**, 334 (1985).

D.L. Dreilus, B.P. Sneed, J. Ren, J.W. Cook Jr., J.F. Schetzina and R.M. Kolbas, Appl. Phys. Lett. **57**, 1663 (1990).

Y. Fan, J. Han, L. He, J. Saraie, R.L. Gunshor, M.M. Hagerott and A.V. Nurmikko, Appl. Phys. Lett. **63**, 1812 (1993).

D.J. Fertig and G.Y. Robinson, Solid-State Electron. **19**, 407 (1976).

C. Fontaine, T. Okumura and K.N. Tu, J. Appl. Phys. **53**, 1404 (1983).

U. Gösele and K.N. Tu, J. Appl. Phys. **53**, 3252 (1982).

R.L. Gunshor, N. Otsuka and A.V. Nurmikko, IEEE Spectrum **May**, 28 (1993).

M.A. Haase, J. Qiu, J.M. DePuydt and H. Cheng, Appl. Phys. Lett. **59**, 1272 (1991).

J. Han, L. He, R.L. Gunshor and A.V. Nurmikko, IEEE Circuits and Devices 18 (1994).

M. Heuken, J. Sollner, F.E.G. Guimaraes, K. Marquardt and K. Heime, Appl. Phys. Lett. **60**, 1694 (1992).

F. Hiei, M. Ikeda, M. Ozawa, T. Miyajima, A. Ishibashi and K. Akimoto, Electronics Letters **29**, 878 (1993).

A. Hiraki, M.-A. Nicolet and J.W. Mayer, Appl. Phys. Lett. **18**, 178 (1971).

P.S. Ho, T.Y. Tan, J.E. Lewis and G.W. Rubloff, Journal of Vacuum Science and Technology **16**, 1120 (1979).

E. Hokelek and G.Y. Robinson, Solid State Electronics **24**, 99 (1981).

G.A. Hutchins and A. Shepela, Thin Solid Films **18**, 343 (1973).

R.G. Kaufman and P. Dowbor, J. Appl. Phys. **45**, 4487 (1974).

C.J. Kircher, Solid-State Electron. **14**, 507 (1971).

H.P. Klug and L.E. Alexander, edited (John Wiley & Sons, 1974), p.

T.S. Kuan, J.L. Freeouf, P.E. Batson and E.L. Wilkie, J. Appl. Phys. **58**, 1519 (1985).

V. Kumar, Journal of Physical Chemistry of Solids **36**, 535 (1975).

Y. Lansari, J. Ren, B. Sneed, K.A. Bowers, J.W. Cook Jr. and J.F. Schetzina, Appl. Phys. Lett. **61**, 2554 (1992).

S.S. Lau, W.K. Chu, J.W. Mayer and K.N. Tu, Thin Solid Films **23**, 205 (1974).

F. LaVia, P. Lanza, O. Viscuso, G. Ferla and E. Rimini, Thin Solid Films **161**, 13 (1988).

J.-C. Lin, K.-C. Hsieh, K.J. Schulz and Y.A. Chang, J. Mater. Res. **3**, 148 (1988).

T.W. Little and H. Chen, J. Appl. Phys. **63**, 1182 (1988).

A.W. Livingstone, K. Turvey and J.W. Allen, Solid-State Electron. **16**, 351 (1973).

T. Marshall, S. Colak and D. Cammack, J. Appl. Phys. **66**, 1753 (1989).

J.W. Mayer and K.N. Tu, Journal of Vacuum Science and Technology **11**, 86 (1974).

C.E. McCants, T. Kendelewicz, K.A. Bertness, P.H. Mahowald, M.D. Williams, R.S. List, I. Lindau and W.E. Spicer, Journal of Vacuum Science and Technology B **5**, 1068 (1987).

C.A. Mead, Physics Letters **18**, 218 (1965).

T. Miyajima, H. Okuyama and K. Akimoto, Japanese Journal of Applied Physics, Pt. 2 **31**, L1743 (1992).

S.P. Murarka, Solid-State Electron. **17**, 869 (1974).

H. Muta and D. Shinoda, J. Appl. Phys. **43**, 2913 (1972).

R.J. Nemanich, C.M. Doland and F.A. Ponce, Journal of Vacuum Science and Technology B **5**, 1039 (1987).

G.F. Neumark, R.M. Park and J.M. DePuydt, Physics Today **June**, 26 (1994).

P. Oelhafen, J.L. Freeouf, T.S. Kuan, T.N. Jackson and P.E. Batson, Journal of Vacuum Science and Technology B **1**, 588 (1983).

I. Ohdomari and K.N. Tu, J. Appl. Phys. **51**, 3735 (1980).

T. Okumura and K.N. Tu, J. Appl. Phys. **54**, 922 (1983).

T. Okumura and K.N. Tu, J. Appl. Phys. **61**, 2955 (1987).

J.O. Olowolafe, P.S. Ho, H.J. Hovel, J.E. Lewis and J.M. Woodall, J. Appl. Phys. **50**, 955 (1979).

G. Ottaviani, Journal of Vacuum Science and Technology **16**, 1112 (1979).

A. Oustry, M. Caumont, A. Escaut, A. Martinez and B. Toprasertpong, Thin Solid Films **79**, 251 (1981).

J.M. Poate and T.C. Tisone, Appl. Phys. Lett. **24**, 391 (1974).

J.M. Poate, K.N. Tu and J.W. Mayer. *Thin Films- Interdiffusion and Reactions* (The Electrochemical Society, Princeton, New Jersey, 1978).

R. Pretorius, Journal of the Electrochemical Society **128**, 107 (1981).

M.J. Rand and J.F. Roberts, Appl. Phys. Lett. **24**, 49 (1974).

T. Sands and V.G. Keramidas, in *Handbook on Semiconductors*, edited by T.S. Moss and S. Mahajan (Elsevier Science Publishers, 1994), p. 1997.

T. Sands, V.G. Keramidas, R. Gronsky and J. Washburn, Materials Letters **3**, 409 (1985).

T. Sands, V.G. Keramidas, A.J. Yu, K.-M. Yu, R. Gronsky and J. Washburn, J. Mater. Res. **2**, 262 (1987a).

T. Sands, V.G. Keramidas, K.M. Yu, J. Washburn and K. Krishnan, J. Appl. Phys. **62**, 2070 (1987b).

W. Schottky, Naturwissenschaften **26**, 843 (1938).

D. Sigurd, R.W. Bower, W.F. VanDerWeg and J.W. Mayer, Thin Solid Films **19**, 319 (1974).

A.K. Sinha, R.B. Marcus, T.T. Sheng and S.E. Haszko, J. Appl. Phys. **43**, 3637 (1972).

A.K. Sinha and J.M. Poate, Appl. Phys. Lett. **23**, 666 (1973).

L. Solymar and D. Walsh. *Lectures on the Electrical Properties of Materials* 465 (Oxford Science Publications, 1988).

I. Suemune, Appl. Phys. Lett. **63**, 2612 (1993).

S.M. Sze. *Physics of Semiconductor Devices* 868 (John Wiley & Sons, Inc., 1981).

T.D. Thompson and J.W. Allen, Journal of Crystal Growth **101**, 981 (1990).

N. Toyama, T. Takahashi, H. Murakami and H. Koriyama, Appl. Phys. Lett. **46**, 557 (1985).

M. Vos, C.M. Aldao, D.J.W. Aastuen and J.H. Weaver, Phys. Rev. B **41**, 991 (1990).

M. Vos, F. Xu, S.G. Anderson, J.H. Weaver and H. Cheng, Phys. Rev. B **39**, 10744 (1989).

A.P. Vyatkin, N.K. Maksimova, N.M. Panova, E.N. Pekarskii, I.D. Romanova and M.P. Yakubenya, Izvestiya Vysshikh Uchebnykh Zavedenii **4**, 3 (1981).

Y.X. Wang and P.H. Holloway, Vacuum **43**, 1149 (1992).

B.E. Warren. *X-ray Diffraction* (Addison-Wesley Publishing Company, Reading, Mass., 1969).

M. Wittmer, J. Appl. Phys. **54**, 5081 (1983).

W. Xie, D.C. Grillo, M. Kobayashi, L. He, R.L. Gunshor, H. Jeon, J. Ding, A.V. Nurmikko, G.C. Hua and N. Otsuka, Journal of Crystal Growth **127**, 287 (1993).

K.M. Yu, J.M. Jaklevic and E.E. Haller, in *Materials Research Society Symposia Proceedings*, edited 1986), p. 281.

K.M. Yu, W. Walukiewicz, J.M. Jaklevic and E.E. Haller, Appl. Phys. Lett. **51**, 189 (1987).

Z. Yu, J. Ren, J.W.J. Cook and J.F. Schetzina, Physica B **191**, 119 (1993).

Appendix I: ZnSe Etchants

Adapted from Landolt and Börnstein, *Numerical Data and Functional Relationships in Science and Technology: New Series.*

Etch	Etching Conditions	Remarks
concentrated NaOH solution	hot	polish [1]
dilute solution of Br in methanol	room temperature	different behavior of A and B surfaces [2]
HCl	hot	etch pits on A and B surfaces [2]
3 parts of H_2SO_4, 3 parts concentrated $K_2Cr_2O_3$, aqueous solution		applied to (110) faces [3]

[1] Aven, M., et al., Journal of Applied Physics, 32 (1961) 2261.

[2] Sagan, A., et al., Journal of Applied Physics, 39 (1968) 5336.

[3] Park, Y.S., Applied Physics Letters, 21 (1972) 567.

Appendix II: ZnSe OMVPE Growth Parameters

Parameter	145	167	181	201
DEZ temperature (°C)	15.00	15.00	15.00	15.00
DEZ vapor pressure (torr)	9	9	9	9
DEZ flow (sccm)	25	25	25	25
DISE temperature (°C)	10.00	32.50	32.50	32.50
DISE vapor pressure (torr)	10	22	22	22
DISE flow (sccm)	95	40	40	40
Injection pressure (torr)	500	500	300	500
Injection push flow (sccm)	500	1000	500	1000
Hydrogen shroud flow (sccm)	5200	5500	6500	5500
Chamber pressure (torr)	300	300	200	300
Growth temperature (°C)	464	464	464	464
Growth period (minutes)	41	60	45	60
CALCULATED VALUES:				
DEZ molar flow (micro-moles/min.)	20.58	20.58	34.72	20.58
DISE molar flow (micro-moles/min.)	82.58	82.22	141.37	82.22
Ratio Se/Zn	4.01	4.00	4.07	4.00
DEZn partial pressure (millitorr)	22	18	21	18
DISE partial pressure (millitorr)	87	73	84	73
Measured film thickness (microns)	0.47	0.5	0.9	0.5

Appendix III: Powder Diffraction Data File Record Numbers for Pd/Zn/Se and Pt/Zn/Se phases

Pd	5-0681*
PdZn:	
Pd_5Zn_{21}	4-0883D
PdZn	6-0620
PdZn	6-0630Q
$PdZn_2$	31-0942C
$PdZn_2$	34-1215I
PdSe:	
$PdSe_2$	11-0453
Pd_4Se	11-0498
$Pd_{2.5}Se$	11-0499Q
$Pd_{17}Se_{15}$	11-0508
PdSe	18-0953
$Pd_{17}Se_{15}$	29-1437C
Pd_7Se_4	31-0939C
PdGaZn:	
$Pd_7Zn_3Ga_4$	26-0675
ternaries:	None

Pt	4-0802
PtZn:	
Pt_3Zn	6-0584
PtZn	6-0604
$PtZn_{1.7}$	6-0619
Pt_5Zn_{21}	12-0612Q
Pt_7Zn_{12}	23-0466
$PtZn_5$	23-1311I
PtSe:	
$PtSe_2$	18-0970I
Pt_5Se_4	18-0971D
Pt_5Se_4	31-0950C
ternaries:	None

Appendix IV: Crystal Structure of Pd_5ZnSe

Structure information is taken from *Atlas of Crystal Structure Types*, J.L.C. Daams, P. Villars, and J.H.N. van Vucht, eds.

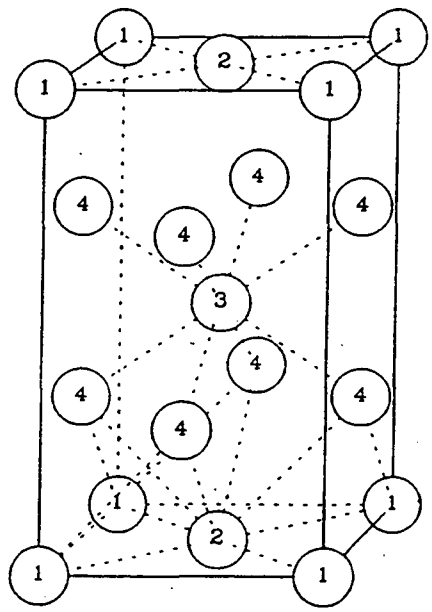

Pearson symbol: tP7

Structure type: $AsPd_5Tl$

Space group: P4/mmm

Space group number: 123

a=0.4005 nm c=0.7042 nm

Number	Atom	Multiplicity	Wyckoff letter	x	y	z	Occupancy
1	Tl	1	a	0	0	0	1
2	Pd1	1	c	½	½	0	1
3	As	1	d	½	½	½	1
4	Pd2	4	i	0	½	0.30	1

LAWRENCE BERKELEY LABORATORY
CENTER FOR ADVANCED MATERIALS
1 CYCLOTRON ROAD
BERKELEY, CALIFORNIA 94720